Inaugural Dissertation

for
obtaining the doctoral degree
of the
Combined Faculty of Mathematics, Engineering and Natural Sciences
of the
Ruprecht - Karls - University
Heidelberg

Presented by
M.Sc. Daniel Beyer

born in: Kassel, Germany
Oral examination: 18.06.2025

# Molecular Dominoes:

## The interplay between FGF2 oligomerization and PI(4,5)P2 clustering in membrane pore formation

Referees

Prof. Dr. Walter Nickel

Dr. Petr Chlanda

# Table of Contents

## Abstract

Within the fibroblast growth factor family, fibroblast growth factor 2 (FGF2), a potent mitogen, follows an unconventional secretory pathway (UPS), as FGF2 does not contain a signal peptide that directs the protein for classical ER/Golgi export. It is able to translocate directly across the plasma membrane (type I UPS). This mechanism involves sequential interactions with cellular components at the plasma membrane. The cytosolic α1 domain of the Na,K-ATPase recruits FGF2 to the membrane. FGF2 then interacts with Tec kinase, phosphorylating FGF2. FGF2 binds to the phosphoinositide PI(4,5)$P_2$ lipids in the inner leaflet of the plasma membrane, leading to oligomerization and membrane insertion. The translocation is then completed by membrane-proximal heparan sulfate chains of heparan sulfate proteoglycans, which outcompete PI(4,5)$P_2$ in the mutually exclusive binding site, making the translocation unidirectional and irreversible. Bound to the cell surface, FGF2 can exert its function in autocrine and paracrine signaling. Direct visualization of single secretion events from living cells by total internal reflection microscopy (TIRF) revealed an average time interval of 200 ms from FGF2 recruitment at the inner plasma membrane leaflet to full translocation to cell surfaces. Reconstitution of FGF2 translocation in giant unilamellar vesicles identified FGF2, a PI(4,5)$P_2$-containing membrane, and luminal long-chain heparin as the minimal component system for translocation. The average FGF2 oligomer size for pore formation was determined by fluorescence brightness analysis to be four to eight monomers, both *in vitro* and in cells.

Using Molecular Dynamics simulations, I demonstrated that the C95-C95 disulfide-bridged FGF2 dimer self-assembles into oligomers on flat, PI(4,5)$P_2$-containing membranes to induce a substantial, spatially-confined membrane remodeling event. The FGF2 oligomer gathered 4 to 5 of the negatively charged PI(4,5)$P_2$ molecules per FGF2 monomer, thereby creating a strong, local electrical charge gradient across the membrane. In addition, PI(4,5)$P_2$ accumulation caused negative curvature deformations underneath the FGF2 oligomer. Combined with a very high concentration of non-bilayer lipids such as PI(4,5)$P_2$ and phosphatidylethanolamine, these effects generate spatially confined stress on the membrane, which I propose to be the primary driving force for membrane pore formation, the process that mediates unconventional secretion of FGF2 into the extracellular space.

## Zusammenfassung

Innerhalb der Familie der Fibroblasten-Wachstumsfaktoren folgt der Fibroblasten-Wachstumsfaktor 2 (FGF2), ein starkes Mitogen, einem unkonventionellen Sekretionsweg, da FGF2 kein Signalpeptid enthält, das das Protein zum klassischen ER/Golgi-Export leitet. Direkte Translokation durch die Plasmamembran führt zur Sezernierung von FGF2, womit es dem Typ I Mechanismus unkonventioneller Proteinsekretionswege folgt. Dieser Mechanismus beinhaltet sequenzielle Interaktionen mit zellulären Komponenten an der Plasmamembran. Die zytosolische α1-Domäne der Na,K-ATPase rekrutiert FGF2 an die Membran. FGF2 interagiert dann mit der Tec Kinase, die FGF2 phosphoryliert. FGF2 bindet dann an das Phosphoinositid $PI(4,5)P_2$ an der zytoplasmatischen Lipidmonoschicht der Plasmamembran. Dadurch kommt es zur Oligomerisierung, transienter Porenbildung und Membraneinlagerung des FGF2 Oligomers. Die Translokation wird dann durch membrannahe Heparansulfatketten von Heparansulfat-Proteoglykanen vervollständigt, die $PI(4,5)P_2$ an der sich gegenseitig ausschließenden Bindungsstelle verdrängen, wodurch die Translokation unidirektional und irreversibel wird. An die Zelloberfläche gebunden, kann FGF2 seine Funktion bei der autokrinen und parakrinen Signalübertragung ausüben. Die direkte Visualisierung einzelner Sekretionsereignisse in lebenden Zellen mittels *total internal reflection fluorescence* Mikroskopie (TIRF) ergab eine durchschnittliche Zeit von 200 ms von der FGF2-Rekrutierung an der zytoplasmatischen Lipidmonoschicht der Plasmamembran bis zur vollständigen Translokation an die Zelloberfläche. Die Rekonstitution der FGF2-Translokation in *giant unilamellar vesicles* (GUVs) identifizierte die minimal nötigen Komponenten für die Translokation, FGF2 Oligomerisierung, eine $PI(4,5)P_2$ enthaltende Membran und langkettiges Heparin im Lumen der Vesikel. Die durchschnittliche Größe des FGF2 Oligomers wurde mittels Fluoreszenz-Helligkeitsanalysen auf vier bis acht Monomere bestimmt.

Mit Hilfe von Molekulardynamik-Simulationen konnte ich zeigen, dass sich das über eine Disulfidbrücke zwischen (C95-C95) kovalent verknüpfte FGF2-Dimere auf flachen, $PI(4,5)P_2$-enthaltenen Membranen zu einem ringförmigen Hexamer assemblieren. Dadurch wird die Membran lokal deformiert und die Lipidverteilung beeinflusst. Das FGF2-Hexamer reichert lokal 4 bis 5 der negativ geladenen $PI(4,5)P_2$ Moleküle pro FGF2-Monomer an und verursacht hierdurch eine negative Membrankrümmung unter dem FGF2-Oligomer. In Verbindung mit einer sehr hohen Konzentration von nicht-bilamellaren ($PI(4,5)P_2$, Phosphatidylethanolamin, und Cholesterin) führen diese Effekte zu einem räumlich begrenzten Stress für die Lipiddoppelschicht, der die Hauptantriebskraft für die Membranporenbildung ist.

# 1 Introduction

Cells are built from a plethora of different proteins, lipids, DNA, RNA, and other components to ensure proper functioning. In eukaryotic cells, many processes are compartmentalized into highly specialized, membrane-encapsulated organelles. To maintain homeostasis and intercellular communication, cells must not only synthesize necessary proteins but also accurately target them to their designated subcellular localization or secrete them across the plasma membrane into the extracellular space. An intricate protein transport machinery has evolved to mediate and regulate the transport of (newly synthesized) proteins to their proper location. For this, typically, hydrophobic N-terminal signal peptides are recognized by the transport machinery to sort the proteins through the endoplasmic reticulum (ER)/Golgi-mediated secretory pathway (1).

However, over the past few decades, proteins lacking such signal peptides have been identified, revealing the existence of ER/Golgi-independent secretory pathways. These alternate routes, collectively termed unconventional secretory pathways (2), vary depending on the cell type, tissue context, type of cargo, and even the energetic state of the cells. Since most of the unconventionally secreted proteins are involved in vital physiological functions, it is therefore essential to characterize these mechanisms at the molecular level.

## 1.1 The Classical Secretory Pathway

The classical protein secretion begins directly during the translation of newly synthesized proteins. These proteins are directed to the ER and subsequently transported through the Golgi network to their designated target regions.

This pathway is typically initiated by amino-terminal signal peptides at the nascent protein chain during the beginning of translation. These short 15 to 30 amino acid-long sequences, consisting of a stretch of hydrophobic residues flanked by positively charged residues, are recognized by the signal recognition particle (SRP) (3, 4). The binding of the SRP to the nascent chain and the ribosomes temporarily halts elongation. The ribosome – mRNA – peptide – SRP – complex is then recruited to the ER membrane where the SRP receptor is located (5). The final step in this delivery is the guanosine triphosphate-dependent (GTP) dissociation of the SRP complex (4). Now, elongation continues and the polypeptide chain is translocated co-translationally into the lumen of the ER or integrated into the membrane of the ER-mediated by the Sec61 translocon complex (1, 6-8). Inside the ER, the signal sequence is cleaved off by signal peptidases (9).

The ER provides a well-adapted environment for the maturation of newly synthesized proteins, containing numerous chaperones assisting in proper protein folding (10). In addition, the ER is home to proteins that attach post-translational modifications to the young proteins, which are crucial for their functionality and stability. These modifications include amongst others N-glycosylation at asparagine residues (11), the addition of glycophosphatidylinositol

(GPI) anchors for membrane attachment (12), the assembly of multimeric complexes (13), and the formation of disulfide bonds in the oxidative environment of the ER lumen (14). Despite this optimized environment, various factors can lead to improper protein folding. To tackle issues in protein folding, the ER also contains a quality control mechanism which, in the end, triggers the ER-Associated Degradation (ERAD) if the folding issues cannot be resolved. Misfolded proteins are exported from the ER into the cytosol, where they are marked by ubiquitination and subsequently degraded by the proteasome (15).

Non-ER resident proteins passing the quality control system exit the ER through coat protein complex II (COPII) vesicles at specific ER exit sites (ERES) (16). COPII vesicles are transported to the Golgi apparatus (17, 18). The Golgi is an organelle consisting of five to eight stacked and linked cisternae which are divided into three primary compartments named cis-, medial- and trans-Golgi. Each of these compartments has a distinct and unique functionality (19, 20).

COPII vesicles first arrive at the cis-Golgi closest to the ER. Upon arrival, the vesicles shed their COPII coat and fuse with the Golgi membrane to form the ER-Golgi intermediate compartment (ERGIC) (21). From the ERGIC, the cargo is then progressively transported through the cis-Golgi to the trans-Golgi. During this transport, proteins undergo further processing by enzymes embedded in Golgi membranes. These modifications can include remodeling of the already added glycosylations, the addition of small chemical groups like acetylation, phosphorylation or additional glycosylation, proteolytic cleavage, fatty acid addition to targeting the proteins to membranes, and more (22). These posttranslational modifications not only secure proper function but also act as sorting signals in the trans-Golgi network. From here, proteins are packaged into vesicles destined for specific cellular locations, e.g. exocytosis via secretory vesicles or organelles like endosomes or delivery to organelles such as lysosomes (22).

This direction of protein transport is referred to as anterograde transport. However, Golgi- and ER-resident proteins are also unintentionally transported along this pathway. To retain these proteins in their respective compartment, COPI-coated vesicles mediate retrograde transport from the trans-Golgi back to the ER (16).

## 1.2 Unconventional Secretory Pathways

As discussed so far, “conventional” protein secretion occurs via the ER/Golgi route, researchers have discovered that some proteins can be secreted independently of the ER/Golgi pathway. Early evidence of these “unconventionally” secreted proteins was the lack of N-terminal signal peptides and the ability to be secreted in the presence of Brefeldin A, Monensin, and Nocodazole, which all block intracellular vesicle transport and classical secretion (23-26).

Since the late 20$^{th}$ century, numerous cargo proteins for unconventional secretion (UPS) have been identified, with modern secretomics analysis predicting the existence of many more (27).

A major challenge in clearly identifying more UPS cargoes is the missing common export signals, intracellular functions of the secreted proteins, cell type specificity, and (stress) signal-dependent secretion (e.g. Interleukin 1-β, IL-1β).

UPS pathways can be distinguished into four types (type I-IV) based on their secretion mechanism (28). Type I to III refer to soluble proteins without signal peptide, known as leaderless secreted proteins (LLSPs). These proteins are translocated either directly across the plasma membrane (UPS type I), via membrane-resident ATP-binding cassette (ABC) transporters (UPS type II), or through endocytic compartments that fuse with the plasma membrane (UPS type III). UPS type IV cargo typically consists of membrane proteins bypassing the Golgi on their way to the plasma membrane. An overview of the UPS pathways can be found in Figure 1.

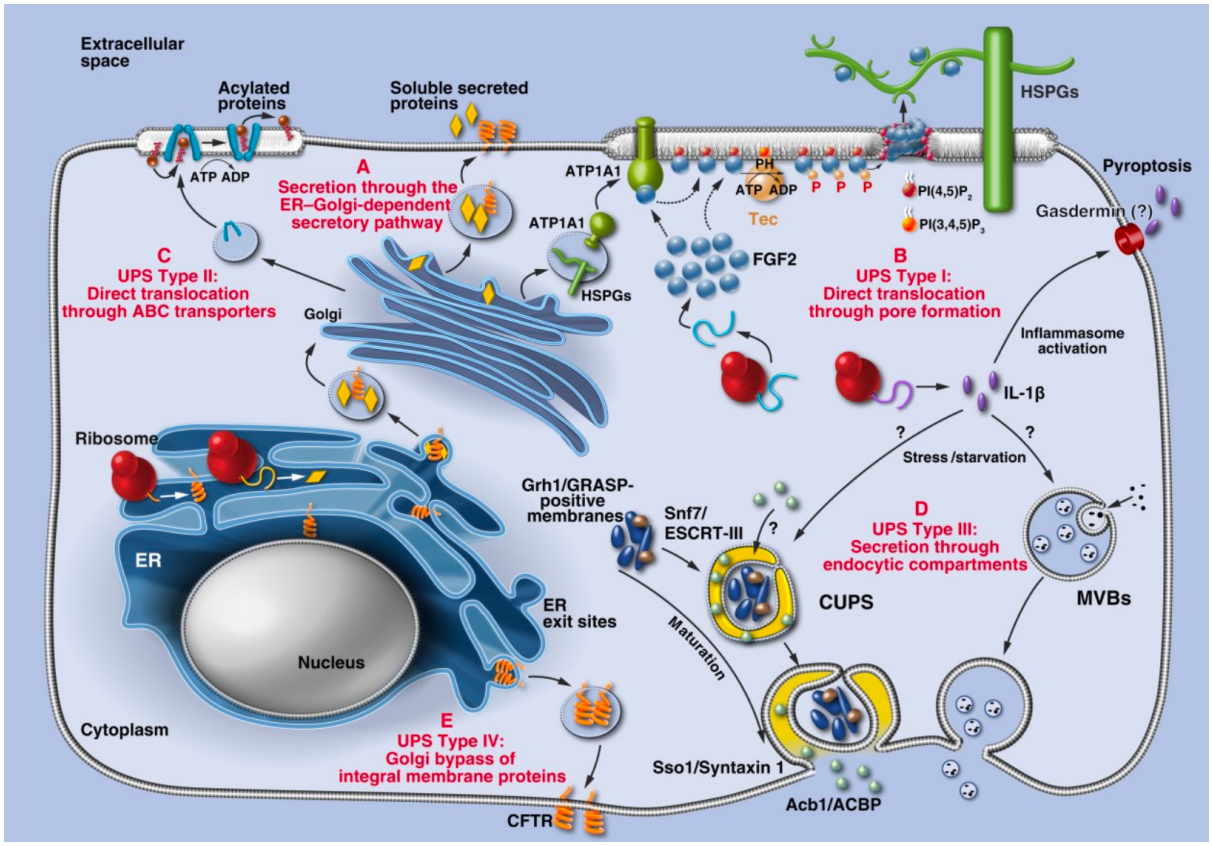


**Figure 1: Overview of unconventional secretory pathways.** Most secreted proteins follow the conventional pathway via ER and Golgi in a signal peptide-dependent manner. However, proteins can also be exported via unconventional protein secretion (UPS) which follows one of four types. UPS type I: Direct translocation across the plasma membrane my lipid-dependent membrane pore formation. UPS type II: Secretion of mostly acylated proteins via membrane-resident ABC transporters. UPS type III: Secretion through endocytic compartments, which fuse with the plasma membrane to release cargo. UPS type IV: Golgi-bypass of plasma membrane proteins directly from ER to the plasma membrane. Adapted from Dimou and Nickel (2018) (29).

UPS type I: direct translocation across the plasma membrane through pores

Some UPS type I cargo proteins are very well-characterized examples of unconventional secretion. FGF2 and human immunodeficiency virus (HIV) trans-activator of transcription (TAT) are signal peptide-less, constitutively secreted proteins. Both are recruited to the plasma membrane by phosphatidylinositol 4,5-bisphosphate ($PI(4,5)P_2$) lipids, which triggers homo-oligomerization of FGF2 and TAT and subsequent pore formation to cross the plasma membrane (30-32). These proteins contain a $PI(4,5)P_2$-binding motif and are associated with heparan sulfate proteoglycans (HSPG) on the cell surface (33, 34). However, it is not clear yet if HIV TAT's association with HSPGs is essential for its secretion. Further details on the unconventional secretion of FGF2 are discussed in chapter 1.3.3.

Another member of the FGF family, FGF1, also follows type I UPS. In contrast to FGF2, FGF1 is only secreted upon stress conditions like heat shock, starvation, and hypoxia (35). In addition, FGF1 secretion requires the assembly of a protein complex and cannot cross the plasma membrane without it. This complex includes S100A13, a calcium-binding protein, the p40 form of synaptotagmin-1, sphingosine kinase 1, and also requires copper ions as a cofactor (36-38). Similar to FGF2, though, FGF1 secretion also requires the formation of a disulfide bond, yet a different one (C30 in FGF1 compared to C95 in FGF2), binding to acidic lipids at the plasma membrane, and FGF1 has to be fully folded (39-41).

Tau is another example following type I UPS. In a physiological context, Tau is a microtubule-associated protein, and dynamic phosphorylation and dephosphorylation regulate its binding to microtubules, ensuring proper cellular microtubule-related functions (42). In pathological conditions like Alzheimer's disease, Tau gets hyperphosphorylated, causing reduced affinity towards microtubules and increased cytosolic concentrations (43). Hyperphosphorylated Tau is able to form large aggregates, leave cells, and accumulat in the nervous system, which has been identified as the cause of these progressive, neurodegenerative diseases called tauopathies (44, 45). The mechanism of Tau secretion and spreading has not been fully unraveled but has been linked with both vesicular and non-vesicular UPS (46). Just like FGF2, *in vitro* studies demonstrated that Tau is able to bind to $PI(4,5)P_2$ in large unilamellar vesicles (LUVs) and requires HSPGs to reach the cellular surface in living cells (47, 48). The latter was demonstrated by blocking sulfation of heparan sulfates by $NaClO_3$, which not only reduced surface levels but also inhibited cell-to-cell spreading of Tau. As with some other UPS cargo proteins, Tau can also be secreted by different UPS pathways. It has been reported that in some immune cells, astrocytes, and specialized neurons, Tau is exported via secretory lysosomes (46).

Type I UPS can also be triggered by inflammation. Interleukin-1β (Il-1β) is a well-studied leaderless cytokine and fulfills a central role in the innate immune system. Based on the specific cell type and stimulus, Il-1β can follow type I or type III UPS. In macrophages, Il-1β resides as inactive pro-Il-1β activated by caspase-1. Upon inflammatory response, Il-1β is then

released via hyperpermeabilization of the plasma membrane by gasdermin D, which involves inflammasome activation and is usually followed by the death of the secreting cell (49-51). More on the type III UPS of Il-1β will follow in the respective sub-chapter.

UPS type II: translocation by ABC transporters

ABC transporters are a diverse family of membrane-resident transporters that use ATP for active transport of cargo against a concentration gradient and are represented on all levels of life, from prokaryotes to eukaryotes (52, 53). Yet, only a handful of cargo has been described so far. An early discovery was the *Saccharomyces cerevisiae* mating pheromone a-factor (54). The small 1.5 kDa peptide is secreted to the cell surface of *S. cerevisiae* by the Ste6 transporter (55). Another interesting type II UPS cargo is the *Leishmania* hydrophilic acetylated surface protein B (HASPB). The secretion machinery of HASPB has not been fully unveiled so far. However, its secretion requires correct targeting of the protein through double acylation at the HASPB SH4 domain, which is myristoylated and palmitoylated and cannot be blocked by inhibitors of the ER/Golgi pathway (56-58). What is most intriguing is that recombinant HASPB is able to be secreted in human cells, indicating a highly conserved mechanism that can even be recognized by higher mammals (57).

UPS type III: translocation involving endocytic compartments

Type III UPS describes the export of cargo by involvement of intracellular vesicles like secretory lysosomes, secretory autophagosomes, or multi-vesicular endosomes (28). *S. cerevisiae* provides another well-characterized example of a UPS cargo protein, the acyl-coenzyme A (CoA) binding protein (Acb1 in yeast, ACBP in mammals). Secretion of Acb1 is linked to starvation and requires the presence of the Golgi reassembly and stacking protein (GRASP) yeast orthologue Grh1 (59). Under nutrient starvation conditions, Grh1 relocates from the ER-Golgi to the ERES to form the Compartment of Unconventional Protein Secretion, CUPS, a specialized vesicular organelle for the secretion of proteins. CUPS also contain proteins of the ESCRT machinery, namely Vps23, the ESCRT-III protein Snf7 for structural integrity, and require the t-SNARE protein Sso1 for fusion with the plasma membrane and release of cargo (59-61).

For Il-1β, we already discussed its secretion following type I UPS upon inflammatory signals. Yet, under nutrient starvation conditions, Il-1β has been found to be secreted from non-macrophages in a GRASP-dependent process also involving multi-vesicular body formation (MVBs) (62). It has been found that Il-1β secretion in a starvation context could be blocked with general inhibitors of autophagy and impairing the normal function of the main gene for autophagy, *Atg5*, by mutations (62, 63). The secretion of Il-1β demonstrates the complexity of finding and characterizing UPS cargo, as the exact mechanisms can greatly differ between cell types and external stimuli.

UPS type IV: translocation bypassing the Golgi

In contrast to type I and II UPS, type IV UPS cargo are integral membrane proteins containing uncleavable signal sequences. Therefore, they will follow a path through the ER and, under normal conditions, reach their target membrane in a conventional manner. Golgi-bypass secretion is mostly activated upon cellular stress conditions or impairment of the conventional secretion machinery (64).

A well-characterized example of type IV UPS is the cystic fibrosis transmembrane conductance regulator (CFTR), a cAMP-activated ion channel that transports chloride ions out of epithelial cells (65). CFTR is an integral membrane protein consisting of two transmembrane domains, each built from six transmembrane helices. The signal sequences for integration into the membrane are located in the transmembrane helices (66), and under normal conditions, CFTR follows conventional secretion, including heavy glycosylation in the Golgi (65, 67). However, if this pathway is blocked, e.g. upon ER stress, CFTR is able to reach the plasma membrane in an immature state by a GRASP-dependent Golgi bypass secretion (68). Surprisingly, this immature form of CFTR remains fully functional (69). In cystic fibrosis disease, the most common mutation in patients is the ΔF508 deletion, which prevents CFTR from reaching the plasma membrane due to misfolding and degradation from the ER. By rerouting CFTR-ΔF503 to type IV UPS, it could be possible to rescue the healthy phenotype. Indeed, it was discovered that phosphorylated version GRASP55 is able to send CFTR-ΔF503 to the plasma membrane in an unconventional and inositol-requiring enzyme type 1 (IRE-1) dependent manner (69).

## 1.3 Fibroblast Growth Factors:

### 1.3.1 The FGF family

The fibroblast growth factor superfamily was discovered with its first member in the 1970s, with 24 known proteins today, 22 of which can be found in humans (FGF1 to FGF14, FGF16 to FGF23). All FGFs are essential in controlling different aspects of the organism, from embryogenesis to stem cells, adult cells, and even cancer cells by autocrine, paracrine, or even endocrine signaling (70). They are diverse in molecular weight (MW), ranging from 17 to 34 kDa, but share a similar core structure of 12 antiparallel β-sheets.

The family can be divided into canonical FGFs, which activate FGF receptors (FGFRs) at the plasma membrane, and non-canonical FGFs (FGF11-FGF14), also known as FGF homology factors (FHFs) (71). The latter were thought to be non-signaling, intracellular proteins, yet with high affinity towards heparan sulfates. Very recently, though, it has been discovered that FGF11 to FGF14 are also able to reach the extracellular space upon stress conditions like elevated temperature and even activate FGFR downstream signaling by direct interaction with FGFR1 (72). Inhibitors of classical secretion are not able to block FGF11-FGF14 secretion, but ouabain, an inhibitor of the Na,K-ATPase, is able to block the secretion of the FHF family

proteins similar to FGF2 (73, 74). Very recently, the long isoform of FGF12 has been shown to follow Na,K-ATPase, Tec kinase, and lipid-dependent direct translocation from cells, which could not be blocked by inhibitors of classical protein secretion (75). The authors of this study hypothesize that the other secreted FGFs also follow the same mechanism, which will require further investigations.

Most canonical FGFs contain an N-terminal signal sequence for secretion through the classical secretory pathway and exhibit a high affinity towards HSPGs (76). However, several FGFs are secreted in a leaderless manner. The first group, comprising FGF9, FGF16 and FGF20 (FGF9 family), is secreted via the ER/Golgi pathway through a nonclassical, uncleavable export sequence in the N-terminal region (77-79). The second group, consisting of FGF1 and FGF2, is secreted by type I UPS. Another group of FGFs containing a leader signal, consisting of FGF19, FGF21, and FGF23, shows no or only low affinity towards heparan sulfates. Upon secretion, these FGFs act as endocrine hormones and require α- (FGF23) or β-klotho (FGF19/21) to interact with FGFRs (80, 81).

### 1.3.2 The FGF receptor family

As already touched, FGFs exert their cellular functions through FGFRs. FGFRs are tyrosine kinase receptors (RTKs) residing in the plasma membrane, sharing the same overall structural characteristics as most tyrosine kinases (82). They have a cytosolic tyrosine kinase domain, a single transmembrane helix, and an extracellular ligand binding domain consisting of three immunoglobulin-like (IG) domains, also classifying FGFRs as part of the immunoglobulin family (83). There are four FGFRs, with different isoforms produced by alternative splicing, contributing to the diversity of function in FGF signaling (84). Signaling is induced by ligand binding in the IG domains of FGFRs. In the N-terminal region of the IG-II domain is a highly conserved region of 18 residues across all isoforms to bind heparan sulfate chains, crucial for high-affinity binding of FGFs with FGFRs and formation of the signaling complex constituted of FGF, FGFR, and heparan sulfate (85-88). Upon ligand binding, FGFRs dimerize as most RTKs and undergo autophosphorylation of their cytosolic domains on up to 7 tyrosine residues (89). This activates downstream signaling cascades, the exact type depending on the type of FGF and FGFR interaction. The Ras – mitogen-activated protein kinases (MAPK) pathway, the phosphatidylinositol-3-kinase (PI3K) – Akt pathway, the phospholipase-$\gamma$ (PLC$\gamma$) pathway, and the signal transducer and activator of transcription (STAT) pathway are amongst the FGFR activated pathways, controlling a diverse range of important cellular functions, including proliferation, differentiation, survival and stress response (90, 91). With these many and essential physiological processes under FGFR control, it is no wonder that impairments in FGF signaling can cause a wide range of diseases such as skeletal dysplasia, dwarfism, obesity, insulin resistance, chronic kidney disease, heart diseases, and of course cancer, as FGF signaling usually acts as survival, proliferation or angiogenesis signal (92-95).

### 1.3.3 Fibroblast Growth Factor 2

FGF2, also known as basic FGF, does not contain any signal sequence for secretion yet is able to leave cells following type I UPS. There are five isoforms of FGF2, produced from the *FGF2* gene by alternative splicing, with a molecular weight ranging from 18 to 34 kDa. They are divided into low molecular weight (LMW) with 18 kDa and high molecular weight FGF2s (HMW) with 22, 22.5, 24, and 34 kDa (96). The isoforms share the same structural core of 12 antiparallel β-sheets but differ in their terminal regions. While all isoforms contain a C-terminal nuclear localization signal (NLS), only the HMW isoforms contain a conventional N-terminal NLS, with the 34 kDa isoform of FGF2 containing a second arginine-rich NLS (97). These differences determine the subcellular localization of FGF2 isoforms to either the cytosol or the nucleus, with the LMW form mostly being localized to the cytosol and HMWs to the nucleus (98).

The LMW isoform of FGF2, from here on just called FGF2, predominantly binds to FGFRs 1 (isoform IIIc) but also has been reported to interact to a lesser extent with FGFR1-IIIb, FGFR2-IIIc, and FGFR4 (95, 99-102). FGF2 signaling can be autocrine and paracrine and affects various physiological processes. Examples are the regulation of the proliferation of fibroblasts (103), organ development, cell differentiation, and migration (104). FGF2 is also able to inhibit apoptosis and stimulate cell proliferation, acting as survival signal in many cell types, making it a potent mitogen that has already been associated with tumorigenesis, metastasis formation, and tumor survival (105).

Since the discovery of FGF2 in the 1970s (106), it was amongst the first to be found in the extracellular space despite the lack of a signal peptide (107). Crystal structures of FGF2 were available in the early 1990s and solved by multiple groups (108-110). Since then, many important steps in the type I UPS of FGF2 have been unraveled.

To better understand the mechanism of FGF2 UPS, we first need to look at the most important structural features of FGF2. It is a very basic protein, with an isoelectric point of 9.6. There are four cysteines, three of which are accessible on the protein's surface. Of those three, C77 and C95 are unique to FGF2 and are absent in all signal sequences containing FGFs. These two cysteines have already been mutated to serins in early crystallography studies to solve the structure of FGF2 and play a significant role in proper FGF2 secretion (111). FGF2 has a high-affinity binding pocket specific for $PI(4,5)P_2$ consisting of lysine 127, arginine 128, and lysine 133 (112). Very interesting for the secretion mechanism, the three residues for $PI(4,5)P_2$ binding are also part of the heparin sulfate binding site. Heparan sulfates have a higher affinity for FGF2 and outcompete $PI(4,5)P_2$, creating a mutually exclusive binding site (113). With these residues and features in mind, we can now delve into the unconventional secretion pathway of FGF2.

The secretion of FGF2 requires sequential interaction with several factors at the inner leaflet of the plasma membrane. First, FGF2 binds directly to the cytosolic α1 domain of the Na,K-

ATPase, more specifically to the α1-subCD3 subdomain. The binding of FGF2 to α1-subCD3 was intensively analyzed by NMR, biochemical, and *in silico* experiments, and FGF2 residues K54 and K60 were identified to be crucial for this interaction (114). One of the surface cysteines, C77, was also associated with binding to α1-subCD3. C77A replacements caused a phenotype of reduced membrane recruitment and secretion (115). Using bioluminescence interferometry, it was then clearly shown that C77 is directly involved in binding to α1-subCD3. In contrast, C95 does not play a role in the FGF2 — α1-subCD3 interface (111). FGF2 secretion can, at this stage, be blocked by the Na,K-ATPase inhibitor ouabain and reversed by expression of ouabain-resistant Na,K-ATPase mutants (116).

Subsequently, Tec kinase phosphorylates FGF2 at Y81 (117). Direct interaction between FGF2 and Tec kinase has been revealed by biochemical pulldown assays, and small molecule inhibitors of this interaction inhibit FGF2 secretion (118). Furthermore, Tec kinase knockdown in HeLa cells by siRNA and inhibition of Tec kinase by LFM-A13 in 3T3 fibroblasts showed impairment of FGF2 secretion. In addition, Tec kinase has also been linked to regulating the type I unconventional secretion of FGF2 and FGF12 from U2OS cells (75). However, the precise role of Tec kinase in the unconventional secretion of FGF1, FGF2, and FGF12 needs further investigation.

After recruitment to the plasma membrane, FGF2 makes direct physical contact with the phosphatidylinositol $PI(4,5)P_2$ via the before-mentioned basic residues K127, R128, and K133 (112). *In silico* studies on FGF2 binding to $PI(4,5)P_2$ at the cytosolic leaflet of the plasma membrane revealed a second, lower affinity binding site for $PI(4,5)P_2$ in close proximity to the high-affinity binding site, assisting membrane binding to $PI(4,5)P_2$ (113). Bound to the membrane, FGF2 undergoes oligomerization, the key step required for pore formation and membrane insertion (32). This oligomerization requires disulfide bridge formation and is unique to FGF2 in the FGF family due to its surface cysteines C77 and C95 (119).

FGF2 secretion is then completed from the membrane-inserted oligomer by membrane-proximal HSPGs and extraction of FGF2 by heparan sulfate chains, outcompeting $PI(4,5)P_2$ at the mutually exclusive binding site, making the secretion an irreversible, directed process. Amongst the diverse subclasses like syndecans, perlecans, glypicans, and more, it was found that glypican-1 (GPC1) is the key rate-limiting factor driving the UPS of FGF2 (34). The importance of GPC1 for FGF2 secretion was linked with its enrichment of N-sulfated disaccharides in the heparan sulfate chains. The minimal length of heparin oligosaccharide to bind FGF2 was determined by NMR spectroscopy and consists of 8 monosaccharide units (120). Once fully translocated, FGF2 remains bound to HSPG clusters at the cell surface and can exert its signaling function (121). If HSPG heparan sulfate chain sulfation is blocked by $NaClO_3$ treatment, FGF2 surface concentration and secretion are drastically reduced (122). An important feature of FGF2 translocation compared to classical translocation across a membrane, e.g., into ER or across mitochondrial membranes, is that FGF2 has to be fully folded and functional to bind to HSPGs (123).

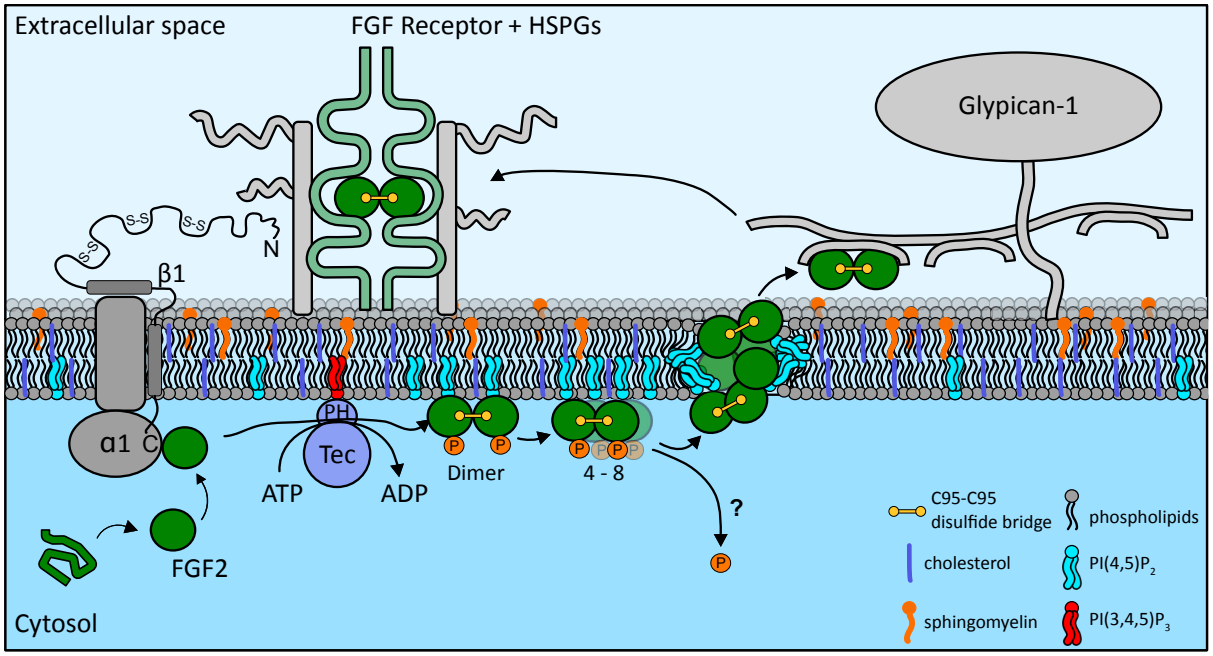


**Figure 2: The unconventional secretory pathway (UPS) type I of FGF2.** FGF2 is recruited to the membrane via the cytosolic α1 domain of the Na,K-ATPase. Subsequently, FGF2 is phosphorylated by Tec kinase and binds to PI(4,5)$P_2$ at the inner leaflet of the plasma membrane. Here, C95-dependent oligomerization occurs, ultimately leading to pore formation and membrane insertion. Translocation is completed by membrane-proximal heparan sulfate chains from HSPGs, specifically glypican-1. Retained at the cell surface by HSPGs, FGF2 can exert its function in an autocrine and paracrine manner. Adapted from (34).

The entire secretion process of a single translocation event, from recruitment at the plasma membrane to translocation across the membrane, could be observed in a time-resolved manner using fluorescence microscopy live-cell imaging. It was discovered that this process only takes around 200 ms (124). FGF2 translocation was also successfully reconstituted with purified components in an *in vitro* system. The required minimal components for the translocation are, besides FGF2, PI(4,5)$P_2$-containing liposomes with incorporated long-chain heparin (lc-heparin, mimicking cellular heparan sulfates) (113). In these systems, translocation is much slower and in the range of minutes to hours (32).

Key differences between the *in vitro* system and translocation from cells are the lipid asymmetry of the plasma membrane, the membrane potential, and, of course, the entirety of membrane proteins and membrane-associated proteins in the cellular context. With these in mind, it is no great surprise that such a large difference in translocation dynamics can be observed between cellular and *in vitro* translocation.

## 1.4 Properties of the Phosphoinositide PI(4,5)$P_2$

Absolutely essential for FGF2 binding to the membrane is the presence of PI(4,5)$P_2$ in the membrane, both in cellular and *in vitro* context. PI(4,5)$P_2$ is a minor, yet critical phospholipid in the plasma membrane of eukaryotic cells, with around 1 % of the total phospholipid content resident in the inner leaflet of the plasma membrane (125).

$PI(4,5)P_2$ is a key regulator in plasma membrane processes. Some examples are membrane trafficking, cytoskeletal organization, cell polarization, cell migration, membrane fusion, as cofactor in ion channel regulation, direct signal transduction, or as precursor of diacylglycerol (DAG) and $PI(3,4,5)P_3$ signaling (126-131). These varying functions are also thought to be linked to $PI(4,5)P_2$'s presence in membrane regions with different lateral organization, as $PI(4,5)P_2$ is present as freely-diffusing lipids, in smaller transient clusters, and large stable aggregates (130, 132). The lateral distribution can be regulated by $PI(4,5)P_2$ interacting proteins as well as multivalent cations (discussed below in detail) (127, 129, 132, 133).

I want to point out important features of $PI(4,5)P_2$ and their effect on membrane curvature and lipid sorting. From a classical perspective, $PI(4,5)P_2$ was thought to induce positive curvature (curvature facing towards the cytosol) due to the large, negatively charged phosphatidylinositol headgroup (-4 at physiological conditions) (134). However, the effect of $PI(4,5)P_2$ on membrane curvature is more complex. $PI(4,5)P_2$ is able to form strong hydrogen bond networks with itself despite the charge repulsion, and interact with other lipid types, such as PE, which also affects the $PI(4,5)P_2$ headgroup protrusion (135, 136). Multivalent ions such as $Ca^{2+}$ are able to bind to several $PI(4,5)P_2$ lipids at once, induce local clustering and also negative membrane curvature (137). And in addition, proteins like caveolin-1 or I-BAR (Bin-Amphiphysin-Rvs) bind to $PI(4,5)P_2$ and are known to induce negative membrane curvature (132, 138).

Multivalent ions like magnesium, calcium or aluminum were shown to promote $PI(4,5)P_2$ cluster formation. This was demonstrated by using a fluorescent $PI(4,5)P_2$ variant, labeled with a BODIPY analogue at the sn2 fatty acyl chain level (TopFluor®-$PI(4,5)P_2$), which self-quenches upon $PI(4,5)P_2$ clustering (139-141).

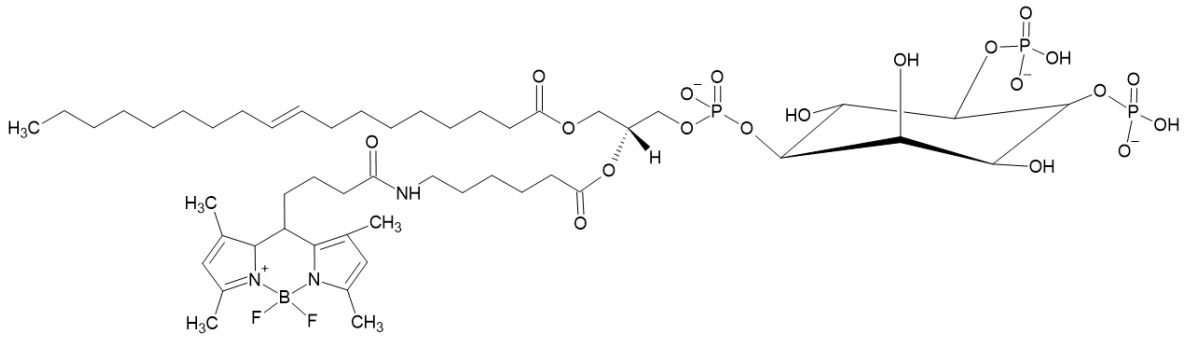

**Figure 3: TopFluor®-$PI(4,5)P_2$.** $PI(4,5)P_2$ analogue, fluorescently labeled at the sn2 acyl chain. Fluorescence is self-quenched upon clustering of the TopFluor® lipid. Excitation: 495 nm, Emission: 503 nm. CAS number: 1246355-57-6.

TopFluor®-$PI(4,5)P_2$ was also used to investigate protein-induced lipid clustering. Yi Wen *et al.* addressed the question of how HIV-1 particle membranes are able to contain a higher concentration of $PI(4,5)P_2$ compared to the plasma from which they bud (142). The study focused on interactions between $PI(4,5)P_2$ and HIV-1 Gag, the protein driving budding of new virus particles through oligomerization, and its myristoylated matrix (MA) domain. The MA

domain specifically binds to $PI(4,5)P_2$ and promotes incorporation of the viral envelope (Env) glycoproteins into budding virus particles(143).

By pre-clustering $PI(4,5)P_2$ in model membranes using multivalent cations, they demonstrated that Gag selectively binds to these clusters, leading to further enrichment of $PI(4,5)P_2$ at this site. This enrichment depends on Gag oligomerization. Furthermore, myristoylation of MA domain was identified for this selective binding to pre-clustered $PI(4,5)P_2$. Lack of N-terminal myristoylation shifted binding preferences towards free $PI(4,5)P_2$ (144). Interestingly, binding to pre-clustered $PI(4,5)P_2$ was restored through artificial pre-oligomerization of non-myristoylated MA by fusion to the carboxysome shell protein Ccmk4, which forms homo-hexamers in solution (145). It was hypothesized that multivalent $PI(4,5)P_2$-binding sites are able to displace the ions and access $PI(4,5)P_2$ for binding.

Strengthening this hypothesis, Bilkova *et al.* provided evidence of phospholipase C delta 1 pleckstrin homology domain (PLC δ-1 PH, short PH) being sensitive to the membrane state. The PH domain contains a single, specific $PI(4,5)P_2$ binding site, and binding to model membranes was almost completely inhibited in the presence of $Ca^{2+}$ ions. With Molecular Dynamics simulations, it was observed that calcium ions cause $PI(4,5)P_2$ headgroup tilt and reasoned this as cause for the abolished PH domain binding to model membranes (146). Despite these insights, the exact mechanism underlying protein preference for free versus clustered $PI(4,5)P_2$ remains unclear. These findings, however, emphasize the influence of $PI(4,5)P_2$'s lateral organization in the membrane in modulating protein binding.

Another study by Allolio *et al.* used Molecular Dynamics simulations to further look into the role of calcium ions, specifically in its ability to cause protein-independent membrane fusion if negatively charged lipids as $PI(4,5)P_2$ or phosphatidylserine (PS) are present (147-149). In those membranes, $Ca^{2+}$ induces negative curvature. In neutral membranes or with other negatively charged lipids as the ganglioside GM1, $Ca^{2+}$ only slightly effects membrane curvature. The increased negative curvature was pointed down to extended long-range cluster formation of the respective lipids by $Ca^{2+}$, which binds tightly to the $PO_4$ headgroups bridging those lipids into a network (137). Allolio *et al*. moreover looked into $Ca^{2+}$-mediated membrane fusion and calculated that the $Ca^{2+}$-induced lipid clustering leads to increased membrane tension, Gaussian bending modulus and reduced hydration repulsion, promoting negative curvature and association of respective lipids in the fusion stalk area (137).

To conclude, $PI(4,5)P_2$ is a central regulatory lipid in the cytosolic leaflet of the plasma membrane. However, how $PI(4,5)P_2$ is involved in this many processes remains unclear. Proteins like HIV-1 Gag demonstrate the ability to not only bind to a specific local population of clustered $PI(4,5)P_2$ lipids, but also enhance $PI(4,5)P_2$ clustering upon oligomerization. Similarly, FGF2 binds to $PI(4,5)P_2$ and oligomerizes. My aim is to whether FGF2 oligomerization influences the local $PI(4,5)P_2$ concentration in the membrane, potentially inducing membrane remodeling and curvature. This could provide insights into the biophysical basis for the observed pore formation and determine the main driving force for FGF2 membrane translocation.

## 1.5 Molecular Dynamics Simulations

MD simulations have been around since the 1950s and have evolved with increasing numbers of structural information and computational power from simulations of simple gases to more complex molecules and finally proteins in the late 1970s (150, 151). The first all-atoms simulation of a protein, bovine pancreatic trypsin inhibitor, was done in vacuum and reached a simulation time of 9.2 ps. Today, MD simulations benefit greatly from the massive increase in computational power of modern super computers and are comfortably able to reach the microsecond range, with the millisecond range soon to be reached. Further technical advances in recent graphics processing units (GPUs) and more user-friendly MD simulation software also allow users to run MD simulations in-house with at a relatively affordable cost (152).

MD simulations became an indispensable tool in the study of molecular systems, offering a detailed view into the molecular level of (macro-) Molecular Dynamics over time, unreachable by any other method so far. The level of detail can range from simulating every single atom (all-atoms), to super coarse-grain systems, where the membrane of an entire cell is simulated by coarse-graining the membrane into meshes.

The underlying principle of MD simulations is to determine the time evolution of atom positions and velocities by applying Newton's equations of motion. In classical MD simulations, electrons are neglected based on the Born-Oppenheimer approximation (153). It states that the motion of the much heavier nuclei can be separated from the motion of electrons. For this reason, bonds cannot be formed or broken and protonation states are fixed in classical MD simulations. Newton's equations of motions are numerically integrated over time for every particle in the system.

$$\mathrm{F} = m\mathrm{a} \tag{1}$$

F is the total force acting on a particle with mass m, and a is the resulting acceleration.

$$\mathrm{a} = \frac{\delta v}{\delta t} \tag{2}$$

Acceleration a can be described as change of velocity v over time t.

$$\mathrm{v} = \frac{\delta r}{\delta t} \tag{3}$$

And velocity v is the change in position of the particle over time t.

In practical terms, the software calculates all the forces between particles in an iterative way using fixed time steps (Δt) for a very large number of times, moving the particles accordingly after each time step. This results in a trajectory of particle movement of all observed particles in the chosen time window. The time step is limited by the fastest oscillations in the system, typically oxygen-hydrogen bond vibrations, leading to a standard time step of 2 fs in all-atom simulations of proteins and lipids. The algorithm used in this work to then integrate the

equations of motions for all calculated forces to determine the new particle positions is called the leap-frog algorithm (154). The principle of this algorithm is to calculate the velocities in half-time steps (t + Δt/2) and the positions are updated only every time step (t + Δt), so update either velocities or positions, but not at the same time. This gives increased numerical stability and computational efficiency for larger MD simulations.

$$\vec{r_i}(t + \Delta t) = \vec{r_i}(t) + \vec{v_i}\left(t + \frac{\Delta t}{2}\right)\Delta t \tag{4}$$

$$\vec{\mathrm{v_i}}\left(\mathrm{t} + \frac{\Delta \mathrm{t}}{2}\right) = \vec{\mathrm{v_i}}\left(\mathrm{t} - \frac{\Delta \mathrm{t}}{2}\right) + \frac{\vec{\mathrm{F_i}}(\mathrm{t})}{2\mathrm{m_i}}\Delta \mathrm{t} \tag{5}$$

The framework used to calculate the forces between particles in each step is given in the force field, a set of empirical parameters describing all bonded and non-bonded interaction between particle types within a molecular system. Bonded interactions include the bonds, angles and torsions between atoms. Bonds are typically treated like a classical spring. A harmonic potential is used to keep the bonded atoms at optimal distance, exerting force when the distance between atoms is not at the reference distance. Similarly, angles between bonded atoms are treated with a force constant, letting the bonded atoms oscillate around the reference angle. Both oscillations are based on Hook's law (155):

$$V_{(bond)} = \frac{1}{2}k_b(r - r_0)^2 \tag{6}$$

$$V_{(angle)} = \frac{1}{2}k_b(\Theta - \Theta_0)^2 \tag{7}$$

Non-bonded interactions include Van-der-Waals (VdW) forces and electrostatic interactions which are calculated by Leonard-Jones potential and Coulomb's law, respectively.

VdW forces are created by the formation of transient dipoles between proximal molecules. The Leonard-Jones (156), or 12-6 potential describes the repulsive and attractive forces between intermolecular pairs. If the distance between molecules is too short, repulsive forces dominate that decay with distance inversely proportional to $r^{12}$, with r being the distance between molecules. Attractive VdW forces are very short-ranged, typically from a few Angstroms to about 1 nanometer, and decay rapidly with $r^6$.

Electrostatic interactions are calculated using Coulombs law (157) where the electrostatic force is the quotient of the strength of charges $q_1$ and $q_2$ of the respective particles divided by the distance to the power of 2, and multiplied by the Coulomb constant $k_e$.

$$F = k_e\frac{q_1 q_2}{r^2} \tag{8}$$

To keep the computational cost for the long-ranged, slow-decaying electrostatic interactions low, electrostatic interactions are calculated with the Particle Mesh Ewald (PME) method for all-atoms and reaction field (RF) method for Martini coarse-grained simulations (158, 159). Both, PME and RF methods calculate all electrostatics explicitly within a given cut-off radius between particles, typically 1.2 nm. In RF methods, beyond this threshold, atoms collectively contribute to a smooth, uniform electrostatic environment, also called dielectric continuum. This force acts equally on all atoms within the simulation box regardless of individual positions and charges. In the Particle Mesh Ewald (PME) method, charges are interpolated onto a 3D grid and transformed into reciprocal space using a Fourier transform (160) to simplify electrostatic calculations. An inverse Fourier transform then converts the data back into real space, where it is mapped onto the particles. This approach enhances the accuracy of long-range interaction calculations. The sum of bonded and non-bonded interactions, or intra- and intermolecular energies results in the potential energy U.

$$\mathrm{U} = \text{Intrameolcular energies} + \text{Intermolecular energies} \tag{9}$$

The total forces are then calculated from the negative gradient of the potential energy:

$$\vec{F_i}(x) = -\Delta U_i(x) \tag{10}$$

There are different force fields like AMBER, CHARMM36 and GROMOS, which are each optimized for distinct molecular systems, e.g. AMBER is mostly used for protein-DNA interactions and CHARMM36 for membrane systems and lipids. For my work, I use the CHARMM36 (161, 162) and Martini2.2 (163, 164) force-fields for accurate predictions of my all-atoms and coarse-grain systems, respectively.

The choice of particle resolution is a very important one and several questions have to be addressed when choosing the most suited resolution for the given biological problem. All-atoms representations of molecules represent every single atom as a bead with specific parameters which were adapted to match experimental results of molecule behavior. If one aims for the correct atomistic picture of molecules, this is the way to go. Yet, depending on the system size and time scale of the biological problem, it might not be feasible to reach these in all-atoms resolution. Nowadays, typical systems for all-atoms resolution contain around 1 million atoms, and reach 1 to 10 microseconds, up to 1 millisecond if the computational resources are available. These time scales might still be too short to observe some biological systems, like membrane reorganization.

To overcome these limitations of system size and time scale, we can reduce the resolution of molecules. Meaning, we can simplify the particles by combining atoms into beads. The Martini model maps 4 heavy atoms, ignoring hydrogen atoms, into a single bead. Thereby, a particle reduction of 80 to 90 % can be achieved compared to all-atoms resolution. In addition, the

time steps during the simulation can be greatly enlarged up to 20 fs, a factor of 10 over all-atoms simulations. With this, the performance of simulations can be increased by a factor of 10 to 100 times. All beads of the Martini model have the same mass, but are distinguished into four types of beads: polar, intermediate polar, apolar, and charged. Their Leonard-Jones interactions are calculated based on an interaction matrix, which gives pairs of beads fixed interaction strengths reaching from super attractive to super repulsive. The Martini2.2 model is widely used to simulate biological membranes and proteins nowadays. Yet, studying systems with two or more proteins has to be treated with special care as the Martini model overestimates protein-protein interactions (165). Meaning, predicted protein-protein interaction interfaces may be incorrect even though free energy calculations might be correct.

Once the choice of force-field, resolution and type of system is made, a simulation box with a finite volume containing all particles is created. To avoid artificial boundary effects of particles leaving the simulation box, where particles would be on one side in contact with particles and on the other side in contact with vacuum, the simulation box is surrounded by identical copies of itself. This is called periodic boundary condition (PBC) (166). Based on the finite simulation box, an effectively infinite system is created, but only the nearest copies are taken into consideration for calculations (minimum image conversion). In practical terms, particles leaving the simulation box on one side will reappear on the opposite site of the box under PBC. This allows for conservation of thermodynamic properties and potential energy within the simulation. The PBC is especially useful for simulating membranes as PBC creates a planar, continuous lipid bilayer to study. In two special cases, PBC should be handled with care. One is the simulation of (artificially) curved membranes. The other is the visualization of natural membrane undulations, which require a certain minimal size of the membrane patch in one simulation box (167).

The simulation box with its confined volume and particles resembles a microcanonical ensemble from a thermodynamical point of view. This is characterized by a constant number of particles N, constant volume V, and constant total energy E of the system (NVE). As MD simulations want to mimic experimental setups, a different ensemble has to be chosen, as volume and total energy cannot be controlled easily. What can be controlled more easily on the other hand are temperature and pressure. Therefore, the NVT (constant: particles, volume, temperature; canonical ensemble) or NpT (constant particles, pressure, temperature; isothermal – isobaric ensemble) are employed (168). The NPT ensemble is particularly used to mimic biological conditions because most biological systems operate under constant pressure (e.g., 1 atm) and temperature (e.g., 300 K) in a flexible environment, where the volume can fluctuate to accommodate natural pressure variations. This allows simulations to better replicate realistic physiological conditions (169).

The temperature of a classical MD simulation system is directly linked to the velocity of particles, more precise the kinetic energy. To keep the temperature constant, one could simply rescale the velocities of particles in the system. This is done by the Berendsen thermostat

(170), which rescales the velocities in periodic time intervals $\tau_t$ to match the reference temperature $T_0$:

$$\frac{dT}{dt} = \frac{T_0 - T}{\tau_t} \tag{11}$$

This elegant, yet simple rescaling performed by the Berendsen thermostat ensures stability and fast temperature equilibration of the simulations. Though, it is usually only used during equilibration because it suppresses natural fluctuations in the temperature that should occur in an NVT ensemble due to its coupling to the reference temperature (also called “bath” from experimental thermodynamics studies). A much more sophisticated, but also more precise algorithm is provided by the Nosé-Hoover thermostat (168, 171). Instead of strict rescaling, the Nosé-Hoover thermostat couples the system dynamically to the fictitious heat bath, allowing a more dynamic flow of energy. This allows the systems to explore the correct Maxwell-Boltzmann distribution of kinetic energy at the given temperature (172, 173).

Different algorithms exist for pressure control (pressure coupling) in MD simulations, similar to temperature control. The Berendsen barostat, like its thermostat counterpart, rescales the pressure in the simulation in constant time intervals (170). Like the thermostat, it is not suitable to reproduce the correct NpT ensemble behavior, either, and is mostly used for fast, stable equilibration of systems. A more suitable algorithm is provided by the Parrinello-Rahman barostat, commonly used for production runs, as it correctly reproduces the NpT ensemble (169). There are three ways the pressure can be controlled which has to be carefully chosen, depending on the type of system. Isotropical pressure coupling treats the x-y-z dimensions equally and is used for pure liquid simulations. The z-dimension can also be uncoupled from x and y so that both sets can change their sizes independently, which is called semi-isotropic, required for membrane simulations and the most prominent pressure coupling in this work. In anisotropic pressure coupling, x-y-z dimensions are independent from each other. This can also be used for membrane simulations and for specific box shapes.

Overall, MD simulations have become a very potent tool to investigate biological systems at the molecular level, providing both explanation for experimental observations, and guidance and predictions for experiments.

In this work, MD simulations will be applied in both coarse-grain and all-atoms resolution to uncover molecular details of FGF2 secretion at the molecular level. For this, insights from many years of experimental research will guide my simulations to mimic the biological process of FGF2 secretion at the membrane as closely as possible, which will be described in the next section.

## 1.6 FGF2 membrane translocation – Key features of FGF2 oligomerization and pore formation

In the late 2000s, Temmerman *et al*. identified $PI(4,5)P_2$ as crucial component for FGF2 membrane translocation in the plasma membrane. A high-affinity binding site of FGF2 towards $PI(4,5)P_2$, consisting of the residues K127, R128 and K133 was unveiled. Mutations in these residues caused a loss of binding of FGF2 towards $PI(4,5)P_2$-containing membranes (112). Membrane binding of FGF2 to $PI(4,5)P_2$-containing membranes was further validated by all-atoms MD simulations, revealing secondary, low-affinity binding sites for $PI(4,5)P_2$, which are thought to promote initial contact with the membrane (113).

Biochemical reconstitution experiments on model membranes in the early 2010s revealed that $PI(4,5)P_2$ is essential for FGF2 oligomerization and pore formation (32). Pore formation was detected using a fluorescent tracer molecule, small enough to enter through the FGF2-induced pore into the liposome vesicles. Interestingly, a $His_6$-tagged version of FGF2 did not show these properties on liposomes when recruited trough Ni-NTA lipids.

FGF2 binding behavior at the membrane is also affected by cholesterol. Super resolution microscopy using the stimulated emission depletion technique revealed colocalization of doxycycline-induced recombinant FGF2-Halo and cholesterol-rich membranes areas, detected by GRAM1b (174). In addition, increasing the cholesterol concentration of the plasma membrane with cholesterol-loaded methyl-β-cyclodextrin enhanced FGF2 membrane recruitment at the inner plasma membrane as well as membrane translocation to the extracellular space. It was hypothesized, using MD simulations, that cholesterol increased $PI(4,5)P_2$ headgroup visibility on the membrane by exposing the negative charge, which translated into faster binding kinetics and stronger binding, by lowering the free binding energy about -15 $k_bT$ in the presence of cholesterol (174).

The surface cysteines C77 and C95 were suspected to be involved in FGF2 oligomerization. Mutation of C77 to alanine moderately reduced FGF2 secretion efficiency in CHO cells, while C95A led to a 65 % decrease in FGF2 secretion. The double mutant C77/95A showed an almost complete loss of secretion activity in CHO cells (111).

*In vitro* pore formation experiments on giant unilamellar vesicles (GUV) and kinetic measurements of pore formation on large unilamellar vesicles (LUV) showed further confirmed these findings, with C95A and C77/95A showing significantly impaired pore formation abilities. Recent fluorescence correlation spectroscopy combined with brightness analysis on GUVs showed that the average oligomeric size of FGF2-GFP (green fluorescent protein) on $PI(4,5)P_2$-containing membranes was 4 to 8. While FGF2-GFP-C77A exhibited a similar oligomerization behavior as the wildtype FGF2-GFP (wtFGF2-GFP), both FGF2-GFP-C95A and FGF2-GFP-C77/95A mutants completely lost the ability to oligomerize.

These findings were used in my MD simulations and provided a rationale for their starting conditions. In all-atoms MD simulations, FGF2 consistently bound from the solvent to the

membrane with PI(4,5)$P_2$ in the high-affinity binding. This initial binding step is skipped and my simulations started with FGF2 pre-bound to the membrane with a single PI(4,5)$P_2$ molecule occupying the high-affinity binding site. Additionally, experimental data suggest FGF2 dimerization via C95-C95 disulfide bridge formation. To reflect this, simulations involving FGF2 dimers were covalently linked between the two C95 residues (111).

Scanning electron microscopy of FGF2-GFP complexes on flat, supported lipid bilayers provided structural insights into FGF2 oligomerization (unpublished data). These FGF2-GFP oligomers showed a non-uniform variety of shapes, some more square-shaped and some hexagonal. However, a common characteristic across all structures was their size, around 20 nm in diameter, and the presence of a small hole in the center of the oligomeric structure.

## 1.7 Aim of this thesis

Many key aspects of FGF2 secretion have been thoroughly investigated and uncovered. The secretion of FGF2 in cells depends on the presence of the Na,K-ATPase, Tec kinase, PI(4,5)$P_2$ at the inner plasma membrane leaflet, and GPC1, a heparan sulfate proteoglycan at the extracellular surface of the plasma membrane. *In vitro* studies using a minimal component system on GUVs have shown that PI(4,5)$P_2$-containing membranes are sufficient for pore formation, and complete FGF2 translocation across the GUV membrane was reconstituted with luminal long-chain heparin. Additionally, fluorescence brightness analysis using fluorescence correlation spectroscopy determined the average oligomeric size of FGF2 complexes on membranes to be 4 to 8 monomers.

These findings support the hypothesis that oligomerization of FGF2 on PI(4,5)$P_2$-containing membranes is sufficient to drive membrane pore formation. This thesis aimed to uncover the molecular mechanisms driving FGF2 oligomerization and determine the driving force of membrane pore opening along with the insertion of FGF2 oligomers into the plasma membrane.

# 2 Materials and Methods

## 2.1 Hardware and Software

Workstation:
Linux Manjaro OS system v 6.6.54-2, CPU: 2 x AMD Threadripper , 2 x Nvidia GeForce RTX 2080 Ti, 2 x Intel® Xeon® Gold 6130 @ 2.10 GHz, 16 x Micron 16GB 2Rx4 PC4-2133P-R DDR4 Registered Server-RAM Modul REG ECC - MTA36ASF2G72PZ-2G1A2

Supercomputer:

bwForCluster Helix

GROMACS versatile package to perform Molecular Dynamics simulations
Used Versions: 2021-4, 2022-6, 2023-1, 2024-2, 2021-4-plumed-2.7.3 modified version

MOSAICS tool to characterize and analyze structure and dynamics of membrane system
Used version: 1.0

MemSurfer tool to compute and analyze membranes
Used version: 1.1

Python3

MDAnalysis
Used version: 2.7.0

Martinize2

BumPy

Charmm-Gui

## 2.2 Computational Methods

Lipid bilayers (all-atoms and coarse-grained) were created using the Charmm-Gui web interface (charmm-gui.org, Leigh University). For coarse-grained lipids not deposited in the Charmm-Gui databank, topology files of the desired fatty acids were manually built according to the building blocks of lipid molecules in Martini2.2.

From previous simulations, it is known that FGF2 will move from water and bind to PI(4,5)$P_2$ molecules in the membrane with the high-affinity binding site. To save simulation time, I always start all-atoms and coarse-grain simulations with FGF2 already bound to the lipid bilayer with a PI(4,5)$P_2$ molecule in the high-affinity binding pocket.

### 2.2.1 Coarse-grain Martini2.2 simulations

Proteins were coarse-grained using the martinize2 tool with the elnedyn22 forcefield for elastic network creation. The command for martinize2 was:

```
martinize2 -f input.pdb -o topo.top -x output.pdb -p backbone -ff elnedyn22 -elastic -ef 700.0 -el 0.5 -eu 0.9 -cys auto -dssp <path-to-mkdssp>
```

The parameters -ef, -el and -eu were used for the elastic network. Cysteine bridges were automatically detected with -cys auto. The dssp package was used to determine the secondary structures of the proteins.

10 % of regular water beads were exchanged with antifreeze water beads, as water tends to freeze and form crystalline structures at much higher temperatures than expected, especially in membrane systems (163).

If not stated otherwise in the subsequent sections, coarse-grained systems were minimized and equilibrated the same way. Minimization was performed with the steepest-decent algorithm with these parameters:

```
integrator              = steep
nsteps                  = 1000
tinit                   = 0.0
emtol                   = 400

nstlog                  = 5000
nstenergy               = 100

cutoff-scheme           = Verlet
```

```
nstlist                  = 20
ns_type                  = grid
pbc                      = xyz
verlet-buffer-tolerance  = 0.005

epsilon_r                = 15
coulombtype              = reaction-field
rcoulomb                 = 1.1
vdw_type                 = cutoff
vdw-modifier             = Potential-shift-verlet
rvdw                     = 1.1
```

For equilibration, multiple short simulations with 1 ns duration were performed with decreasing forces for position restraints and increased time-steps for 2 to 20 fs. The final step of equilibration was performed for 100 ns. During equilibration, temperature and pressure were controlled using the V-rescale and Berendsen algorithms to keep temperature and pressure constant at 310 K and 1 atmosphere with a coupling constant of 1 ps and 5 ps, respectively. For membrane-containing systems, semi-isotropic pressure coupling was chosen. The cut-offs for Coulomb and Van-der-Waals forces were set to 1.1 nm.
As was reported in 2023 by Kim *et al. (175),* using standard CHARMM-GUI parameters for production simulations can lead to curvature-artifacts in very large membranes. Therefore, I included the suggested, which are setting the verlet-buffer-tolerance to -1 and rlist to 1.35. For production, simulations were run for at least 10 µs and I applied a timestep of 20 fs with the V-rescale thermostat and the Parrinello-Rahman barostat with a time constant of 12 ps and semi-isotropic pressure coupling. Exemplary parameters are given below:

```
integrator               = md
dt                       = 0.02
nsteps                   = 500000000

nstlog                   = 50000
nstenergy                = 50000
nstxout-compressed       = 50000
compressed-x-precision   = 100
nstcalcenergy            = 100

cutoff-scheme            = Verlet
nstlist                  = 20
ns_type                  = grid
pbc                      = xyz
verlet-buffer-tolerance  = -1
rlist                    = 1.35
epsilon_r                = 15
```

```
coulombtype              = reaction-field
rcoulomb                 = 1.1
vdw_type                 = cutoff
vdw-modifier             = Potential-shift-verlet
rvdw                     = 1.1

tcoupl                   = v-rescale
tc-grps                  = membrane protein solvent
tau_t                    = 1.0      1.0     1.0
ref_t                    = 310      310     310

Pcoupl                   = Parrinello-Rahman
Pcoupletype              = semiisotropic
Tau_p                    = 12.0
Compressibility          = 4.5e-5  4.5e-5
ref_p                    = 1.0     1.0
```

#### 2.2.1.1 Curvature – PI(4,5)$P_2$ and FGF2 diffusion along curved membranes

Coarse-grained membranes were created from a small patch of membrane, created with Charmm-GUI, and the tool BUMPy (176). It uses geometric transformations and area matching to create a plethora of different membrane shapes. Dummy particles were added to the according created membrane to keep the shape stable. These are mass-free particles, only interacting with the PC lipid headgroups to repel them from leaving the given shape via Leonard-Jones potentials.

I used a semicylinder_plane configuration to create a large system with both, positive and negative curvature as well as flat regions. The membrane was created with the following command:

```
python bumpy.py -f input.gro -s semicyliner_plane
-r_cylinder 60 -l_cylinder 100 -r_junction 60 -l_flat 60
-o out.pdb -p topol.top -n index.ndx --gen_dummy_particles
--dummy_grid_thickness 50 --dummy_name DUMY
```

#### 2.2.1.2 Preformed toroidal pores – PI(4,5)$P_2$ diffusion along lipid toroidal pores

To study lipid and FGF2 behavior in toroidal pores after pore formation, we used a shortcut to pre-form a toroidal pore and start the simulations an already pore-containing membrane. To open a toroidal pore, a flat-bottom restraint was applied to the PC lipids during the simulation. The potential is based on the following equation:

$$V_{\mathrm{fb}}(\mathbf{r}_i) = \frac{1}{2} k_{\mathrm{fb}} [d_g(\mathbf{r}_i; \mathbf{R}_i) - r_{\mathrm{fb}}]^2 H[d_g(\mathbf{r}_i; \mathbf{R}_i) - r_{\mathrm{fb}}],$$

If PC molecules entered the defined region of the flat-bottom restraint, a force acted on the last 2 beads of the acyl chains to push them out of the defined region. As PC was the main phospholipid component of the used membranes, a toroidal pore formed. The flat-bottom restraint was defined in the ".itp" topology file and followed the following general scheme:

```
#ifdef FLAT_BOTTOM
    [ position_restraints ]
;atom_number - type_of_restraint - Shape_of restraint - Radius - Force
    11  2   8   -4.5   FLAT_BOTTOM_FC
    12  2   8   -4.5   FLAT_BOTTOM_FC
    15  2   8   -4.5   FLAT_BOTTOM_FC
    16  2   8   -4.5   FLAT_BOTTOM_FC
#endif
```

The first number defined the atomic number on which the flat-bottom restraint acts on. The second number defines the type of restraint. The third number defines the shape of the restraint with 8 being a cylindrical shape in z-direction (orthogonal to the membrane). The fourth number defined the radius in nm and was varied to achieve different pore sizes. The force of the flat-bottom restraint was defined in the .mdp-options file and was set to 100 kJ/mol.

To study PI(4,5)$P_2$ diffusion, the membrane was made with only POPC and cholesterol lipids. PI(4,5)$P_2$ was placed in only one of the leaflets to mimic asymmetry of the cellular plasma membrane.

Screening of PI(4,5)$P_2$ diffusion around toroidal pores was performed with 4 varying parameters: cholesterol content of the membrane, pore size, PI(4,5)$P_2$ acyl chain types, PI(4,5)$P_2$ concentration.
Cholesterol concentration ranged from 0 to 40 % in 10 % increments. 2, 4, and 6 nm were chosen as pore sizes. PI(4,5)$P_2$ concentration ranged from 2.5 to 12.5 % of phospholipids in a single bilayer. For acyl chains, 18:0-18:0, 18:1-18:0, 18:1-18:1, and 18:0-20:4 was used.

#### 2.2.1.3 Preformed toroidal pores – FGF2 diffusion into toroidal pores

Coarse-grained FGF2 was embedded into the membrane with a single PI(4,5)$P_2$ molecule inside the high-affinity binding site by simple placing of the 2 molecules into the membrane. Proteins were placed on the "cytosolic" side containing free PI(4,5)$P_2$ lipids. Simulations were carried out with 1 to 4 FGF2 monomers at pore sizes of 2, 4 and 6 nm.

As protein-protein interactions are overestimated in the Martini2 forcefield, these interactions were reparametrized and scaled down to 80 % of normal strength (177). Production simulations were run for at least 10 µs with the toroidal pores already preformed.

### 2.2.2 All-atoms resolution Molecular Dynamics simulations

Proteins in all-atoms resolution were created from structures deposited in the Protein Data Bank (www.rcsb.org) with the Charmm-Gui web interface (178-192). The x-ray structure 1BFF was used here, with residues 26 to 154 being resolved (193). FGF2-FGF2 cysteine dimers were created by positioning 2 FGF2 monomers facing each other with C95s and using this structure as input for Charmm-Gui, selecting a disulfide bridge modification between the 2 C95s.

#### 2.2.2.1 FGF2 insertion into lipid bilayers

Insertion of single FGF2 monomers followed the universal method for embedding proteins into lipid bilayer (194). Briefly, the protein-to-be-inserted was placed in the vacuum besides the membrane. I performed a short simulation under high lateral pressure, applying positional restraints on the protein in all dimensions and z-direction restraints on the lipids, which led to the membrane sliding around the protein. Then, a short relaxation simulation was performed. To embed FGF2 into membranes, a single $PI(4,5)P_2$ molecule was already bound in the high-affinity binding site.

For simulations with several FGF2 monomers or FGF2 oligomers, a different approach had to be used, as the lipids below the protein could not mix leading to holes in the leaflet. Instead of pushing FGF2 with $PI(4,5)P_2$ into the membrane, all the bound $PI(4,5)P_2$'s were inserted without FGF2. Then, using VMD, FGF2 was aligned to the $PI(4,5)P_2$ molecules with the high-affinity binding site engulfing the $PI(4,5)P_2$ headgroup.

For both cases, water was added in a similar way by placing the proper amount of water (full hydration of the membrane and proteins) in the vacuum next to the protein-membrane system and applying high lateral pressure. Movement of water molecules in z-direction was restrained to prevent water molecules moving into the bilayer plane. The full system was then equilibrated for a total of 1.35 ns with decreasing position restraints on protein and lipids in every step.

#### 2.2.2.2 Machine learning-driven screening of the FGF2 dimer interface

Both monomers were embedded into the membrane as described before, facing each other with their respective C95s. To sample the interaction space, one of the monomers was rotated by 1° for 360° and kept at a constant distance of 0.8 nm to the non-rotating monomer. A Bayesian Gaussian mixture model (GMM)-based cluster analysis was used to identify the predominant dimerization interface in these simulations. Rotations and translations were fitted to one of the FGF2 monomers and its respective $PI(4,5)P_2$ lipid. The complexity of the

structural space was reduced from 3 to 2 dimensions to the C-alpha atoms using an artificial neural network-based autoencoder to ensure more robust clustering (195). An eight-component model was chosen for cluster identification with the Bayesian GMM.

#### 2.2.2.3 FGF2 self-assembly into higher oligomers

To study the self-assembly of FGF2 into higher oligomers, I embedded FGF2 monomers and FGF2 dimers into a simple membrane containing POPC, 30 % of cholesterol and 5 % of $PI(4,5)P_2$. The concentration of $PI(4,5)P_2$ was increased compared to the 2% biological $PI(4,5)P_2$ concentration in the plasma membrane to ensure that some $PI(4,5)P_2$ molecules remain in the bulk membrane rather than being entirely sequestered by FGF2. I either used 2 dimers and 2 monomers or 3 dimers, so 6 FGF2 monomers in total, according to experimental data about FGF2 oligomeric state in *in vitro* experiments (111). For each of the 2 systems, I created 30 different starting orientations with different orientations of the individual FGF2 monomers and/or dimers.

FGF2 Hexamer stability was simulated for at least 5 µs and 3 repeats on a complex, asymmetric membrane with a lipid composition adapted from (51). The cholesterol concentration was lowered to reduce membrane rigidity and enhance lipid diffusion.

**Table 1:** Lipid composition of the complex membrane used for FGF2 hexamer stability

| (Name) Acyl chain and type | Total number / Concentration | cytosolic | extracellular leaflet |
|---|---|---|---|
| (SOPC) 18:1 - 18:0-PC | 36 / 4,1 % | 72 / 7,9 % | |
| (PAPC) 16:0 - 20:4-PC | 0 / 0,0 % | 54 / 5,9 % | |
| (PIPC) 18:2 - 16:0-PC | 81 / 9,2 % | 162 / 17,7 % | |
| (dPPC) 16:0 - 16:0-PC | 18 / 2,0 % | 0 / 0,0 % | |
| (POPE) 18:1 - 16:0-PE | 27 / 3,1 % | 0 / 0,0 % | |
| (SAPE) 18:0 - 20:4-PE | 45 / 5,1 % | 42 / 2,7 % | |
| (PDOPE) 24:6 - 16:0-PE | 90 / 10,3 % | 0 / 0,0 % | |
| (PLA20) d18:1 - 20:4-PE | | | |
| (PAPS) 16:0 - 20:4-PS | 144 / 16,4 % | 0 / 0,0 % | |
| (SAPS) 18:0 – 20:4-PS | 9 / 1,0 % | 9 / 0,1 % | |
| (PSM) d18:1 – 18:0-SM | 9 / 1,0 % | 126 / 13,8 % | |
| (NSM) d18:1 – 24:1-SM | 0 / 0,0 % | 99 / 10,8 % | |
| (LSM) d18:1 – 24:0-SM | 0 / 0,0 % | 81 / 8,9 % | |
| (CHL1) Cholesterol | 257 / 29,3 % | 283 / 31,0 % | |
| (SAPI2) 18:0 – 20:4 $PI(4,5)P_2$ | 45 / 5,1 % | 0 / 0,0 % | |
| Total | 913 | 878 | |

#### 2.2.2.4 Membrane remodeling by membrane-bound FGF2 oligomers

As Lipid diffusion was extremely slow in FGF2-hexamer-containing all-atoms resolution MD simulations, I decided to go back to coarse-grain resolution to address the question whether FGF2 hexamers are able to cause local membrane remodeling. The lipid composition of the membrane was adapted by Schaefer and Hummer (51), mimicking the plasma membrane and was composed of 12 different lipid types, asymmetrically distributed (see Table 2: Lipid composition of cytosolic (FGF2-embedded) and extracellular leaflet. Notably, I used the highly unsaturated 18:0-20:4-PI(4,5)$P_2$ instead of the 18:1-18:0 acyl chains, as the 18:0-20:4 PI(4,5)$P_2$ is the naturally most abundant PI(4,5)$P_2$ species. Second, I used only 30 % compared to 40 % of cholesterol as the higher cholesterol concentrations would make the membrane too rigid and slow down diffusion. As the reference membrane was created in all-atoms resolutions, some lipids did not exist in Martini2.2, and were instead added as the most abundant phospholipid of the respective class. To monitor real lipid mixing, the FGF2 hexamer was placed – bound with 1 PI(4,5)$P_2$ molecule per monomer – into a patch of pure PC lipids surrounded by the complex lipid mixture. During equilibration, position restraints in xyz-dimensions were applied to FGF2 and PC lipids to prevent mixing of lipids at this stage.

**Table 2:** Lipid composition of cytosolic (FGF2-embedded) and extracellular leaflet

| Lipid Type (Martini2.2-Name) | Total number / Concentration | cytosolic | | extracellular leaflet | |
|---|---|---|---|---|---|
| (POPC) 18:1-16:0-PC | | 68 / | 4,4 % | 192 / | 12,5 % |
| (PAPC) 20:4-16:0-PC | | 0 / | 0,0 % | 87 / | 5,7 % |
| (PIPC) 18:2 – 16:0-PC | | 171 / | 11,2 % | 229 / | 14,9 % |
| (DPPC) 16:0 – 16:0-PC | | 24 / | 1,6 % | 0 / | 0,0 % |
| (POPE) 18:1 – 16:0-PE | | 45 / | 2,9 % | 0 / | 0,0 % |
| (PAPE) 20:4 – 16:0-PE | | 264 / | 17,2 % | 42 / | 2,7 % |
| (PRPE) 24:6 – 16:0-PE | | 147 / | 9,6 % | 0 / | 0,0 % |
| (PAPS) 20:4 – 16:0-PS | | 249 / | 16,3 % | 15 / | 1,0 % |
| (DPSM) d18:1 – 18:0-SM | | 15 / | 1,0 % | 204 / | 13,3 % |
| (PNSM) d18:1 – 24:1-SM | | 0 / | 0,0 % | 288 / | 18,7 % |
| (CHOL) Cholesterol | | 468 / | 30,5 % | 480 / | 31,2 % |
| (PAP2) 20:4 – 16:0 PI(4,5)$P_2$ | | 81 / | 5,3 % | 0 / | 0,0 % |
| Total | 1532 | | | 1537 | |

#### 2.2.2.5 Analysis for membrane remodeling

Lipid sorting was calculated for each leaflet individually. To separate the leaflets, the FATSLiM tool (**F**ast **A**nalysis **T**oolbox for **S**imulation of **Li**pid **M**embranes) was used with the “fatslim membranes” command (196). Each leaflet file was combined with the protein as the reference

for the analyzed membrane area. A self-written script in python was used using MDAnalysis to select the lipid patch and calculate enrichment/depletion for each lipid type (197). Lipids were selected within a cylindrical volume with a radius of 6.5 nm from the center of mass of the FGF2 oligomer.

Membrane curvatures were calculated with the MDAnalysis kit MembraneCurvature following the Tutorial. Curvatures were calculated for the last microsecond of each simulation.

# 3 Results

## 3.1 FGF2 and PI(4,5)$P_2$ curvature preferences by *in silico* Molecular Dynamics simulations

With new insights from our collaborators and experiments in the Nickel lab, FGF2 was found to predominantly form tetramers, hexamers, and octamers (brightness analysis). It assembles into differently shaped oligomers on membranes, as shown by negative stain EM, atomic force microscopy, and cryo-ET, with dimerization occurring through C95 (111). This sparked my interest in the molecular details of FGF2 self-assembly, pore formation, and the structural architecture of the membrane-inserted oligomer. With Molecular Dynamics simulations, I canaddress several highly interesting questions on the nature of FGF2 oligomerization and pore formation on a single complex level. The first question is about the membrane-associated oligomerization process of FGF2. How does FGF2 oligomerization occur, is there a specific oligomerization interface between cysteine-bridged FGF2 dimers? Do FGF2 monomers associate with FGF2 dimers to form stable, potential pore-forming complexes? Then, I want to investigate the local lipid environment around membrane-associated FGF2. Does FGF2 oligomerization cause membrane remodeling? Does FGF2 prefer or induce membrane curvature? What happens to PI(4,5)$P_2$ before, during or after pore formation?

### 3.1.1 Membrane curvature partitioning preferences

The current model of FGF2 secretion predicts transient formation of a toroidal pore. Toroidal pores are characterized by highly positive curvature at the pore rim, negative mean curvature in the center of the pore for small radii, no mean curvature here for larger pore radii. From a classical biochemical perspective, PI(4,5)$P_2$'s large and charged headgroup would be expected to disfavor negative curvature. On the contrary though, experiments and Molecular Dynamics simulations showed PI(4,5)$P_2$ in association with proteins in negatively curved membrane regions (198). Additionally, the PI(4,5)$P_2$ lipid is characterized by a slight negative spontaneous curvature, increased by multivalent ions like calcium (137). This negative curvature preference has usually been demonstrated in the context of membrane curvature-inducing proteins such as I-BAR domains, and with S-shaped membranes lacking extended flat regions without curvature (138). Therefore, I generated a coarse-grained membrane with both curved and flat regions, and simulated the diffusion of PI(4,5)$P_2$ and FGF2 on this membrane. As membrane, I used a simple POPC membrane with cholesterol and 5 % PI(4,5)$P_2$ and created a small patch of membrane. By using the BumPy (176) tool with the semicylindrical_plane, this membrane was multiplied by BumPy to create a semicylindrical shape to create a highly curved membrane, with a short flat region flanking the curvature. To combine positive, negative and no curvature of the semicylinders in one simulation, I created an inverse curvature of the same

membrane patch with identical settings and combined both curved membranes in one system, as illustrated in Figure 4.

As the curved membranes would just flatten out and loose the curvature, I used the in-built option of BumPy to position dummy particles during membrane creation. These dummy particles are mass-less, fixed artificial beads which only interact with the PO4 beads of phospholipids. The interaction between dummy particles and PO4 beads is repulsive, to keep the phospholipids in the created membrane shape. On each side of the membrane, a layer of dummy particles was added. Then, I embedded a FGF2 monomer to the flat, positively, or negatively curved region of the membrane to follow FGF2 curvature preference. FGF2 is embedded into the membrane with a single $PI(4,5)P_2$ lipid in the high-affinity binding-site composed of the residues K127, R128, and K133. The goal of this set of simulations is to determine whether FGF2 has an inherent preference for positive or negative membrane curvature, given that during translocation, it must either induce curvature or traverse the highly curved toroidal pore.

Production simulations were performed for at least 14 µs. In each of the respective systems, the FGF2 molecule quickly collected several additional $PI(4,5)P_2$ molecules. This dramatically reduced FGF2 diffusion on the membranes, and the FGF2 molecules did not leave their respective starting region in any of the simulations. The initial and final positions of the 3 starting simulations are shown in Figure 4. The FGF2 starting in the flat membrane did not pass the positively curved region to the left during the 38 µs simulation and remained in the negatively curved region. The FGF2 starting at the top of the positively curved region also did not leave this area during 37 µs. The FGF2 placed in the negatively curved invagination barely moved during the 14 µs simulation, whereas the lipids showed regular fast diffusion.

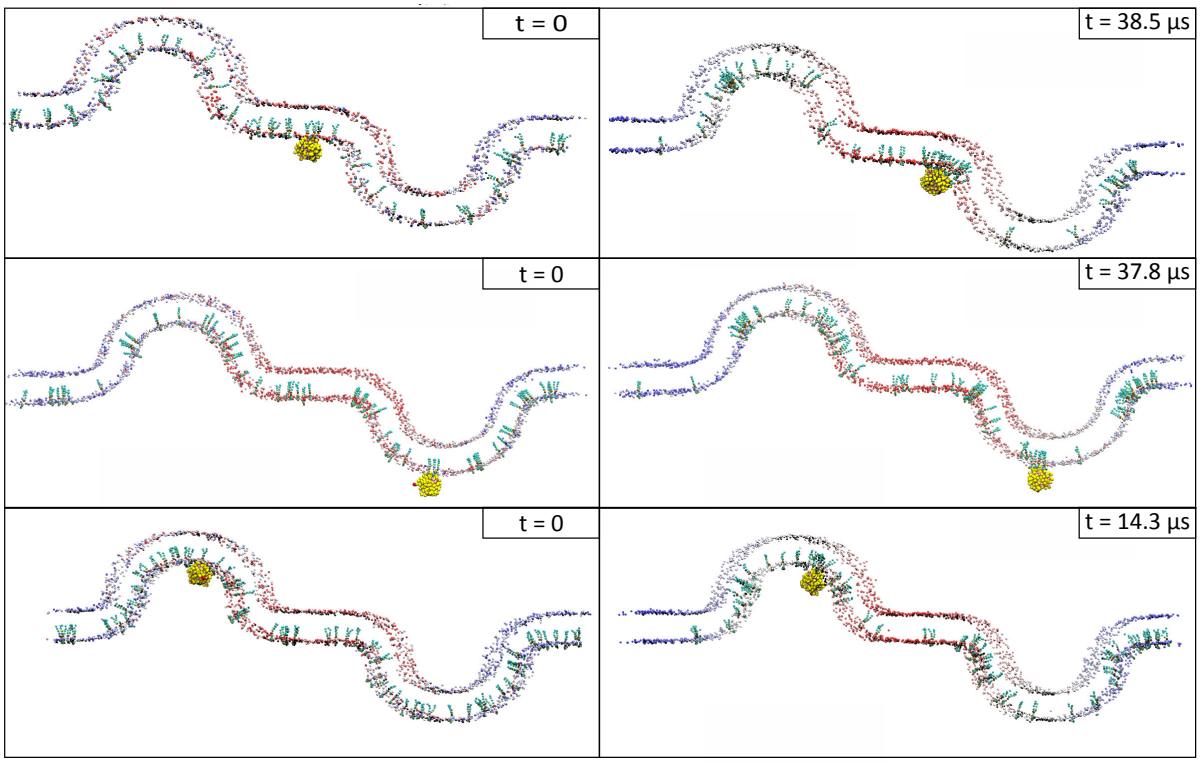


**Figure 4: FGF2 diffusion on large, curved membranes.** 3 systems were created with FGF2 embedded into the flat, positively, or negatively curved are of the membrane. FGF2 was embedded with a $PI(4,5)P_2$ molecule in the $PI(4,5)P_2$ high-affinity binding site of FGF2. In all simulations, FGF2 started to collect 4-5 additional $PI(4,5)P_2$ molecules, but diffusion slowed down and none of the FGF2 molecules left their respective starting curvature. VMD representation of the membrane: FGF2 is displayed as VdW representation, color: yellow. Phospholipid headgroups are shown to visualize the shape of the membrane. All individual $PI(4,5)P_2$ lipids are displayed to demonstrate positioning at the end of one repetition. QR codes link to videos of each simulation.

As most $PI(4,5)P_2$ lipids were not affected by FGF2 in these systems, $PI(4,5)P_2$ diffusion was considered independent. There, the evenly distributed $PI(4,5)P_2$ at the start of the production simulation was accumulated in the negatively curved areas of the membrane (Figure 5). Building on previous studies that examined sinusoidal membrane shapes with curvature-inducing proteins or flat membranes locally perturbed by such proteins (199), the inclusion of an extended flat region provided additional insight: in a POPC-cholesterol context, $PI(4,5)P_2$ exhibits a preference for negative curvature over no curvature.

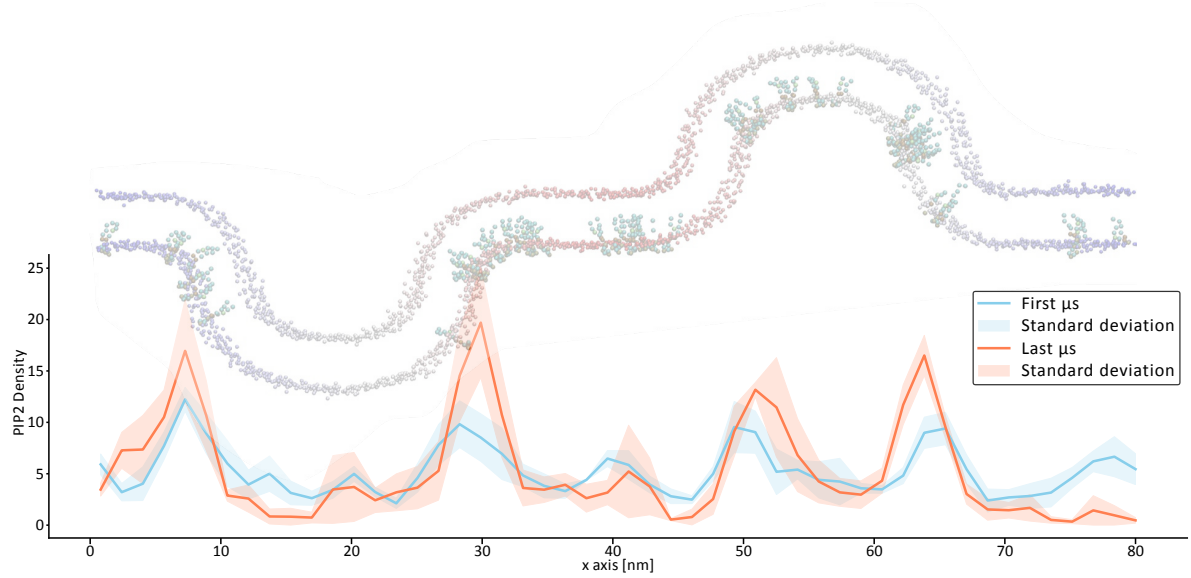


**Figure 5: PI(4,5)$P_2$ localization on curved membranes.** Production simulations of a POPC – cholesterol membrane with asymmetric PI(4,5)$P_2$ distribution in a curved context with areas of positive, negative, intermediate and no curvature. PI(4,5)$P_2$ was evenly distributed at the start of the simulation (blue line, first µs). During the production simulation, PI(4,5)$P_2$ accumulated in the negatively charged regions of the membrane and was abscent in the positively and non-curved regions. Data show the average of 3 independent simulations. In these simulations, a single FGF2 was placed on the membrane at either positive, negative are no curvature (not visualized in the example membrane). As most PI(4,5)$P_2$ molecules diffused independently from FGF2, the PI(4,5)$P_2$ localization in these simulations is unaffected by the present FGF2. VMD representation of the membrane: Phospholipid headgroups are shown to visualize the shape of the membrane. All individual PI(4,5)$P_2$ lipids are displayed to demonstrate positioning at the end of one repetition.

With this set of simulations, I could not observe FGF2 curvature preference due to the slow or potentially impaired diffusion of the FGF2 molecules on the curved membranes. In addition, using the dummy particles to maintain the predefined membrane profile, it was also not possible to see local changes in membrane curvature caused by the FGF2 monomer. Yet, the observed preference for PI(4,5)$P_2$ to cluster in the negatively curved regions sparked the thought for a new set of simulations, using a short-cut to gain more insights into the membrane-embedded state of FGF2 during translocation, described in the next section.

### 3.1.2 PI(4,5)$P_2$ clustering in toroidal pores depends on cholesterol and fatty acyl chain composition

From the problems of observing FGF2 diffusion on the previously described curved membranes, the idea arose to use a short-cut and observe FGF2 and PI(4,5)$P_2$ diffusion in a membrane with an already preformed toroidal pore as mimic for the membrane-inserted transition state during FGF2 translocation. As the pore opening on the actual membrane is dependent on so-far unknown properties and occurs in the range of tens or hundreds of milliseconds, the actual pore opening would be impractical to near impossible to simulate using only equilibrium simulations. However, it is a standard procedure to artificially open toroidal pores in MD simulations using flat-bottomed position restraints. Flat-bottomed position restraints applied a harmonic potential to specified particles outside a defined region,

guiding them back within its boundaries. Once inside, the particles no longer experienced the harmonic potential and were free to diffuse. Alternatively, the harmonic potential could be applied to particles within a defined region to push them outward. This method was used here on the PO4 beads of POPC lipids to form a toroidal pore with different diameters. Applying the potential on the bulk POPC lipids was enough to open toroidal pores despite PI(4,5)$P_2$ and cholesterol inside the membrane (Figure 6A). In this way, PI(4,5)$P_2$ and cholesterol molecules were never affected by the flat-bottomed position restraints and diffused unbiasedly. To study PI(4,5)$P_2$ localization in the presence of toroidal pores, I used Martini2.2 and created coarse-grained membranes with a simple lipid composition of POPC, varying concentrations of cholesterol, and 2.5 % PI(4,5)$P_2$, added only to one of the leaflets, creating PI(4,5)$P_2$ asymmetry. Figure 6B presents representative snapshots from a 10 µs simulation with 40 % cholesterol, a 2 nm pore, and 18:0-20:4 PI(4,5)$P_2$. These images show the observed PI(4,5)$P_2$ clustering (upper membrane bulk PO4 beads not shown for visualization). Initially, only 3 to 4 PI(4,5)$P_2$ molecules localize within the pore during the first microsecond, but their numbers increase over the course of the simulation until almost all PI(4,5)$P_2$ molecules of the membrane reside within the pore region.

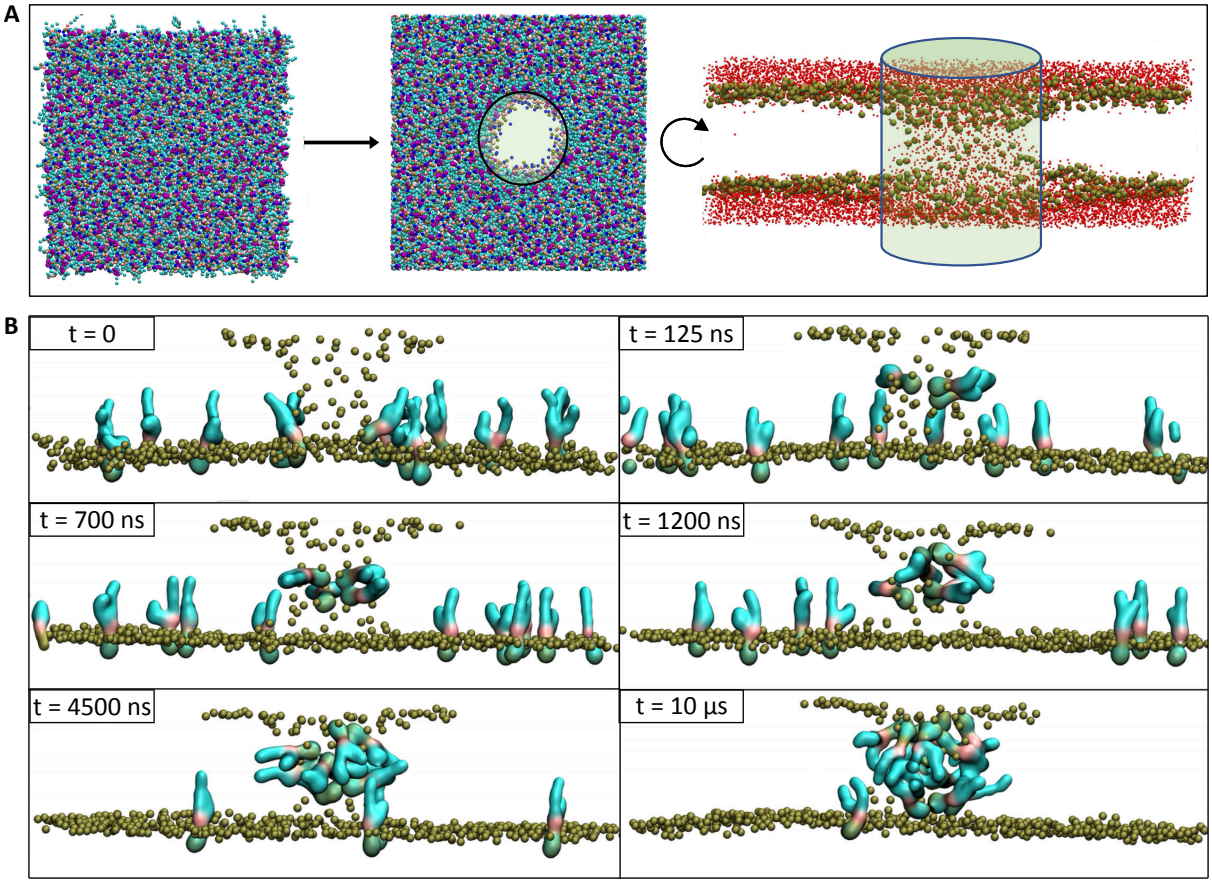


**Figure 6: Preformed toroidal pores to study PI(4,5)$P_2$ and FGF2 diffusion. A)** A flat-bottomed potential acts on the PO4 beads of the POPC bulk lipid to open a toroidal pore (green cylinder). The top and side view of the toroidal pore is on the right. The side view shows the PO4 beads of phospholipids (orange) and water beads (red) to demonstrate the water-filled pore. **B)** Snapshots of 18:0-20:4 PI(4,5)$P_2$ clustering around a 2 nm toroidal pore in an asymmetric POPC membrane with 40 % cholesterol and 2.5 % PI(4,5)$P_2$. PO4 beads: orange beads. PI(4,5)$P_2$: Quicksurf drawing method in Cyan. The upper part of the bulk membrane is not shown for visualization.

As it is known that cholesterol enhances PI(4,5)$P_2$-dependent binding of FGF2 to membranes *in vitro* (174), I used 0, 20, and 40 % cholesterol with a pore size of 2 nm, mimicking an initial state of pore opening. In Figure 7A, 2D histograms of PI(4,5)$P_2$ headgroup localization over the course of the entire 10 µs production simulations are shown. From left to right, the cholesterol concentration was increased, leading to a higher signal of PI(4,5)$P_2$ around the pore area, hence clustering. Upon expanding the pore sizes from 2 to 4 and 6 nm in diameter, mimicking pore expansion, PI(4,5)$P_2$ did not cluster anymore at the 4 and 6 nm diameter pores (Figure 7B). Here, I used the membrane with 40 % cholesterol, as it showed the most substantial clustering. Figure 7C showed a visualization of a 6 nm toroidal pore in a 10 % PI(4,5)$P_2$, 50 % POPC, 40 % cholesterol membrane. PI(4,5)$P_2$ in red was heavily clustered in the central plane of the toroidal pore, where both positive and negative curvature are present, orthogonal to the membrane and parallel to the membrane, respectively. Phospholipid headgroups are shown in yellow and water is displayed as blue beads to demonstrate the water-filled toroidal pore.

In Figure 7B, I maintained a constant PI(4,5)$P_2$ concentration while increasing the pore diameter, thereby expanding the pore area. To examine whether PI(4,5)$P_2$ clustering around larger pores depends on the number of available PI(4,5)$P_2$ lipids, I generated systems with 5, 7.5, 10, and 12.5% PI(4,5)$P_2$ and conducted production runs of at least 10 µs. Increasing the PI(4,5)$P_2$ concentration to 5% led to enhanced clustering around the 6 nm pore, with this effect intensifying as the PI(4,5)P2 concentration increased (Figure 7D). A similar trend was observed for 2 and 4 nm pores (data not shown).

Since the initial simulations focused on cholesterol concentration, pore size, or PI(4,5)$P_2$ concentration at a fixed cholesterol level, I conducted an additional set of simulations using POPC membranes with 6.25 % PI(4,5)$P_2$ and cholesterol concentrations ranging from 0 to 40 %, with a fix 4 nm pore. At this concentration, 18:0-20:4 PI(4,5)$P_2$ exerted weak clustering around the pore. Increasing cholesterol levels enhanced clustering as expected. At 30% and 40% cholesterol, PI(4,5)P2 clustering nearly or entirely displaced POPC molecules within the pore region, resulting in pore shrinkage or near-complete closure, respectively (Figure 7E). The data for this set of simulation is an average of three independent production runs of 10 µs each.

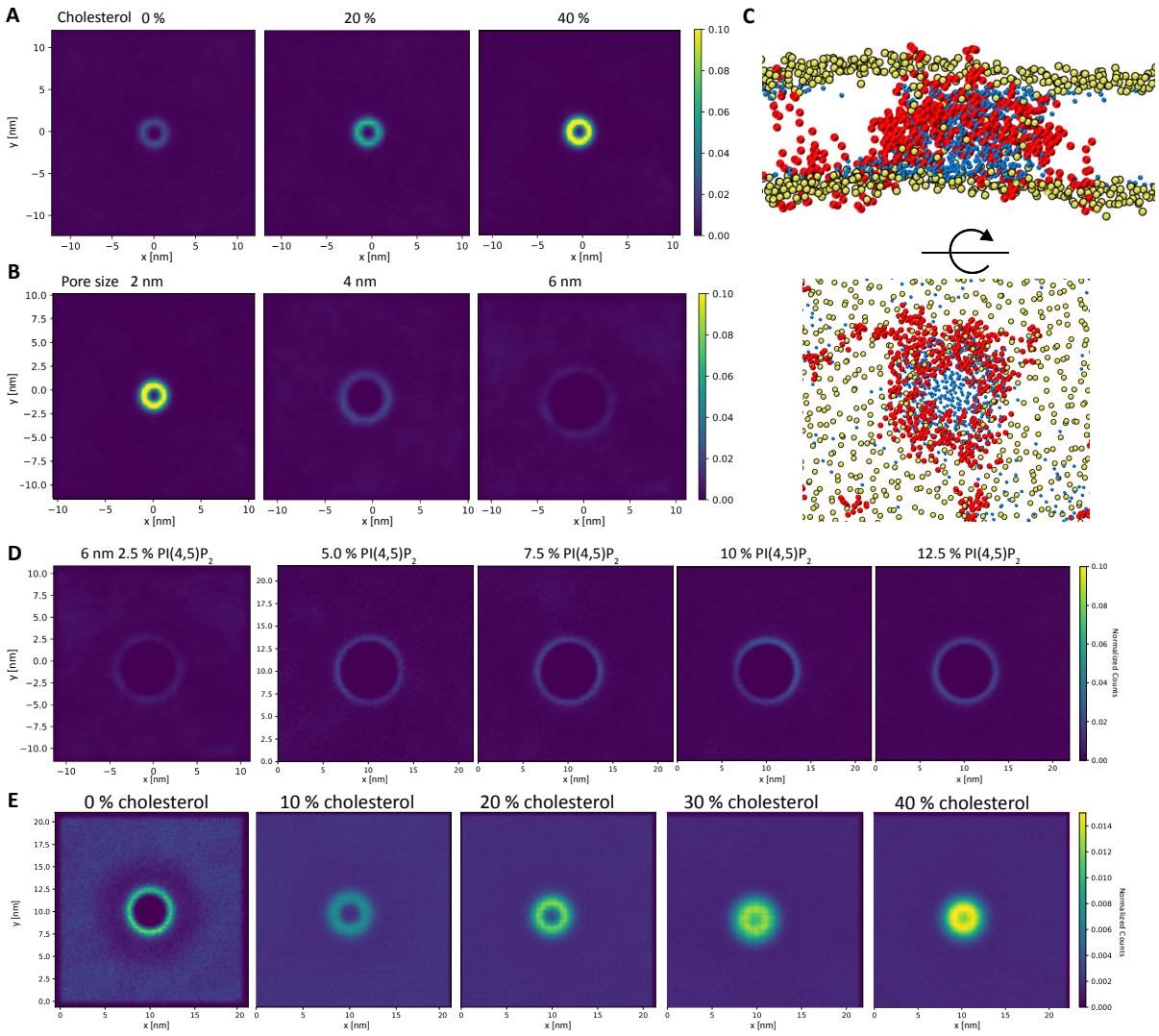


**Figure 7: PI(4,5)$P_2$ can cluster around preformed toroidal pores in a cholesterol, fatty acyl chain, and concentration-dependant manner. A)** 2D-histograms of PI(4,5)$P_2$-headgroup localization. 14 PI(4,5)$P_2$ molecules are able to cluster around a 2 nm toroidal pore upon increasing cholesterol concentration in the membrane. Lipid composition: POPC, 2.5 % PI(4,5)$P_2$ in one leaflet, cholesterol variable. **B)** 2D-histograms of PI(4,5)$P_2$-headgroup localization. Upon expanding the pore size from 2 to 4 and 6 nm, PI(4,5)$P_2$ did cluster less in the 40 % cholesterol background. The leftmost image is the same as the rightmost in A. The PI(4,5)$P_2$ concentration was kept constant. Lipid composition: POPC, 2.5 % PI(4,5)$P_2$, 40 % cholesterol. **C)** Side (top) and top view on a 4 nm pore with 40 % cholesterol and 10 % PI(4,5)$P_2$ for visualization of a water-filled toroidal pore. Yellow beads: PO4 atoms of phospholipids. Red beads: naturally most abundant 18:0-20:4 PI(4,5)$P_2$. Blue beads: water beads inside the pore region. **D)** 2D-histograms of PI(4,5)$P_2$-headgroup localization. As less observed clustering upon increasing pore size could potentially be PI(4,5)$P_2$-concentration dependent, I investigated clustering for higher PI(4,5)$P_2$ concentrations in a 40 % cholesterol membrane at 6 nm pores. Here, increasing the PI(4,5)$P_2$ concentration resulted in more clustering in the toroidal pore region. Lipid composition: POPC, 40 % cholesterol, 2.5 to 12.5 % PI(4,5)$P_2$ in 2.5 % increments. Scales of the leftmost and other four histograms are identical. **E)** 2D-histograms of PI(4,5)$P_2$-headgroup localization. Cholesterol-dependent PI(4,5)$P_2$ clustering around 4 nm toroidal pores at 6.25 % PI(4,5)$P_2$ concentration (in one leaflet). Increasing the cholesterol concentration caused more PI(4,5)$P_2$ to cluster in the toroidal pore region. Upon reaching 30 and 40 % cholesterol at 6.25 % PI(4,5)$P_2$, PI(4,5)$P_2$ displaced almost all POPC molecules, causing the pore to shrink and even close during the 40 % cholesterol production simulation.

In a final set of simulations, I investigated the role of PI(4,5)$P_2$ acyl chain heterogeneity. The predominant acyl chain in natural brain extract is 18:0-20:4 PI(4,5)$P_2$. The aim was to determine whether variations in acyl chain compositions might influence PI(4,5)$P_2$ clustering behavior *in silico* in addition to the observed cholesterol dependency. To explore this, I used

the same membranes with a 4 nm pore, with cholesterol concentrations ranging from 0 to 40 %. I analyzed the diffusion behavior of 3 additional PI(4,5)$P_2$ types: 18:0-18:0, 18:1-18:1, and 18:1-18:0. Unlike polyunsaturated 18:0-20:4 PI(4,5)$P_2$, these lipids did not show complete clustering around the 4 nm pore at any of the investigated cholesterol concentrations tested (compared to Figure 7E). The results for this set of simulations are an average of three independent production runs lasting 10 µs each.

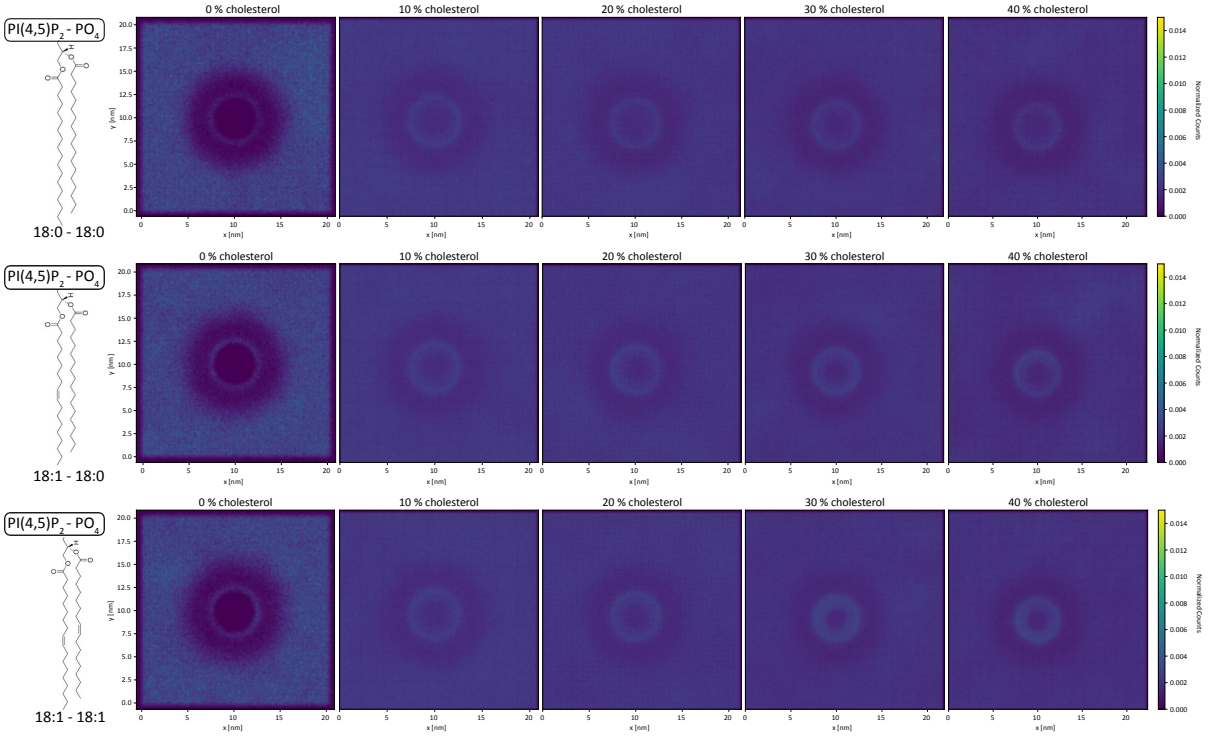


**Figure 8: 2-D histograms of acyl chain dependent PI(4,5)$P_2$ clustering around 4 nm toroidal pores. Top)** 2D histograms of membranes containing the fully saturated 18:0-18:0-like PI(4,5)$P_2$ in membranes from 0 to 40 % cholesterol. **Middle)** 2D histograms of membranes containing the partially unsaturated 18:1-18:0-like PI(4,5)$P_2$ in membranes from 0 to 40 % cholesterol. **Bottom)** 2D histograms of membranes containing the unsaturated 18:1-18:1-like PI(4,5)$P_2$ in membranes from 0 to 40 % cholesterol. **All)** No cluster formation was observed at any of the tested cholesterol concentrations. Positive control (Figure 7E): All membranes contain 6.25 % of the 18:0-20:4 PI(4,5)$P_2$ species with the labeled concentration of cholesterol in a POPC membrane.

These findings highlight the effect of cholesterol concentration, pore size, concentration and fatty acyl chain composition of PI(4,5)$P_2$ lipids on the clustering behavior in the presence of a preformed toroidal pore, with cholesterol and the highly unsaturated 18:0-20:4 acyl chain promoting PI(4,5)$P_2$ clustering within toroidal pores.

### 3.1.3 *In vitro* pore formation on GUVs with synthetic PI(4,5)$P_2$'s.

Building on the observed effects of different fatty acyl chains on PI(4,5)$P_2$ clustering, we investigated whether this influences FGF2 pore formation. To address this, my colleague Manpreet Kaur and I designed in vitro experiments, which she conducted, assessing FGF2-GFP pore formation on GUVs containing various synthetic PI(4,5)$P_2$ molecules. Based on synthetic PI(4,5)$P_2$ lipid availability, the acyl chains 16:0-16:0, 18:1-18:1, and 18:0-20:4 were used. FGF2-GFP was incubated with GUVs with the respective PI(4,5)$P_2$ lipids and pore formation was followed by confocal microscopy. Upon pore formation, a small fluorescent tracer molecule entered the GUV-lumen and the percentage of filled versus unfilled GUVs was counted (Figure 9A). In the control without PI(4,5)$P_2$, around 5 % of GUVs showed luminal signals, indicating unspecific leakage as FGF2-GFP could not bind to these GUVs. 16:0-16:0 PI(4,5)$P_2$ did cause slight increase to 15 %, but was statistically not significant compared to the control. For 18:1-18:1 PI(4,5)$P_2$, pore formation reached 35 %. And for 18:0-20:4, almost 50 % of GUVs showed pore formation (Figure 9B). Zeta potential was measured to ensure proper PI(4,5)$P_2$ incorporation into the GUV membranes. Zeta potential measurement is a technique for assessing the surface charge of suspended particles. PI(4,5)$P_2$ incorporation adds a lot of negative charge to the GUVs and should therefore lower the Zeta potential (more negative), and indeed this is what was observed for all three synthetic PI(4,5)$P_2$'s (Figure 9C). FGF2-GFP binding to the different GUV species was impaired, as FGF2-GFP bound significantly less to the 16:0-16:0 and 18:1-18:1 PI(4,5)$P_2$ GUVs (Figure 9D).

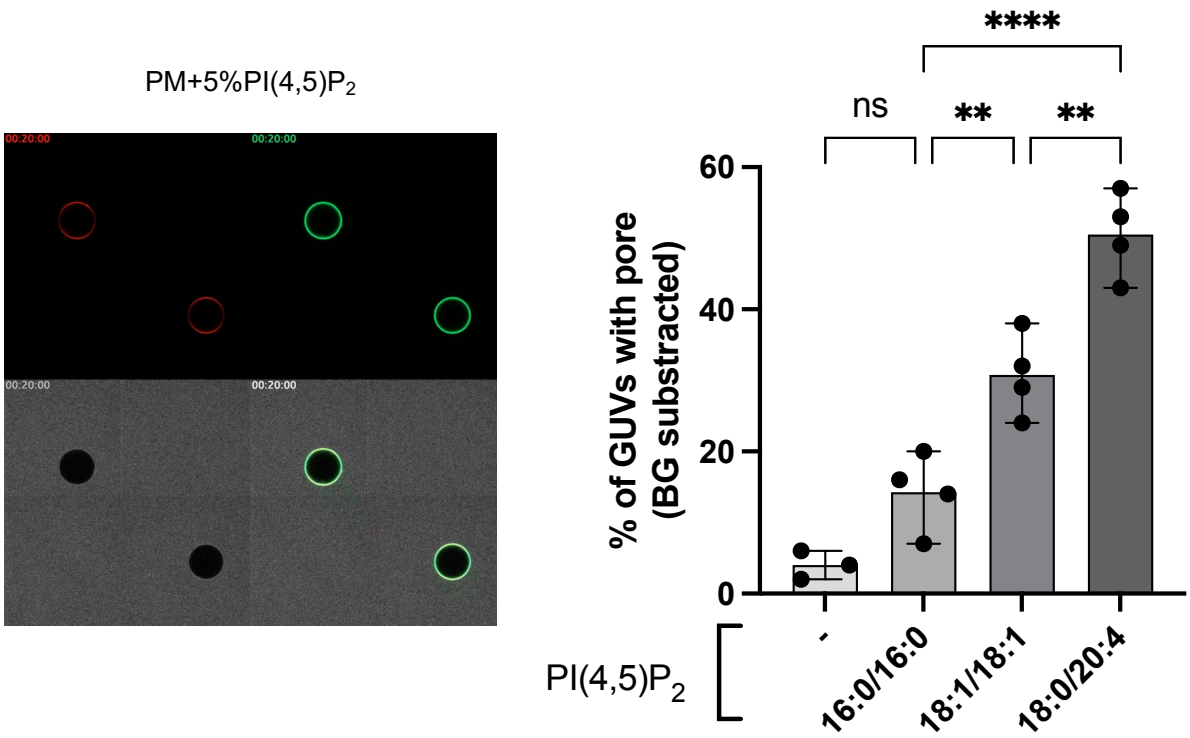


**Figure 9: Pore formation on GUVs by FGF2-GFP with different synthetic PI(4,5)$P_2$'s (data created by Manpreet Kaur).** Left: Exemplary images of GUVs in confocal fluorescence microscopy with plasma membrane-like lipid composition and 5 % brain-extract PI(4,5)$P_2$. The GUVs were created with Rhoadmine-PE, making the membrane visible in the red fluorescent channel (top left). The non-leaky GUVs before pore formation show no signal (black; bottom images). Upon pore formation, the fluorescent tracer enters the GUVs. Right: Percentage of pore formation upon FGF2-GFP binding to GUVs with the respective synthetic PI(4,5)$P_2$ lipid type. The experiments were designed together with Manpreet Kaur and carried out by Manpreet Kaur.

### 3.1.4 FGF2 organization inside preformed toroidal pores

By using the already preformed toroidal pore membranes and adding FGF2 to the membrane, I could study FGF2 organization inside toroidal pores. I used a scaled version of the Martini2.2 forcefield to reduce protein-protein interactions. Otherwise, contacts between FGF2 would be too strong and not separate anymore during the simulation, and I wanted the proteins to be able to dynamically diffuse across the membrane and inside the toroidal pore.

This set of simulation's starting point was 1 to 4 FGF2 molecules pre-bound to the membrane. The lipid composition of the membranes was 5 % PI(4,5)$P_2$, 55 % PC and 40 % cholesterol, and I tested 4 and 6 nm pores sizes, as a single FGF2 is already around 2.5 nm in diameter. For these simulations, the protein-protein interactions of the Martini2.2 forcefield was reduced to 80 %, as this simulation aimed to investigate dynamic interactions of monomeric proteins inside the toroidal pore. With the regular Martini2.2 forcefield, protein-protein interactions would be too strong and not flexible. Hence, in this set of experiments, I am only interested in the overall effect of FGF2-FGF2 interactions inside the toroidal pore, not their specific type and interface.

As a single FGF2 molecule entered the pore, it localized into the central region of the pore (height of the hydrophobic membrane core) and stayed there during the simulation (Figure 10A). With additional FGF2 monomers, FGF2 molecules experienced rearrangement upon protein-protein interaction with each other. Starting from a central arrangement within the membrane's central plane, interactions between FGF2 monomers inside the pore induced a structural rearrangement, resulting in parts of the protein protruding from the pore. (Figure 10B). When interactions between monomers ended, the proteins either exited the pore region or returned to the central pore. A similar rearrangement occurred with two or three FGF2 monomers in the pore region, leading to protein protrusions from the pore. Notably, this protruding arrangement exposed the PI(4,5)$P_2$-binding site (normally covered on flat membranes) to the surrounding solvent (Figure 10B). This could potentially suggest how membrane-proximal heparan sulfate chains can extract FGF2 since K133 of the PI(4,5)P2-binding site is part of the mutually exclusive binding site for heparan sulfates.

The arrangement of FGF2 monomers within the toroidal pore, including protrusion of protein surfaces from the membrane and the exposure of the PI(4,5)$P_2$-binding site, as part of the mutually exclusive heparin-binding site, to the surrounding solvent, provided insight into the dynamic interactions of FGF2 in the confined area of a toroidal pore and potentially help in understanding the 3-dimensional architecture upon membrane insertion of FGF2 oligomers. Before FGF2 can insert into the membrane, FGF2 must undergo essential oligomerization. This process presumably takes place on flat membranes and results in all necessary conditions for pore formation on PI(4,5)$P_2$-containing membranes. Understanding of these conditions is essential to uncover this most critical step in FGF2 unconventional secretion.

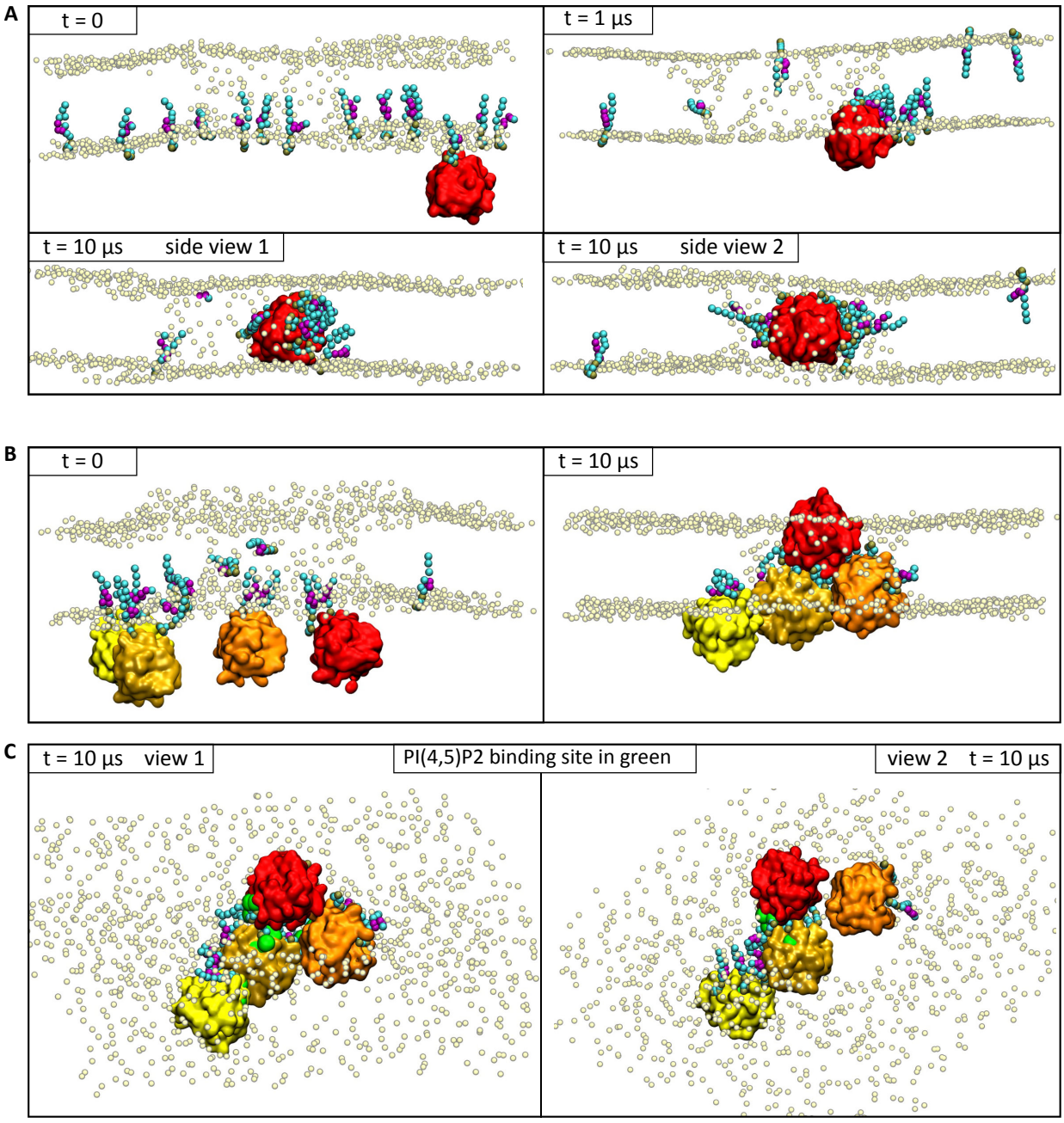


**Figure 10: 3-dimensional architecture of FGF2 inside stable, preformed toroidal pores.** Pre-bound, monomeric FGF2s were added to a POPC, 40 % cholesterol, 5 % 18:0-20:4 PI(4,5)$P_2$ membrane with a preformed toroidal pore of 6 nm. To prevent proteins from keeping stuck to each other and allow dynamic remodeling, the protein-protein interaction strength of the Martini2.2 forcefield was reduced to 80 %. **A)** A single FGF2 monomer in a 6 nm-sized pore. The FGF2 monomer moved in the center plane of the toroidal pore and collected 9 PI(4,5)$P_2$ molecules. **B)** Upon interacting in the pore region, FGF2 monomers shifted out of the central plane, resulting in both proteins protruding from the membrane. **C)** Two views from above of the image in **B** at t = 10 µs. PI(4,5)$P_2$ binding sites are highlighted in green. PI(4,5)$P_2$ binding sites are accessible by the surrounding solvent. Red, yellow, gold, orange: individual FGF2 monomers. Turquoise color: PI(4,5)$P_2$. Pale yellow beads: $PO_4$ headgroup bead of phospholipids. Green: PI(4,5)P2-binding site.

## 3.2 FGF2 self-assembly membrane surface

### 3.2.1 Oligomerization interface: FGF2 monomers on a flat membrane

Having gained insight into the three-dimensional architecture within preformed toroidal pores, I next aimed to address the preceding steps, specifically, the process of FGF2 oligomerization that occurs before pore formation and membrane insertion. It is known, that FGF2 oligomerization requires disulfide bridge formation and that C95 is the important surface cysteine necessary for oligomerization. Residues for stabilizing this C95-C95 interface have been discovered by *in silico* analysis, E86-K118 and E99-K85. However, no experimental evidence has yet identified the residues involved in potential additional interfaces contributing to oligomerization. To investigate these interactions, I generated an all-atoms system with 2 FGF2 monomers bound on a small membrane, with no additional $PI(4,5)P_2$ molecules, facing each other with the respective C95 residues. Then, I rotated one of the FGF2 monomers by 360° in 1° increments, keeping the shortest distance between both monomers at 0.8 nm (Figure 11A). For each of the 360 independent initial configurations, I ran a 500 ns MD simulation. The resulting trajectories were then used to train a machine learning algorithm, which we employed to cluster all possible dimerization interfaces observed during the simulations. Plotting the respective distances between C77-C77 and C95-C95 revealed that only C95-C95 was ever in close proximity below 1 nm required for disulfide bridge formation (Figure 11B). Dimensionality reduction and clustering with a machine learning Bayesian Gaussian mixture model (GMM) performed by my collaborator Dr. Shreyas Kaptan, University of Helsinki, group of Prof. Ilpo Vattulainen, revealed eight clusters (Figure 11C, D). The largest populated cluster showed that the C95-C95 distances are closer than 1 nm, with a network of salt-bridges stabilizing this arrangement. Residues E66, K85, E86, D98 and K118 were identified here, with the latter four having been previously observed in simulations of two FGF2 molecules in water (113).

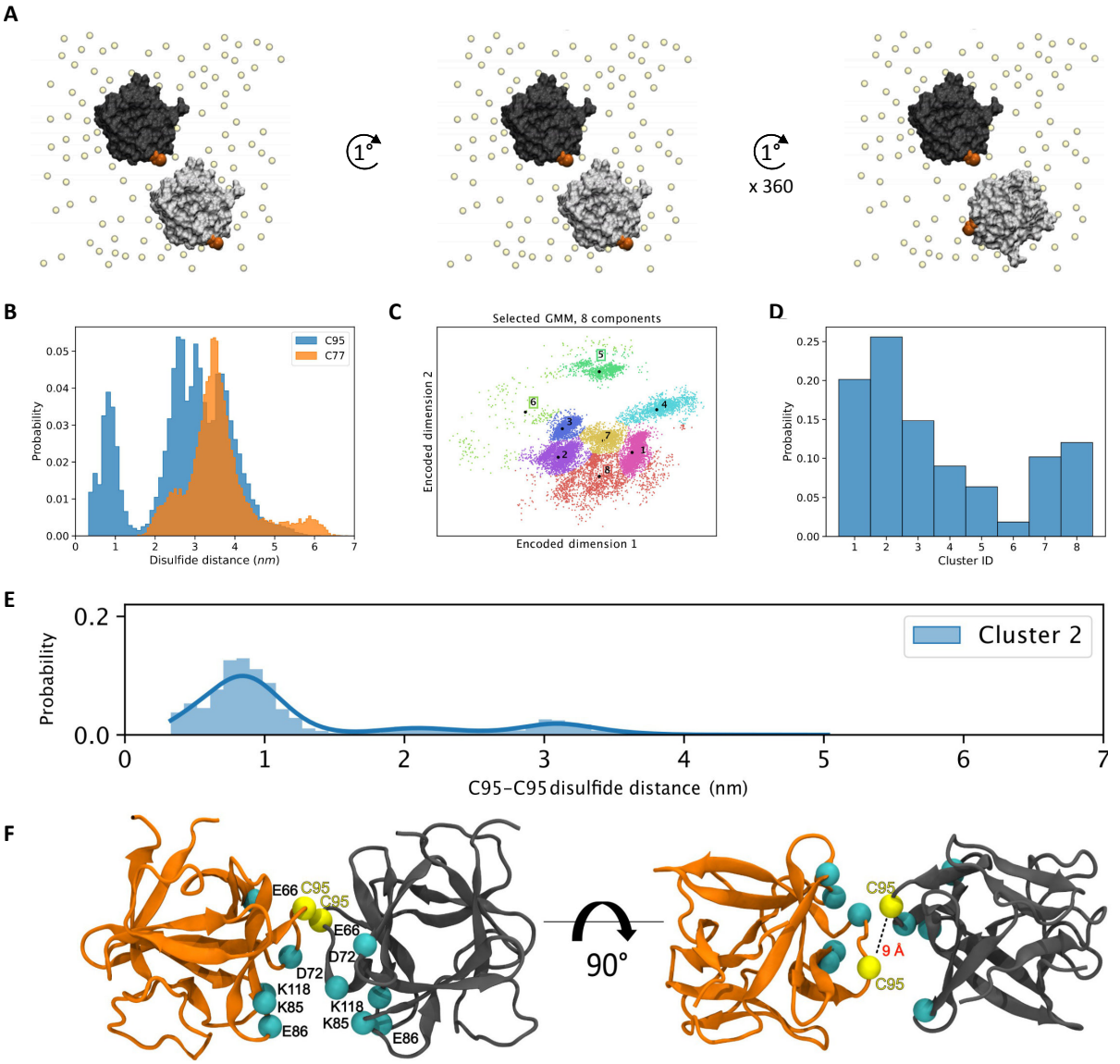


**Figure 11: FGF2-FGF2 interactions of membrane-bound FGF2 monomers. A)** Simulation setup. Two FGF2 monomers were pre-bound to the membrane with PI(4,5)$P_2$ in the respective binding pockets, facing each other with their C95 residues. One of the monomers was then rotated by 360 ° in 1 ° increments. **B)** Histogram of C95-C95 and C77-C77 distances during all 360 simulations. **C)** 2-dimensional representation of machine learning Bayesian Gaussian mixture model clustering with eight main clusters revealed. **D)** Population distribution of the eight clusters. **E)** C95-C95 distances of the cluster 2, showing the largest population of the analysis. C95-C95 distances were below 1 nm, required for disulfide bridge formation. **F)** Representation of cluster 2 centroid structure. C95-C95 were within 9 Å. This configuration was stabilized by electrostatic interactions involving residues E66, D72, K85, E86, D98, and K118. **B** to **F** adapted from Lolicato *et* al. (111).

### 3.2.2 FGF2 self-assembly into oligomers on PI(4,5)$P_2$-containing membranes

With additional interaction sites besides the C95 interface identified, I was curious to simulate FGF2 self-assembly into oligomers in all-atoms resolution. As previously, FGF2s were added with a PI(4,5)$P_2$ lipid inside the PI(4,5)$P_2$-binding site already bound to the membrane. As we know from experimental data, the average oligomeric size of pore-forming FGF2(-GFP) is 6 to 8 (111). Hence, I added a total of 6 FGF2 to a 25 nm x 25 nm patch of membrane composed of 55 % POPC, 40 % cholesterol and 5 % PI(4,5)$P_2$ added to the FGF2-leaflet. Here, I had

included an assumption based on experimental data from the lab, specifically that FGF2 reaches the membrane in an already dimerized state via a C95-C95 disulfide bridge. In one system, I added 2 FGF2 dimers and 2 FGF2 monomers (total of 6), and created 30 systems with different rotations of proteins. Similarly, I embedded 3 FGF2 dimers in the membrane and generated another 30 systems with different rotations (Figure 12). The systems total size was around 500,000 atoms and they were simulated for 5 µs. The 30 simulations with two dimers and two monomers did form a well-defined structural assembly involving all proteins (see appendix FigureS 1). On the other hand, simulations of 3 dimers showed structures with 2 to 3 dimers forming an open U- or V-shaped structures with 3 and 2 dimers, respectively (Figure 12B 1 & 2). Starting from the V-shaped 2-dimers configuration, we generated new simulations by varying the position of the third dimer. This approach aimed to increase the likelihood of interactions between the V-shaped dimers and the additional dimer, ultimately leading to gap closure and forming a hexameric ring. (Figure 12C).

The hexameric FGF2 ring was subsequently embedded in a complex, asymmetric plasma membrane-like lipid composition containing 5% $PI(4,5)P_2$ (Table 1,adapted from (51)), to assess the stability of the observed ring-like structure. elevated $PI(4,5)P_2$ concentration to ensured presence of a pool of $PI(4,5)P_2$ lipids in the bulk membrane, as FGF2 monomers typically gather 4-5 $PI(4,5)P_2$ lipids. Atomic force microscopy (AFM) data (unpublished), showed FGF2-GFP forming different closed-shaped oligomers with a visible hole in the center on flat supported lipid bilayers. Comparing sizes, the FGF2-GFP particles were around 30 nm in diameter and 3 nm in height in the AFM micrographs. My *in silico* FGF2 hexamer is around 10 nm in diameter and about 2.5 nm in height. With GFP being around 2.4 nm in diameter and 4.2 nm in length (200), subtracting these dimensions from the observed 30 nm in diameter, the untagged FGF2 oligomer *in vitro* should also be in the range of 10 nm in diameter. These experimental observations provide strong evidence that this ring-shaped FGF2 trimer of dimers was indeed very likely to represent a physiologically relevant form of FGF2 oligomerization during membrane association, oligomerization and pore formation.

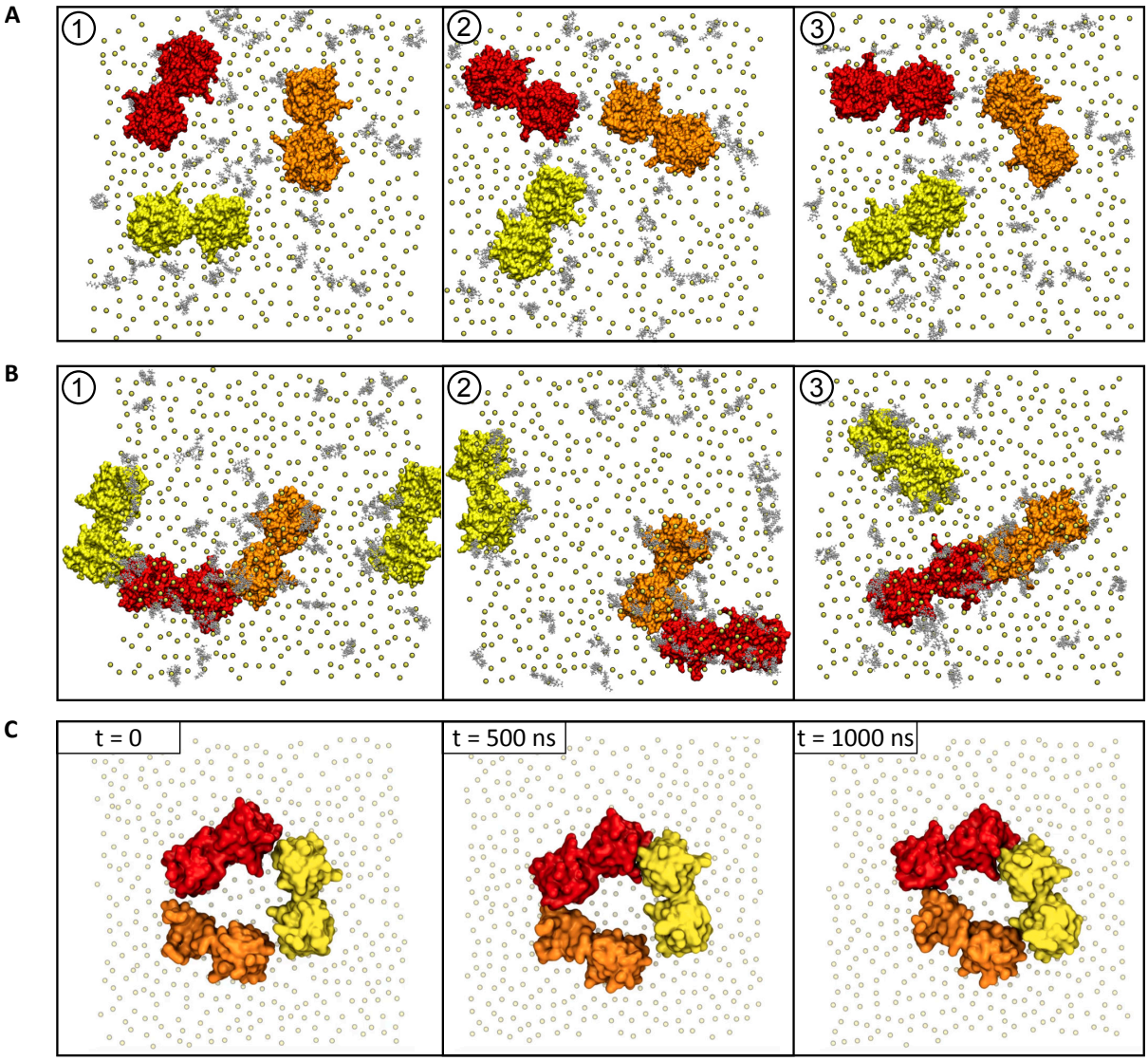


**Figure 12: FGF2 dimer self-assembly on flat membranes A)** Surface representations of 3 FGF2 dimers in all-atoms resolution. FGF2 dimers are covalently connected via C95-C95 disulfide bridge. Each dimer is colored differently. The membrane is represented by pale yellow beads (P atom of phospholipid headgroup), and PI(4,5)$P_2$ molecules are shown in grey (bulk lipid) and turquoise (PI(4,5)$P_2$ inside binding pocket). **B)** Exemplary gallery of found configurations. In 1, an open "U"-shaped hexamer formed with space for a fourth dimer closing the ring. In 2, two dimers form a "V"-like configuration, with space for a third dimer closing the gap to form a hexamer. In 3, linear configuration of two dimers. **C)** Assembly into ring-shaped FGF2 hexamer. The orange dimer was placed near the opening of the "V"-shaped two-dimer configuration. Proteins are represented in VMD Quicksurf style. PI(4,5)$P_2$ not shown here. The membrane has the same composition as in A and B.

Interestingly, although the ring-shaped structure was stable, the hexamer did not show complete symmetry and calculation of the interface surface areas revealed for 2 of the 3 simulations a broader distribution of interface surface areas (Figure 13). The wider distribution and three distinct surface area peaks indicate interface flexibility (Figure 13C). As the membrane contained 5 % PI(4,5)$P_2$, the FGF2s also collected additional PI(4,5)$P_2$ molecules besides the one inside the PI(4,5)$P_2$ binding pocket. Each FGF2 collected around 3 to 5 PI(4,5)$P_2$ within 4 Å. When looked at the hexamer from "below", through the membrane, the distribution of PI(4,5)$P_2$ was noticeable as some of the lipids were positioned directly between the dimers (Figure 13B).

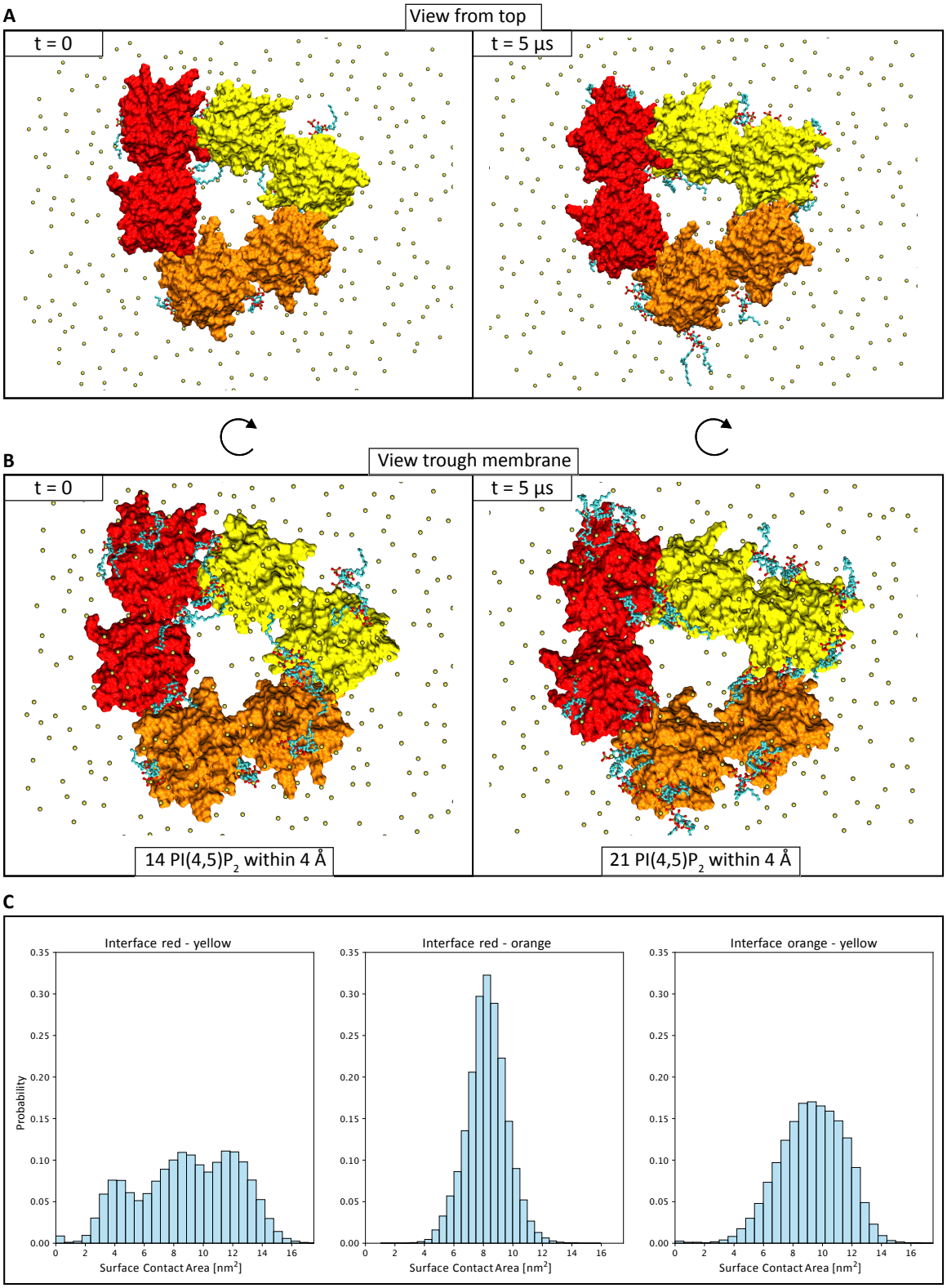


**Figure 13: Oligomerization interfaces in all-atoms hexamer simulations. A)** View from the "cytosol" on the FGF2 hexamer sitting on the flat membrane. Snapshots from t = 0 and t = 5 µs. Each C95-C95 disulfide-bridged monomer is shown in the same color. **B)** View through the membrane onto the membrane-facing side of the FGF2 hexamer with all $PI(4,5)P_2$ molecules shown within 4 Å of the hexamer. Snapshots from t = 0 and t = 5 µs. The FGF2 hexamer collected 7 additional $PI(4,5)P_2$ molecules during the simulation. $PI(4,5)P_2$ molecules in the dimer-dimer interface regions are noteworthy as they interact with residues from both dimers. **C)** Surface contact area plots reveal asymmetry of dimer-dimer interfaces and flexibility during the simulation due to the broadened distribution (red – yellow and orange – yellow interfaces). FGF2 dimers: Surface representation in VMD in red, orange and yellow. $PI(4,5)P_2$: CPK representation in cyan (carbon atoms), red (oxygen atoms), brown (phosphor atoms). Headgroup P atoms of phospholipids: pale yellow beads.

### 3.2.3 Membrane remodeling by FGF2 hexamer

With the hexameric structure of FGF2 in hand, I was able to address the important question of why FGF2 oligomerization ultimately leads to pore formation and membrane insertion. Because lipid diffusion is very slow in all-atoms simulations and the simulations were very large, reaching full equilibrium was not feasible. Therefore, I used a multi-scale approach and coarse-grained the membrane and FGF2 hexamer using the Martini2.2 model. This allowed us to simulate the effects of the membrane-bounded hexameric FGF2 ring within an asymmetric, plasma membrane-like lipid composition.

Coarse-graining of the FGF2 hexamer was achieved by using the martinize2 script with an elastic network, keeping the hexamer in the configuration from the all-atoms simulations. The Martini2.2 forcefield's protein-protein interactions were not modified here, as the interface originated from atomistic simulations. Due to some limitations in accuracy of lipid descriptions in the Martini2.2 model, the number of different lipids was reduced to 12 compared to 16 in the all-atoms system, but relations of the different phospholipids were kept identical (Table 2, adapted from (51)).

To follow lipid partitioning in the presence of the membrane-bound FGF2 hexamer, I did not start the simulation in a fully mixed membrane. I embedded the FGF2 hexamer with pre-bound $PI(4,5)P_2$ in the $PI(4,5)P_2$-binding sites into a patch of PC lipids and cholesterol. This PC-cholesterol-patch was then embedded into the remaining randomly distributed lipids. The PC-embedded FGF2 hexamer was then simulated for at least 10 µs in 6 repetitions. Within the first hundreds of nanoseconds, the PC patch dissolved by diffusion of lipids (Figure 14A). As seen in all-atoms simulations, $PI(4,5)P_2$ started to accumulate below the FGF2 hexamer. On average, each FGF2 monomer collected around 4 to 5 $PI(4,5)P_2$ molecules (Figure 14B). Another notable observation was the emergence of strong negative curvature below the FGF2 hexamer (Figure 14C).

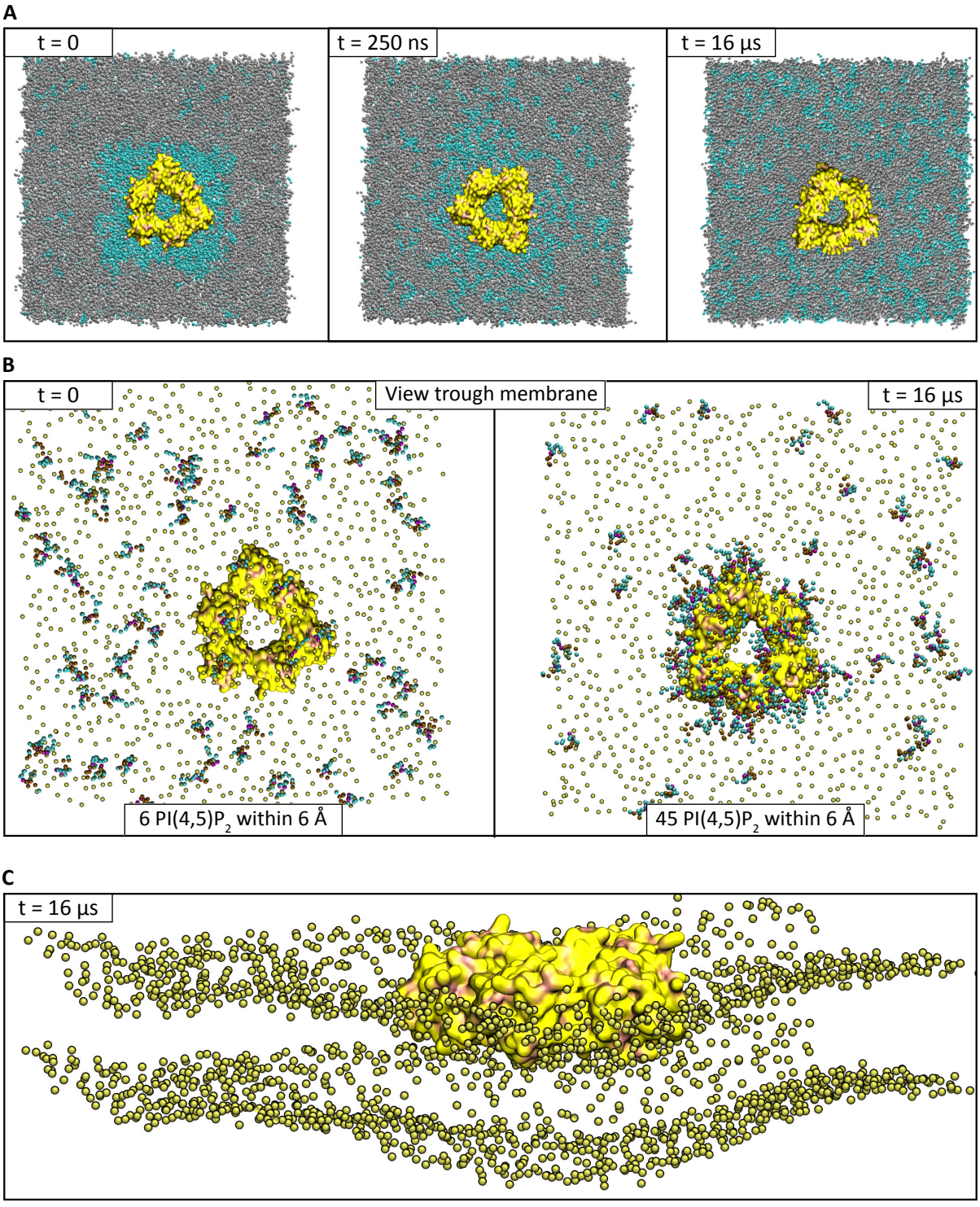


**Figure 14: Production simulation of coarse-grained FGF2 hexamer in asymmetric, plasma-membrane like membrane with 5 % PI(4,5)$P_2$. A)** Starting configuration with the FGF2 hexamer embedded into a patch of PC and cholesterol. Within a few hundred nanoseconds, PC lipids diffuse and distribute in the membrane. Cyan lipids: PC. Grey lipids: non-PC. **B)** PI(4,5)$P_2$ collection by the FGF2 hexamer. Simulations started with one PI(4,5)$P_2$ in the respective PI(4,5)$P_2$-binding site per FGF2 monomer. During production simulations, each FGF2 monomer collected 4-5 PI(4,5)$P_2$ lipids on average. The shown snapshot had even more PI(4,5)$P_2$ withtin 0.6 nm. **C)** Emergence of strong negative curvature below the FGF2 hexamer. Representations: Protein shown in yellow-pink surface representation. B and C: PO4 headgroups of phospholipids: pale yellow. B: PI(4,5)$P_2$ in van der Waals representation, cyan/purple/brown.

#### 3.2.3.1 Lipid partitioning

Given the substantial local accumulation of $PI(4,5)P_2$, I analyzed the local enrichment and depletion of all lipids beneath the FGF2 hexamer. As the FGF2 hexamer is around 10 nm in diameter, lipids for enrichment/depletion were selected within 13 nm of the center of geometry of the hexamer, roughly aligning with the center of the ring's inner cavity. Each membrane leaflet was analyzed separately, with around 230 lipids in the selected areas. I will call the leaflet with $PI(4,5)P_2$ and the FGF2 hexamer from here on *cytosolic leaflet*, and the other one the *extracellular leaflet*, as this system mimicked an FGF2 hexamer bound to the cytosolic leaflet of the plasma membrane. In Figure 15A, the enrichment/depletion is shown for the last microsecond. In the cytosolic leaflet (blue bars), $PI(4,5)P_2$ was heavily enriched by a factor of 3.5, translating into a concentration of 17.5 mol-% of total lipids. PC lipids were depleted by about 40 % down to 11.4 mol-%. PE was slightly increased by 1.4 %. Also, PS levels were depleted by 6.2 % down to 11 mol-%. Cholesterol and sphingomyelin concentrations were not affected. The total concentration of the non-bilayer lipids $PI(4,5)P_2$, PE and cholesterol added up to 76.6 %. In the extracellular leaflet, lipid enrichment and depletion were analyzed within the same region beneath the FGF2 hexamer. The observed variations ranged from 0 to 2%, indicating no direct coupling between the two leaflets.

Furthermore, I generated two sets of simulations: *(a)* with reduced $PI(4,5)P_2$ concentrations (2.5%, 2%, 1.6%, 1.2%, 0.8%, and 0.4%) and *(b)* with either two or a single FGF2 dimer. These systems were designed to assess whether the observed membrane remodeling (specifically lipid enrichment and curvature formation) was influenced by $PI(4,5)P_2$ accumulation beneath the protein and the number of FGF2 dimers on the membrane. Upon reducing the $PI(4,5)P_2$ concentration in the membrane, lipid enrichment/depletion values fluctuated but did not show a clear trend for cholesterol, PC, and PE in the cytosolic leaflet (Figure 15B). The apparent reduced enrichment in $PI(4,5)P_2$ at lower concentration is due to the limited number of $PI(4,5)P_2$ molecules in the membrane, as there are only 36, 30, 24, 18, 12, and 6 $PI(4,5)P_2$ molecules in the respective membranes (2.5, 2, 1.6, 1.2, 0.8, and 0.4 % $PI(4,5)P_2$). However, with lowering the concentration of $PI(4,5)P_2$ in the membrane, PS changed from depletion (- 6.27 %) to slight enrichment (+ 1.45 %). The membranes with only 1 or 2 dimers did not show consistent lipid enrichment/depletion for any of the lipids (FigureS 2).

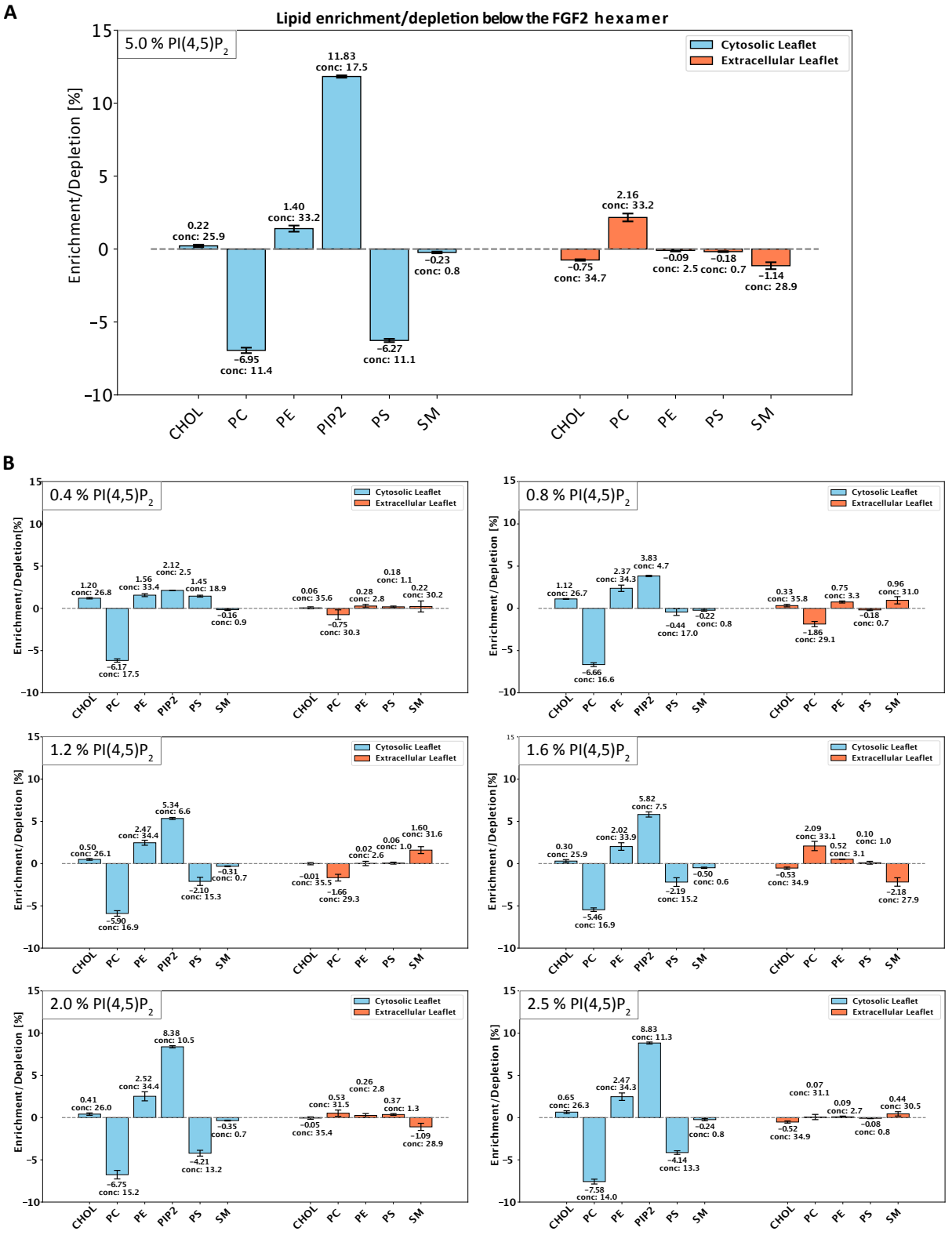


**Figure 15: Lipid enrichment/depletion below the FGF2 hexamer.** Lipid enrichment/depletion was calculated for the lipids within 13 nm of the center of mass of the FGF2 hexamer. The center of mass of the hexamer is located in the central cavity between the proteins. Leaflets were treated individually, yet the same area of membrane was analyzed. The analyzed area contained around 200 to 230 lipids in total (of around 1500 per leaflet). The enrichment/depletion is plotted for every lipid species in the (blue) cytosolic and (orange) extracellular leaflet. The "conc:" value gives the total concentartion of the respective lipid in mol-%, the other value is the enrichment/depletion in mol-% compared to the respective bulk concentration. **A)** Lipid enrichment/depletion for the plasma membrane-like lipid composition with 5 % $PI(4,5)P_2$. Values were calculated for the last microsecond. N = 6. **B)** Lipid enrichment/depletion for membranes with 0.4 %, 0.8 %, 1.2 %, 1.6 %, and 2.0 % $PI(4,5)P_2$.

#### 3.2.3.2 Membrane curvature

To compare membrane curvatures, the mean and Gaussian curvatures of the cytosolic leaflet were calculated using the MDAnalysis toolkit, MembraneCurvature.

The FGF2 hexamer system exhibited strong negative curvature formation when 4–5 PI(4,5)$P_2$ lipids per FGF2 monomer were spatially confined within a 10 nm diameter beneath the hexamer. This led to the formation of a pronounced groove, up to 35 Å deeper than the surrounding membrane regions. In contrast, in the absence of the hexamer, PI(4,5)$P_2$ lipids did not cluster, and membrane curvature remained within typical fluctuation ranges. The calculated surface depths varied between 51 and 58 Å (Figure 16). At PI(4,5)$P_2$ cocentrations below 1 %, membranes did not show distinct curvature formation. For PI(4,5)$P_2$ concentrations above 1 %, the z-positions of the leaflet surface showed a more dynamic range of 15 Å and more with distinct visible valeys in the positions of the FGF2 hexamer, indicating curvature formation, though less pronounced compared to 5 % PI(4,5)$P_2$-containing membranes. Notably, the concentrations from 0.4 % to 2.5 % corresponded to 6, 12, 18, 24, 30, and 36 PI(4,5)$P_2$ lipid molecules in the cytosolic leaflet. When only 6 or 12 PI(4,5)$P_2$ molecules were present (taking into account the 6 PI(4,5)$P_2$ bound to the FGF2 PI(4,5)$P_2$-binding site) no significant membrane curvature was observed (Figure 17A). With one or two FGF2 dimers, the spatially confined accumulation of PI(4,5)$P_2$ was less pronounced, yet still showed membrane curvature formation (Figure 17B). When all PE lipids (comprising approximately 30% of the cytosolic leaflet and known for their intrinsic negative curvature) were replaced with their PC counterparts, (bilayer lipid with no curvature preference) the membrane still exhibited curvature with little to no observable difference from the original system. (Figure 16A).

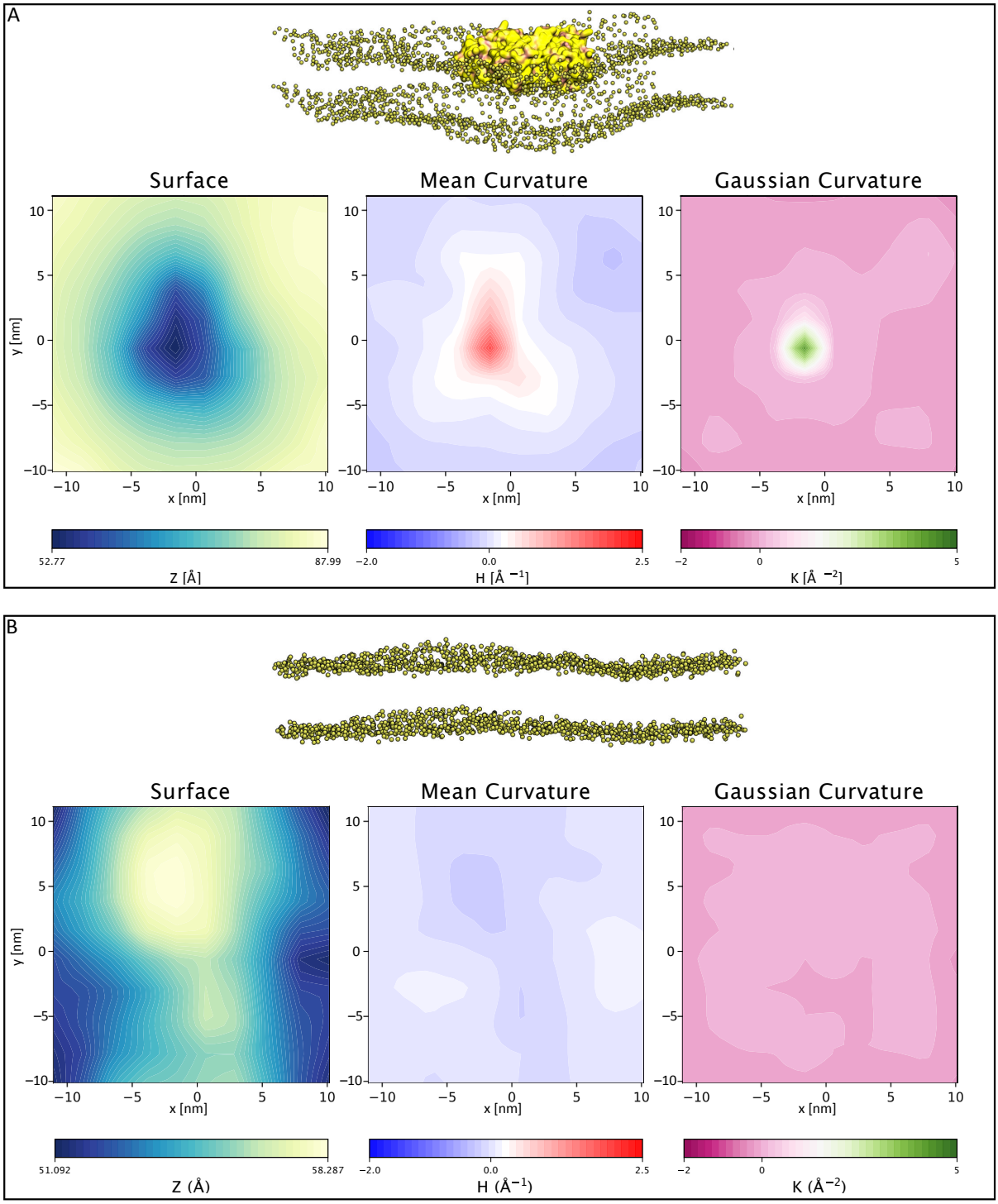


**Figure 16: Clustering of PI(4,5)$P_2$ by the FGF2 hexamer caused negative membrane bending.** VMD representation of systems with displayed PO4 headgroup beads of phospholipids and the FGF2 hexamer in Surface representation. Mean and gaussian curvatures were calculated by the MDAnalysis kit MembraneCurvature. Position of the leaflet surface, mean and gaussian curvature were calculated for each leaflet independently. Shown here are plot for the cytosolic leaflet with the embedded FGF2 hexamer. **A)** Strong formation of mean and gaussian curvature were observed in the plasma-membrane like membrane upon PI(4,5)$P_2$ clustering by the FGF2 hexamer. The Surface representation also shows a dent below the protein. **B)** The reference membrane without FGF2 hexamer did not show negative curvature formation, only typical curvature fluctuations. To compare the different systems, the colour scales for mean and gaussian curvature were set equal for all systems based on the highest values. The surface plots represent the z-positions of the headgroup beads for the cytosolic leaflet. Colour scales here were not set to be identical to appreciate the different dynamic ranges.

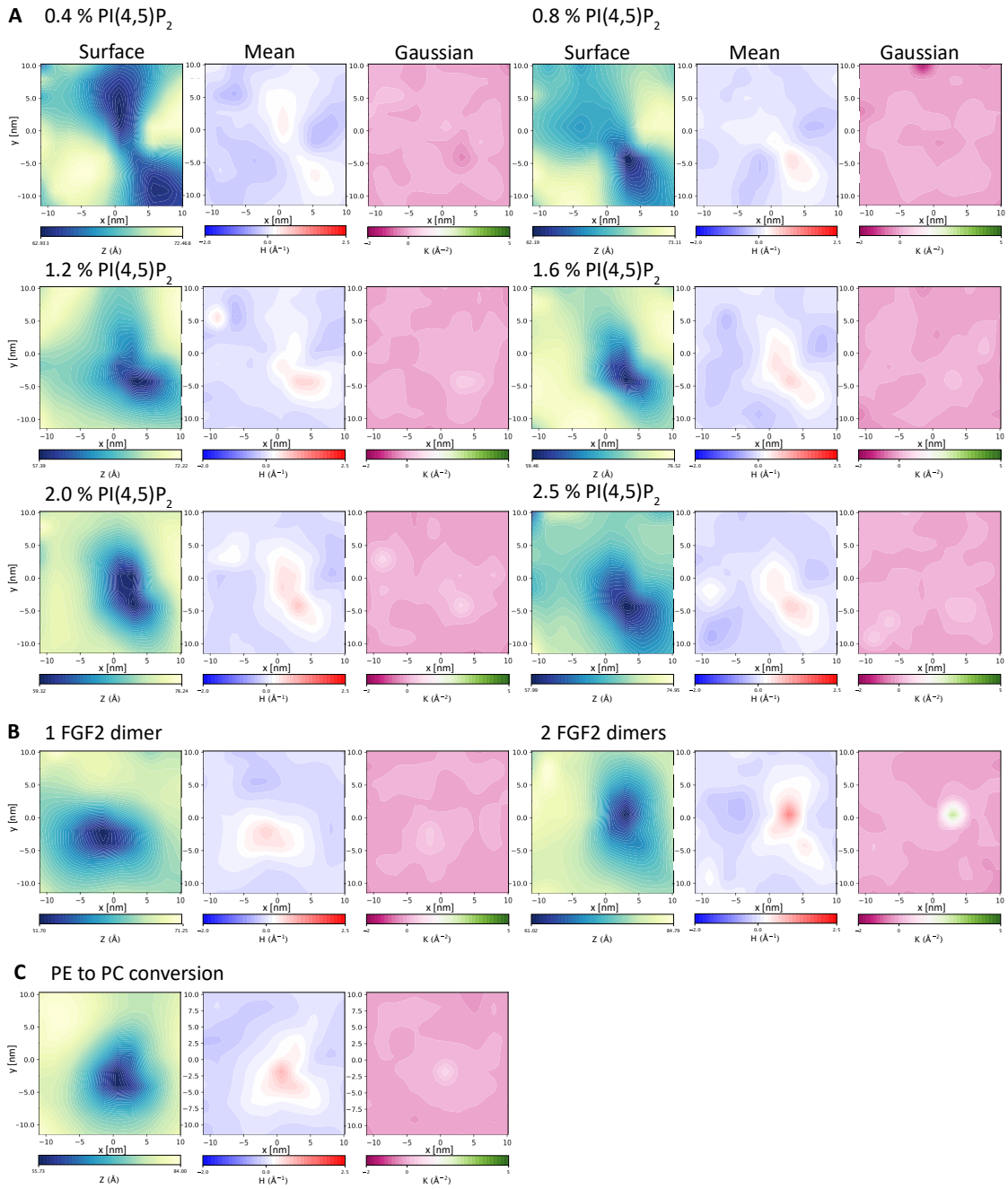


**Figure 17: Negative curvature formation is influenced by spatially confined accumulation of PI(4,5)$P_2$ by FGF2.** Mean and gaussian curvatures were calculated by the MDAnalysis kit MembraneCurvature. Position of the leaflet surface, mean and gaussian curvature were calculated for each leaflet independently. Shown here are plot for the cytosolic leaflet with the embedded FGF2 hexamer. All plots for mean and gaussian curvature have the same color range, respectively, for comparison. **A)** Curvatures for membranes with 0.4 %, 0.8 %, 1.2 %, 1.6 %, 2.0 %, and 2.5 %. Below 1 % PI(4,5)$P_2$ in the membrane, translating to 6 to 12 PI(4,5)$P_2$ lipid molecules in the membrane, mean and gaussian curvatures were less pronounced. Also the surface of the cytosolic leaflet was bent only +- 10 Å. **B)** Membranes with 5 % PI(4,5)$P_2$ and one or two FGF2 dimers. Negative curvature stronger for the system with two dimers. With two dimers, gaussian curvature was measured. **C)** All PE lipids were exchanged against their respective PC counterparts. Otherwise, 5 % PI(4,5)$P_2$ were present together with the FGF2 hexamer. The PE to PC exchange did not visibly effect membrane curvature formation. To compare the different systems, the colour scales for mean and gaussian curvature were set equal for all systems based on the highest values. The surface plots represent the z-positions of the headgroup beads for the cytosolic leaflet. Colour scales here were not set to be identical to appreciate the different dynamic ranges.

Given the pronounced membrane curvature observed, I analyzed the lipid tilt angle distributions across different systems. Lipid tilt angles were defined as the angle between the vector extending from the lipid acyl chain to the headgroup and the membrane normal. In the non-curved reference membrane with 5 % PI(4,5)$P_2$ and no embedded FGF2 hexamer, the lipid tilt angles were narrowly distribution with values below 5°. However, in the presence of FGF2, the lipid tilt angle distribution broadened and shifted towards higher tilt angles, up to 25°, with the majority of tilt angles above 5° (Figure 18B). In membranes containing a reduced PI(4,5)$P_2$ concentration (0.4% to 2.5%), the membrane with 0.4% PI(4,5)$P_2$ exhibited a peak around 3°, which was higher than the 5% PI(4,5)$P_2$ reference membrane but lower than the other systems, which showed a peak at 5°. Membranes with only 1 or 2 embedded FGF2 dimers still showed lipids to tilt up to 20°, with a peak at 5°, more closely resembling the tilt angle distribution in the hexamer-embedded membrane (Figure 18C). In contrast, the tilt angle distribution in the presence of 1 dimer membrane was below 5° as the reference membrane, correlating with the less pronounced mean curvature in Figure 17B

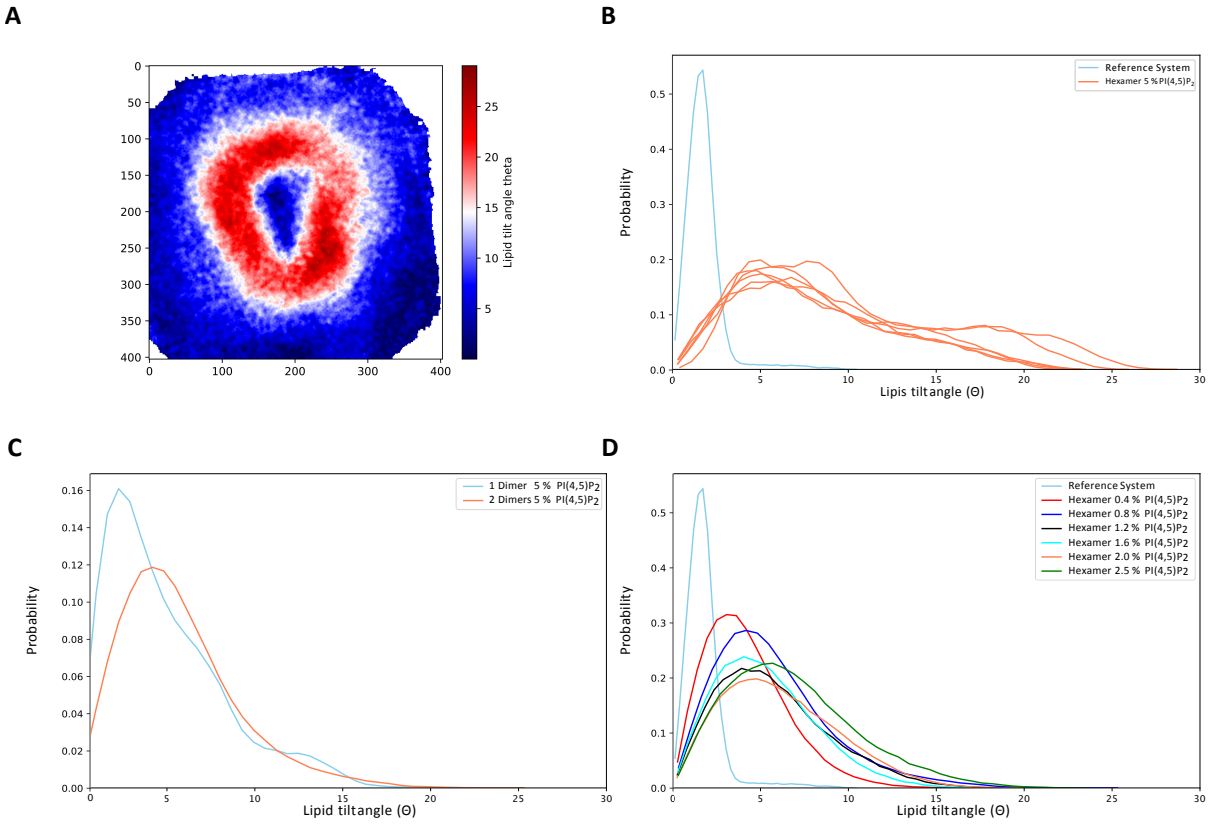


**Figure 18: Lipid tilt angle distribution.** Lipid titlt angles are defined by the vector from acyl chain tail to the headgroup in respect to the membrane normal. **A)** 2D-histogram of lipid tilt angle distribution in the cytosolic leaflet of the hexameric 5 % PI(4,5)$P_2$ membrane with embedded FGF2 hexamer. Tilt angles range from 0° up to 30° **B)** Line plot histogram of all repeats of the membrane with embedded FGF2 hexamer and 5 % PI(4,5)$P_2$ and the same membrane without FGF2. The curved membrane with the FGF2 hexamer showed a broadened distribution shifted to higher tilt angles. **C)** Lipid tilt angle distribution for the 5 % PI(4,5)$P_2$ membrane with only 1 or 2 dimers. **D)** Lipid tilt angle distribution for membranes with the FGF2 hexamer and 0.4 %, 0.8 %, 1.2 %, 1.6 %, 2.0 %, and 2.5 % PI(4,5)$P_2$ with the identical 5 % PI(4,5)$P_2$-containing reference membrane as in B.

These simulations demonstrate that FGF2 was able to locally sort lipids, especially PI(4,5)$P_2$, which then causes membrane deformations and negative membrane curvature.

## 3.3 Concluding remarks

The results from the multi-scale approach on FGF2 self-assembly and FGF2 hexamer-induced membrane remodeling revealed several important insights. Coarse-grained simulations with preformed toroidal pores demonstrated cholesterol and fatty acyl chain dependent PI(4,5)$P_2$ clustering inside toroidal pores. This clutering occurred in the hydrophobic core region of the lipid bilayer (relative position in z). The effect of the fatty acyl chain length and degree of saturation has so far never been tested on the ability of FGF2-GFP to translocate across liposomal membranes *in vitro*, but demonstrated the outstanding role of the 18:0-20:4 PI(4,5)$P_2$, which is especially abundnant in brain tissue (201-203).

Furthermore, the FGF2 hexamer is able to greatly alter the local lipid concentration by accumulation of 4-5 PI(4,5)$P_2$ molcules per monomer and depletion of PC and PS lipids. Thereby, a strong local concentration of negative charge from the PI(4,5)$P_2$ lipids and their tendency for spontaneous negative curvature formation cause a lot of stress to the membrane. Additionally, the lipid remodeling resulted in spatially-confined area beneath the FGF2 hexamer, which consists of approximately 70 % non-bilayer lipids, further promoting a high-energy state of the membrane. The spatially highly confined accumulation of non-bilayer lipids is known to cause membrane packing defects and could potentially be the main driving force for pore formation (204, 205). However, further investigations and biophysical experiments need to be performed based on these results to confirm this hypothesis.

# 4 Discussion

Since the discovery of the protein secretion machinery in the second half of the 20$^{th}$ century (5, 206), it has been extensively studied and components for the secretion of signal peptide-containig proteins from co- or post-translational translocation mechanisms at the rough ER through the Golgi network to the cell surface have been unveiled. Yet, proteins were discovered in the 1990s that did not follow this classical pathway and were able to escape cells without an N-terminal signal peptide, bypassing the classical ER/Golgi pathway (23). This type of secretion was soon termed “unconventional”, with four different types being identified up to this date. These types contain direct translocation across the plasma membrane, active secretion via ABC-transporters, vesicular intermediates, and a Golgi-bypass to the plasma membrane (type I to IV UPS) (2).

FGF2 has been one of the most intensively studied proteins following direct translocation across the plasma membrane (type I UPS) (107). The secretion of FGF2 in cells requires interaction with several factors at the plasma membrane (113). Briefly, FGF2 is recruited from the cytosol to the plasma membrane via the subCD3 domain of the sodium potassium ATPase (114). The interaction interface between the cellular subCD3 domain and FGF2 was pointed down to the residues D560 of α1 and K54 and K60 of FGF2. The latter two are in very close proximity to C77 on the surface of FGF2. Experiments showed FGF2 wild type and C95A substitutions are very capable of binding to the subCD3 domain, whereas FGF2 C77A showed impaired binding towards subCD3, pointing towards a potential involvement of C77 in the interaction interface. Cystein double mutant C77/95A showed a more severly impaired interaction with subCD3, indicating that FGF2 dimerization via C95 might play a role in subCD3 interaction and could already occur at the subCD3 domain before handing over FGF2 to $PI(4,5)P_2$ at the plasma membrane. At the plasma membrane, FGF2 is able to form oligomers in a $PI(4,5)P_2$-dependent manner (32, 112). This oligomerization then causes dynamic membrane disturbances, pore formation and membrane insertion. Lastly, the secretion is completed by membrane-proximal heparan sulfate chains of HSPGs (glypican 1), outcompeting $PI(4,5)P_2$ from the mutual exclusive binding site (34, 113). HSPGs keep FGF2 close to the membrane to act in paracrine or autocrine signaling via high-affinity FGF receptors (94).

A potential reason for this alternate route to the cellular surface could be explained by the FGF2 variants that had attached N-terminal signal peptides. These signal peptide-carrying FGF2s were successfully rerouted through the ER/Golgi to be secreted into the extracellular space. However, this FGF2 was not found at the cell surface and did not show mitogenic activity (207). This could be traced back to posttranslational modifications in the ER/Golgi pathway during conventional secretion. The UPS route could, therefore, indicate an evolutionary older mechanism than the conventional ER/Golgi pathway and/or be an alternate route for proteins avoiding post-translational modifications (208).

In the last years, FGF2 secretion could be imaged in living cells at a single event level using total internal reflection fluorescence microscopy (TIRF), following the process of recruitment, oligomerization and secretion at the plasma membrane (124). To differentiate cellular from extracellular signals, cells expressing FGF2-GFP were paired with a fluorescent anti-GFP nanobody applied to the extracellular space. By monitoring FGF2-GFP fluorescence, recruitment at the plasma membrane could be followed. Then, the translocation event was monitored with the anti-GFP nanobody fluorescence, revealing a very fast kinetic with an average time interval of only 200 ms between FGF2-GFP recruitment at the membrane and full translocation. To put this in cellular context, the fastest observed membrane crossing to date are protein passages through nuclear pore complexes, which take around 10 ms . On the other hand, the classical secretory pathway through ER and Golgi requires between 20 and 40 minutes for cargo to reach the extracellular space (209). Therefore, FGF2(-GFP) direct translocation across the plasma membrane belongs to the fastest processes for proteins crossing a membrane.

The process of FGF2 membrane translocation was also successfully reconstituted *in vitro*, utilizing only FGF2 and PI(4,5)$P_2$-containing, long-chain heparin-filled liposomes, strongly suggesting that the fundamental mechanisms of pore formation are inherent to the intrinsic properties of FGF2 and PI(4,5)$P_2$-containing membranes (113). It has furthermore been demonstrated, that FGF2 oligomerization and pore formation are dependent on PI(4,5)$P_2$ inside the membrane and cannot be reproduced with nickel nitrilotriacetic acid lipids (NTA), which do bind his-tagged FGF2 to the membrane, but do not promote pore formation (32). With luminal long-chain heparin, FGF2-GFP translocation could be followed in live confocal microscopy, with luminal fluorescence as indication of succesfull extraction of the FGF2-GFP from the membrane, which is stuck at the membrane without luminal long-chain heparin (113). With the *in vitro* system, it was also possible to determine the average oligomeric size of the FGF2-GFP fusion protein by employing fluorescence brightness analysis on single GUVs, with an average oligomeric size of 4 to 8 subunits. Here, C77A substitution did not influence oligomerization behavior compared to the reduced membrane recruitment in cells. Substituting C95 by alanine though significantly impaired FGF2 oligomerization, preventing dimerization. Together with impaired pore formation capabilites of only the C95 and C77/C95A substitutions, cross-linking mass spectrometry experiments, and atomistic Molecular Dynamics simulations and structure predictions, the C95-C95 disulfide bridge was identified as the interface for initial FGF2 dimerization, required for further oligomerization (111). Despite C77 not being directly involved in oligomerization, C77A substitution reduced FGF2 secretion efficiency by weakening the K54-K60-C77 interface between α1 subunit of Na,K-ATPase and FGF2, interfering with membrane recruitment of FGF2 (114).

However, compared to the cellular time interval of 200 ms, the translocation of FGF2-GFP on liposomes *in vitro* takes on average about 1 hour (unpublished data, untagged FGF2 55 min (32)). There a several factors that may contribute to this discrepancy. Cofactors as the Na,K-

ATPase and glypican-1 could increase efficient membrane recruitment by promoting correct C95-C95 disulfide bridge formation and offer a favorable lipid environment for fast membrane translocation by association with some sort of lipid nanodomain (precise lipid environment still under investigation). Since a membrane's properties and lipid organization are very closely linked to the exact lipid composition, asymmetry, membrane potential, tension, embedded and linkend proteins, and lateral lipid distribution, model liposomes will have different physical properties compared to plasma membranes. In addition, the *in vitro* system lacks a potential electron acceptor for the oxidation during disulfide bridge formation, slowing down the essential first step of in oligomerization. As these considerations are all possible sources of the observed kinetic differences, further research in these directions could provide valuable insights in fully elucidating the intricate mechanism of FGF2 membrane translocation at the molecular level.

With the principal machinery and a certain level of molecular detail of FGF2 translocation uncovered, big questions remained unclear. Why does FGF2 translocation require oligomerization. Why is FGF2 oligomerization $PI(4,5)P_2$ dependent and only occuring on the membrane? How does oligomerization lead to pore formation? What is the minimal (and maximal) required oligomeric unit for pore-formation? What is the architecture of the membrane-inserted FGF2 oligomer?

In this thesis, I adressed those questions using *multi-scale* Molecular Dynamics simulations.

## 4.1 *In silico* approach to understand FGF2 oligomerization and pore formation

Over the last decades, Molecular Dynamics simulations became a well-established method to gain invaluable insights into the molecular details of dynamics processes from material sciences to biological systems (152, 210). With unparalleled molecular detail and timescales, MD simulations became quite reliable in complementing experimental techniques and guiding experimentalists in designing experiments. Thereby, MD simulations greatly benefit from the exploding amount of available structural data, the emergence of powerful structure prediction tools like AlphaFold 2 and AlphaFold 3, and advances in computational power and their availability (211-214). The latter allows simulations to extend to much longer timescales and larger systems. This progress allows for investigations of increasingly complex systems, which were typically constrained by the computational power available. Since the first MD simulations in the 1970s, where systems were limited to picoseconds timescales and a few atoms, typical simulations nowadays easily reach microsecond timescales, already scratching the millisecond realm, and contain hundreds of thousands to millions of atoms.

It is already known that the translocation of FGF2 and FGF2-GFP and Halo fusion proteins across membranes *in vitro* and in cells depends on proper recruitment at the membrane via $PI(4,5)P_2$, the ability to oligomerize, and is influenced by the cholesterol concentration of the membrane (32, 111-113, 174). However, the molecular mechanism leading to pore formation

at the membrane remained inaccessible to experimental methods. Therefore, I used Molecular Dynamics simulations to shed light on the molecular details of pore formation in FGF2 translocation.

### 4.1.1 Cholesterol and fatty acyl chain-dependent clustering of PI(4,5)$P_2$ around toroidal pores

I used preformed toroidal pores in coarse-grained, asymmetric membranes using the Martini2.2 forcefield to address the fate of PI(4,5)$P_2$ during FGF2-induced pore formation and to observe how FGF2 (monomers) behave in the context of toroidal pores.

By using toroidal pores with diameters ranging from 2 nm, mimicking an initial pore opening state, to 6 nm, which is the potential size of the transient FGF2-oligomer induced pore based on the FGF-GFP oligomer size determined by atomic force microscopy (111), varying PI(4,5)$P_2$ and cholesterol concentrations, and different fatty acyl chains for the PI(4,5)$P_2$ lipids, I was able to identify a cholesterol, fatty acyl chain saturation, and PI(4,5)$P_2$ concentration dependent effect on PI(4,5)$P_2$ clustering inside toroidal pores (Figure 7 & Figure 8). With the naturally most abundant PI(4,5)$P_2$, the highly unsaturated, long-chain 18:0-20:4 PI(4,5)$P_2$, most substantial clustering was observed in a cholesterol-dependent manner. Weak to no clustering occurred in 0 % cholesterol membranes, whereas 40 % cholesterol led to clustering of almost all PI(4,5)$P_2$ molecules in the membrane. At 6.25 mol-% PI(4,5)$P_2$ and 40 % cholesterol, I observed full displacement of all POPC lipids by PI(4,5)$P_2$ in the toroidal pore area. This led to closure of the pores, as the flat-bottom position restraints used to open and maintain pore integrity only affected the POPC PO4 headgroup bead. From these findings, experiments were designed using synthetic PI(4,5)$P_2$ variants to test PI(4,5)$P_2$ pore formation in the established *in vitro* GUV pore formation assay. The experiment was designed with and performed by Manpreet Kaur. Pore formation of FGF2-GFP was observed with a fully saturated, shorter 16:0-16:0, a mono-unsaturated 18:1-18:1, and the most abundant 18:0-20:4 PI(4,5)$P_2$. And indeed, significant differences in pore formation were measured. Pore formation was most abundant in GUVs with 18:0-20:4 PI(4,5)$P_2$ with pore formation observed in 50 % of GUVs. This dropped to 30 % and 15 % for 18:1-18:1 and 16:0-16:0 PI(4,5)$P_2$, respectively (Figure 9). In conclusion, the 20:4 chain offers unique properties amongst the tested acyl chains with multiple double bonds, likely altering the properties of this specific PI(4,5)$P_2$ compared to less unsatured chains. The double bonds enable “kinks” in the tail region increasing flexibility and reducing interactions with cholesterol, which prefers fully saturated acyl chains (215). However, the precise molecular mechanism of acyl chain curvature preference for PI(4,5)$P_2$ needs further investigation.

### 4.1.2 FGF2 self-organization exposes PI(4,5)$P_2$-binding-site inside toroidal pores

With the toroidal pore system at hand, I embedded FGF2 monomers with PI(4,5)$P_2$ inside the PI(4,5)$P_2$ binding pocket into pore-containing membranes and followed FGF2 diffusion into the pore region. Upon interaction of at least two FGF2 monomers, the pore-resident FGF2s underwent spatial rearrangement. They left the central plane near the hydrophobic core of the membrane to positions closer to the pore rims, adopting a helical-like 3-dimensional architecture. This rearrangement resulted in FGF2s protruding from the membrane with their PI(4,5)P2-binding site exposed to the aqueous surroundings. These dynamics were consistent for all simulations with either two, three, or four FGF2 monomers for two different pore sizes. I used a rescaled Martini2.2 forcefield with reduced protein-protein interactions to prevent excessive aggregation of FGF2 monomers (177, 216). This allowed for the observed flexibility of FGF2 – FGF2 interaction. However, the observed interactions between FGF2 monomers did not necessarily represent the native interactions, as the Martini2.2 forcefield overestimates electrostatic interactions (165). Despite this limitation, the observed spatial arrangements provide valuable insights into the potential organization of FGF2 within the toroidal pore.

With the exposed PI(4,5)P2-binding site, membrane-proximal heparan sulfate chains have the potential to outcompete PI(4,5)$P_2$ at the mutually exclusive binding site and extract FGF2 from the pore region. Simulating heparin and heparan sulfates remains very challenging due to their structural complexity and conformational variability. Current force fields do not fully replicate the conformational ensemble observed in experimental data, such as NMR. However, recent advances are promising for correct predictions of (complex) sugars in the near future (217, 218). With improved prediction of heparin/heparan sulfate chains, FGF2 extraction from the toroidal pores could be simulated. This leaves only the pore formation step to be resolved before achieving a complete simulation of the entire FGF2 translocation process from membrane binding and self-assembly to pore formation and extraction.

### 4.1.3 FGF2 self-assembly in PI(4,5)$P_2$-containing membranes

The current hypothesis of the secretory pathway of FGF2 secretion from cells starts with membrane recruitment and dimerization at the α1 domain of Na,K-ATPase. This dimerization, which drives translocation, relies on the surface cysteine C95. Substituting C95 with alanine (C95A) significantly impaired FGF2 translocation from cells and prevented oligomer and pore formation in in vitro experiments using PI(4,5)$P_2$-containing liposomes (111). Pore formation then requires oligomerization, with an average of 4 to 8 monomers in active, pore-inducing complexes, derived from *in vitro* brightness analysis of FGF2-GFP on PI(4,5)$P_2$-containing liposomes.

With C95 being identified as crucial residue for dimerization and oligomer formation on membranes, and a stable interface being identified in Molecular Dynamics simulation with two FGF2 monomers in water, the question remained on how FGF2 can oligomerize. To investigate FGF2-FGF2 interfaces, I embedded two FGF2 monomers, each bound to the membrane by a single PI(4,5)$P_2$ lipid, into a membrane composed of 70% POPC and 30% cholesterol. From 360 different starting positions, I conducted 500 ns simulations for each configuration. This set of trajectories was utilized by my collaborator, Ilpo Vattulainen (University of Helsinki), to train a model for clustering dimerization interfaces. they applied a Bayesian Gaussian mixture model clustering combined with an artificial neural network-based autoencoder, as published in (111), to analyze all dimeric interfaces. This analysis identified the C95-C95 configuration as the most frequently occurring ensemble Distance analysis of the C95-C95 and the C77-C77 clusters demonstrated that the C95s are within 1 nm, a reasonable distance for disulfide bridge formation, whereas C77-C77 distances were greater than 2 nm, confirming the experimental results on the role of C95 in disulfide bridge formation. Contact analysis between the FGF2 monomers revealed previously identified potential salt-bridges in the C95-C95 interface with E86-K118 and E99-K85 showing high interaction probability during the 360 simulations, stabilizing this interface. Analysis of surface contact areas showed a broader distribution of contact areas, indicating potential further stabilized areas for monomer – monomer contacts.

As FGF2 is hypothesized to dimerize already after recruitment to the plasma membrane, I used preformed, C95-C95 disulfide bridged dimers to investigate oligomeric self-assembly on flat, asymmetric membranes regarding PI(4,5)$P_2$ distribution. I observed oligomerization of 3 dimers into a ring-shaped hexameric unit, which resembled closed-shaped oligomers of FGF2-GFP observed on supported lipid bilayers by atomic force microscopy (111). This hexamer was simulated in all-atoms resolution for another 3 x 5 µs to ensure stability. I first looked into the oligomerization interface and, surprisingly, discovered an asymmetric hexamer conformation and high heterogeneity between the 3 dimer interfaces revealed by contact surface area analysis (Figure 13C). Astoundingly, PI(4,5)$P_2$ was also accumulated in the dimer interface region, potentially stabilizing the interface by hydrogen bonding and salt bridges. Lipid-stabilized weak protein oligomers have been already reported and include eukaryotic proteins like bacterial leucine transporter LeuT, the sugar transporter SemiSWEET, and the $Na^+/H^+$ antiporter NhaA (219). In these cases, oligomerization was directly influenced by cardiolipin concentration within the membrane (219), a negatively charged phospholipid, like PI(4,5)$P_2$, that induces negative curvature and can adopt non-bilayer configurations such as hexagonal phases.

### 4.1.4 Membrane remodeling by the FGF2 hexamer

Given that the lipid diffusion in the all-atoms simulations was very slow and exhibited minimal changes over my microsecond simulations, I coarse-grained the FGF2 hexamer with an elastic network into Martini2.2 to reach statistical relevance for lipid remodeling. The FGF2 hexamer was embedded into a patch of pure PC – cholesterol surrounded by the remaining lipids of the plasma-membrane like lipid mixture with 5 % $PI(4,5)P_2$. This initial configuration, deliberately set far from equilibrium, allowed tracking of lipid diffusion as the system progressed towards a more stable state.

In these simulations, the FGF2 hexamer demonstrated a spatially confined lipid sorting effect in the cytosolic leaflet of the membrane. $PI(4,5)P_2$ levels were greatly enriched by a factor of 3, whereas PC and PS levels were depleted. Within the analyzed area near the hexamer, approximately 220 lipids, 75 % of the lipids were non-bilayer lipids, namely PE (33 %), $PI(4,5)P_2$ (17 %) and cholesterol (25 %) (Figure 15). This spatially restricted accumulation of non-bilayer lipids is hypothesized to create a local environment, where the membrane integrity is impaired. Such conditions may promote the formation of non-bilayer states of the membrane, e.g., hexagonal phases (134), leading to membrane deformations and, ultimately, pore formation.

Additionally, FGF2-induced clustering of $PI(4,5)P_2$, with 4 to 5 molecules per monomer, resulted in a localized accumulation of negative charge, as each $PI(4,5)P_2$ carries a charge of -4 at neutral pH (199). This dense negative charge generates a strong, localized electric field and charge gradient across the membrane. This effect could mimic an electroporation-like rupture, resulting in pore formation (220-222).

$PI(4,5)P_2$ clustering did not only cause formation of a local charge gradient, but also was responsible for formation of negative membrane curvature (Figure 16 & 18). The negative membrane curvature may also promote pore formation. The curvature profile of toroidal pores is complex and size-dependent. With positive curvature in the pore rim region, equatorial curvature is negative for small radii below 2 nm, zero if radius = monolayer thickness, and positive for larger radii (223). A single FGF2 is around 1.5 nm in diameter. With the observed helical, bead-like arrangement of FGF2 monomers inside toroidal pores (Figure 10), it is reasonable to assume that initial pore formation is in this range of small radii. Therefore, negative curvature may also promote pore formation here.

Analysis of lipid tilt angles, the vector between lipid tails and the headgroup regarding the membrane normal, revealed a broad distribution up to 25° in the context of $PI(4,5)P_2$-induced negative curvature. Large lipid tilt angles are known to induce stress to membranes, with the observed tilt angles similar to fusion events at the hemifusion diaphragm (224).

Taken together, the observed effects of the FGF2 hexamer-induced lipid sorting and membrane remodeling strongly suggest that the spatially confined accumulation of non-bilayer lipids, particularly $PI(4,5)P_2$, led to a localized destabilization of the membrane. of the membrane integrity, which resolves in pore formation. This hypothesis is consistent with the

experimentally observed minimal requirement for FGF2-induced pore formation, which is the $PI(4,5)P_2$-dependent oligomerization membranes.

# 5 Future perspectives

Using Molecular Dynamics simulations, I demonstrated that FGF2 self-assembled into ring-shaped oligomers, causing substantial, spatially confined membrane remodeling through the accumulation of highly charged and non-bilayer lipids. This put the membrane into a high-energy state, which is subsequently relaxed into pore formation. This mechanism likely represents the main driving force behind FGF2-induced, $PI(4,5)P_2$-dependent pore formation. Moreover, this mechanism may reflect a general principle by which other pore-forming proteins like Gasdermin D, Bcl-2 associated X protein Bax, bacterial pore-forming toxins, and HIV Tat are able to alter local membrane properties. Closer investigations on membrane remodeling by those proteins could provide valuable insights into how proteins are able to compromise membrane integrity to mediate physiological processes of fundamental importance such as inflammation and angiogenesis.

# 6 References


1. Rapoport, T. A. (2007) Protein translocation across the eukaryotic endoplasmic reticulum and bacterial plasma membranes *Nature* **450**, 663-669 10.1038/nature06384
2. Rabouille, C. (2017) Pathways of Unconventional Protein Secretion *Trends Cell Biol* **27**, 230-240 10.1016/j.tcb.2016.11.007
3. Walter, P., Gilmore, R., and Blobel, G. (1984) Protein translocation across the endoplasmic reticulum *Cell* **38**, 5-8 10.1016/0092-8674(84)90520-8
4. Rapoport, T. A. (1992) Transport of Proteins across the Endoplasmic-Reticulum Membrane *Science* **258**, 931-936 DOI 10.1126/science.1332192
5. Gilmore, R., Blobel, G., and Walter, P. (1982) Protein Translocation across the Endoplasmic-Reticulum .1. Detection in the Microsomal Membrane of a Receptor for the Signal Recognition Particle *Journal of Cell Biology* **95**, 463-469 DOI 10.1083/jcb.95.2.463
6. Deshaies, R. J., Sanders, S. L., Feldheim, D. A., and Schekman, R. (1991) Assembly of Yeast Sec Proteins Involved in Translocation into the Endoplasmic-Reticulum into a Membrane-Bound Multisubunit Complex *Nature* **349**, 806-808 DOI 10.1038/349806a0
7. Rutz, C., Klein, W., and Schulein, R. (2015) N-Terminal Signal Peptides of G Protein-Coupled Receptors: Significance for Receptor Biosynthesis, Trafficking, and Signal Transduction *Prog Mol Biol Transl Sci* **132**, 267-287 10.1016/bs.pmbts.2015.03.003
8. Pfeffer, S., Burbaum, L., Unverdorben, P., Pech, M., Chen, Y. X., Zimmermann, R. *et al.* (2015) Structure of the native Sec61 protein-conducting channel *Nature Communications* **6**, ARTN 8403 10.1038/ncomms9403
9. Jackson, R. C., and Blobel, G. (1977) Post-translational cleavage of presecretory proteins with an extract of rough microsomes from dog pancreas containing signal peptidase activity *Proc Natl Acad Sci U S A* **74**, 5598-5602 10.1073/pnas.74.12.5598
10. Hebert, D. N., Simons, J. F., Peterson, J. R., and Helenius, A. (1995) Calnexin, calreticulin, and Bip/Kar2p in protein folding *Cold Spring Harb Sym* **60**, 405-415 Doi 10.1101/Sqb.1995.060.01.045
11. Kelleher, D. J., Kreibich, G., and Gilmore, R. (1992) Oligosaccharyltransferase Activity Is Associated with a Protein Complex Composed of Ribophorin-I and Ribophorin-Ii and a 48kd Protein *Cell* **69**, 55-65 Doi 10.1016/0092-8674(92)90118-V
12. Homans, S. W., Ferguson, M. A., Dwek, R. A., Rademacher, T. W., Anand, R., and Williams, A. F. (1988) Complete structure of the glycosyl phosphatidylinositol membrane anchor of rat brain Thy-1 glycoprotein *Nature* **333**, 269-272 10.1038/333269a0
13. Vitale, A., Ceriotti, A., and Denecke, J. (1993) The Role of the Endoplasmic-Reticulum in Protein-Synthesis, Modification and Intracellular-Transport *J Exp Bot* **44**, 1417-1444 DOI 10.1093/jxb/44.9.1417
14. Frand, A. R., and Kaiser, C. A. (1998) The ERO1 gene of yeast is required for oxidation of protein dithiols in the endoplasmic reticulum *Mol Cell* **1**, 161-170 10.1016/s1097-2765(00)80017-9
15. Travers, K. J., Patil, C. K., Wodicka, L., Lockhart, D. J., Weissman, J. S., and Walter, P. (2000) Functional and genomic analyses reveal an essential coordination between the

unfolded protein response and ER-associated degradation *Cell* **101**, 249-258 Doi 10.1016/S0092-8674(00)80835-1
16. Rothman, J. E., and Wieland, F. T. (1996) Protein sorting by transport vesicles *Science* **272**, 227-234 10.1126/science.272.5259.227
17. Sato, K. (2004) COPII coat assembly and selective export from the endoplasmic reticulum *J Biochem-Tokyo* **136**, 755-760 10.1093/jb/mvh184
18. Viotti, C. (2016) ER to Golgi-Dependent Protein Secretion: The Conventional Pathway *Methods Mol Biol* **1459**, 3-29 10.1007/978-1-4939-3804-9_1
19. Rothman, J. E. (1985) The Compartmental Organization of the Golgi-Apparatus *Sci Am* **253**, 74-& DOI 10.1038/scientificamerican0985-74
20. Benvenuto, G., Leone, S., Astoricchio, E., Bormke, S., Jasek, S., D'Aniello, E. *et al.* (2024) Evolution of the ribbon-like organization of the Golgi apparatus in animal cells *Cell Reports* **43**, ARTN 113791 10.1016/j.celrep.2024.113791
21. Schweizer, A., Fransen, J. A. M., Bachi, T., Ginsel, L., and Hauri, H. P. (1988) Identification, by a Monoclonal-Antibody, of a 53-Kd Protein Associated with a Tubulo-Vesicular Compartment at the Cis-Side of the Golgi-Apparatus *Journal of Cell Biology* **107**, 1643-1653 DOI 10.1083/jcb.107.5.1643
22. Potelle, S., Klein, A., and Foulquier, F. (2015) Golgi post-translational modifications and associated diseases *J Inherit Metab Dis* **38**, 741-751 10.1007/s10545-015-9851-7
23. Muesch, A., Hartmann, E., Rohde, K., Rubartelli, A., Sitia, R., and Rapoport, T. A. (1990) A novel pathway for secretory proteins? *Trends Biochem Sci* **15**, 86-88 10.1016/0968-0004(90)90186-f
24. Helms, J. B., and Rothman, J. E. (1992) Inhibition by Brefeldin-a of a Golgi Membrane Enzyme That Catalyzes Exchange of Guanine-Nucleotide Bound to Arf *Nature* **360**, 352-354 DOI 10.1038/360352a0
25. Mollenhauer, H. H., Morre, D. J., and Rowe, L. D. (1990) Alteration of Intracellular Traffic by Monensin - Mechanism, Specificity and Relationship to Toxicity *Biochimica Et Biophysica Acta* **1031**, 225-246 Doi 10.1016/0304-4157(90)90008-Z
26. Eilers, U., Klumperman, J., and Hauri, H. P. (1989) Nocodazole, a Microtubule-Active Drug, Interferes with Apical Protein Delivery in Cultured Intestinal Epithelial-Cells (Caco-2) *Journal of Cell Biology* **108**, 13-22 DOI 10.1083/jcb.108.1.13
27. Poschmann, G., Bahr, J., Schrader, J., Stejerean-Todoran, I., Bogeski, I., and Stühler, K. (2022) Secretomics-A Key to a Comprehensive Picture of Unconventional Protein Secretion *Front Cell Dev Biol* **10**, ARTN 878027 10.3389/fcell.2022.878027
28. Rabouille, C., Malhotra, V., and Nickel, W. (2012) Diversity in unconventional protein secretion *J Cell Sci* **125**, 5251-5255 10.1242/jcs.103630
29. Dimou, E., and Nickel, W. (2018) Unconventional mechanisms of eukaryotic protein secretion *Curr Biol* **28**, R406-R410 10.1016/j.cub.2017.11.074
30. Rayne, F., Debaisieux, S., Yezid, H., Lin, Y. L., Mettling, C., Konate, K. *et al.* (2010) Phosphatidylinositol-(4,5)-bisphosphate enables efficient secretion of HIV-1 Tat by infected T-cells *EMBO J* **29**, 1348-1362 10.1038/emboj.2010.32
31. Zeitler, M., Steringer, J. P., Muller, H. M., Mayer, M. P., and Nickel, W. (2015) HIV-Tat Protein Forms Phosphoinositide-dependent Membrane Pores Implicated in Unconventional Protein Secretion *J Biol Chem* **290**, 21976-21984 10.1074/jbc.M115.667097

32. Steringer, J. P., Bleicken, S., Andreas, H., Zacherl, S., Laussmann, M., Temmerman, K. *et al.* (2012) Phosphatidylinositol 4,5-bisphosphate (PI(4,5)P2)-dependent oligomerization of fibroblast growth factor 2 (FGF2) triggers the formation of a lipidic membrane pore implicated in unconventional secretion *J Biol Chem* **287**, 27659-27669 10.1074/jbc.M112.381939
33. Chang, H. C., Samaniego, F., Nair, B. C., Buonaguro, L., and Ensoli, B. (1997) HIV-1 Tat protein exits from cells via a leaderless secretory pathway and binds to extracellular matrix-associated heparan sulfate proteoglycans through its basic region *Aids* **11**, 1421-1431 Doi 10.1097/00002030-199712000-00006
34. Sparn, C., Dimou, E., Meyer, A., Saleppico, R., Wegehingel, S., Gerstner, M. *et al.* (2022) Glypican-1 drives unconventional secretion of fibroblast growth factor 2 *Elife* **11**, ARTN e75545
10.7554/eLife.75545
35. Prudovsky, I., Bagala, C., Tarantini, F., Mandinova, A., Soldi, R., Bellum, S. *et al.* (2002) The intracellular translocation of the components of the fibroblast growth factor 1 release complex precedes their assembly prior to export *Journal of Cell Biology* **158**, 201-208 10.1083/jcb.200203084
36. Carreira, C. M., LaVallee, T. M., Tarantini, F., Jackson, A., Lathrop, J. T., Hampton, B. *et al.* (1998) S100A13 is involved in the regulation of fibroblast growth factor-1 and p40 synaptotagmin-1 release *Journal of Biological Chemistry* **273**, 22224-22231 DOI 10.1074/jbc.273.35.22224
37. Soldi, R., Mandinova, A., Venkataraman, K., Hla, T., Vadas, M., Pitson, S. *et al.* (2007) Sphingosine kinase 1 is a critical component of the copper-dependent FGF1 export pathway *Exp Cell Res* **313**, 3308-3318 10.1016/j.yexcr.2007.05.031
38. Landriscina, M., Soldi, R., Bagalá, C., Micucci, I., Bellum, S., Tarantini, F. *et al.* (2001) S100A13 participates in the release of fibroblast growth factor 1 in response to heat shock *Journal of Biological Chemistry* **276**, 22544-22552 DOI 10.1074/jbc.M100546200
39. Prudovsky, I., Kacer, D., Davis, J., Shah, V., Jayanthi, S., Huber, I. *et al.* (2016) Folding of Fibroblast Growth Factor 1 Is Critical for Its Nonclassical Release *Biochemistry* **55**, 1159-1167 10.1021/acs.biochem.5b01341
40. Tarantini, F., Gamble, S., Jackson, A., and Maciag, T. (1995) The Cysteine Residue Responsible for the Release of Fibroblast Growth-Factor-I Resides in a Domain-Independent of the Domain for Phosphatidylserine Binding *Journal of Biological Chemistry* **270**, 29039-29042 DOI 10.1074/jbc.270.49.29039
41. Kirov, A., Al-Hashimi, H., Solomon, P., Mazur, C., Thorpe, P. E., Sims, P. J. *et al.* (2012) Phosphatidylserine externalization and membrane blebbing are involved in the nonclassical export of FGF1 *Journal of Cellular Biochemistry* **113**, 956-966 10.1002/jcb.23425
42. Weingarten, M. D., Lockwood, A. H., Hwo, S. Y., and Kirschner, M. W. (1975) Protein Factor Essential for Microtubule Assembly *P Natl Acad Sci USA* **72**, 1858-1862 DOI 10.1073/pnas.72.5.1858
43. Alonso, A. D., GrundkeIqbal, I., Barra, H. S., and Iqbal, K. (1997) Abnormal phosphorylation of tan and the mechanism of Alzheimer neurofibrillary degeneration: Sequestration of microtubule-associated proteins 1 and 2 and the disassembly of microtubules by the abnormal tau *P Natl Acad Sci USA* **94**, 298-303 DOI 10.1073/pnas.94.1.298

44. Goedert, M. (1999) Filamentous nerve cell inclusions in neurodegenerative diseases:: tauopathies and α-synucleinopathies *Philos T Roy Soc B* **354**, 1101-1118 DOI 10.1098/rstb.1999.0466
45. Creekmore, B. C., Watanabe, R., and Lee, E. B. (2024) Neurodegenerative Disease Tauopathies *Annu Rev Pathol-Mech* **19**, 345-370 10.1146/annurev-pathmechdis-051222-120750
46. Merezhko, M., Uronen, R. L., and Huttunen, H. J. (2020) The Cell Biology of Tau Secretion *Frontiers in Molecular Neuroscience* **13**, ARTN 569818 10.3389/fnmol.2020.569818
47. Katsinelos, T., Zeitler, M., Dimou, E., Karakatsani, A., Müller, H. M., Nachman, E. *et al.* (2018) Unconventional Secretion Mediates the Trans-cellular Spreading of Tau *Cell Reports* **23**, 2039-2055 10.1016/j.celrep.2018.04.056
48. Holmes, B., DeVos, S., Kfoury, N., Miller, T., Papy-Garcia, D., and Diamond, M. (2013) Heparan sulfate proteoglycans mediate internalization and propagation of specific proteopathic seeds *Glycobiology* **23**, 1409-1409
49. Piccioli, P., and Rubartelli, A. (2013) The secretion of IL-1β and options for release *Semin Immunol* **25**, 425-429 10.1016/j.smim.2013.10.007
50. Brough, D., and Rothwell, N. J. (2007) Caspase-1-dependent processing of pro-interleukin-1β is cytosolic and precedes cell death *Journal of Cell Science* **120**, 772-781 10.1242/jcs.03377
51. Schaefer, S. L., and Hummer, G. (2022) Sublytic gasdermin-D pores captured in atomistic molecular simulations *Elife* **11**, 10.7554/eLife.81432
52. Fath, M. J., and Kolter, R. (1993) Abc Transporters - Bacterial Exporters *Microbiol Rev* **57**, 995-1017 Doi 10.1128/Mmbr.57.4.995-1017.1993
53. Thomas, C., Aller, S. G., Beis, K., Carpenter, E. P., Chang, G., Chen, L. *et al.* (2020) Structural and functional diversity calls for a new classification of ABC transporters *Febs Letters* **594**, 3767-3775 10.1002/1873-3468.13935
54. Michaelis, S., and Herskowitz, I. (1988) The a-Factor Pheromone of Saccharomyces-Cerevisiae Is Essential for Mating *Mol Cell Biol* **8**, 1309-1318 Doi 10.1128/Mcb.8.3.1309
55. Kuchler, K., Dohlman, H. G., and Thorner, J. (1993) The a-Factor Transporter (Ste6 Gene-Product) and Cell Polarity in the Yeast Saccharomyces-Cerevisiae *Journal of Cell Biology* **120**, 1203-1215 DOI 10.1083/jcb.120.5.1203
56. Stegmayer, C., Kehlenbach, A., Tournaviti, S., Wegehingel, S., Zehe, C., Denny, P. *et al.* (2005) Direct transport across the plasma membrane of mammalian cells of HASPB as revealed by a CHO export mutant *Journal of Cell Science* **118**, 517-527 10.1242/jcs.01645
57. Denny, P. W., Gokool, S., Russell, D. G., Field, M. C., and Smith, D. F. (2000) Acylation-dependent protein export in *Journal of Biological Chemistry* **275**, 11017-11025 DOI 10.1074/jbc.275.15.11017
58. Kim, J., Gee, H. Y., and Lee, M. G. (2018) Unconventional protein secretion - new insights into the pathogenesis and therapeutic targets of human diseases *Journal of Cell Science* **131**, ARTN jcs213686 10.1242/jcs.213686
59. Duran, J. M., Anjard, C., Stefan, C., Loomis, W. F., and Malhotra, V. (2010) Unconventional secretion of Acb1 is mediated by autophagosomes *Journal of Cell Biology* **188**, 527-536 10.1083/jcb.200911154

60. Curwin, A. J., Brouwers, N., Adell, M. A. Y., Teis, D., Turacchio, G., Parashuraman, S. *et al.* (2016) ESCRT-III drives the final stages of CUPS maturation for unconventional protein secretion *Elife* **5**, ARTN e16299 10.7554/eLife.16299
61. Short, B. (2011) CUPS provide a handle on Acb1 secretion *Journal of Cell Biology* **195**, 922-922 10.1083/jcb.1956iti2
62. Zhang, M., Kenny, S. J., Ge, L., Xu, K., and Schekman, R. (2015) Translocation of interleukin-1β into a vesicle intermediate in autophagy-mediated secretion *Elife* **4**, ARTN e11205 10.7554/eLife.11205
63. Dupont, N., Jiang, S. Y., Pilli, M., Ornatowski, W., Bhattacharya, D., and Deretic, V. (2011) Autophagy-based unconventional secretory pathway for extracellular delivery of IL-1β *Embo Journal* **30**, 4701-4711 10.1038/emboj.2011.398
64. Giuliani, F., Grieve, A., and Rabouille, C. (2011) Unconventional secretion: a on GRASP *Current Opinion in Cell Biology* **23**, 498-504 10.1016/j.ceb.2011.04.005
65. Riordan, J. R., Rommens, J. M., Kerem, B. S., Alon, N., Rozmahel, R., Grzelczak, Z. *et al.* (1989) Identification of the Cystic-Fibrosis Gene - Cloning and Characterization of Complementary-DNA *Science* **245**, 1066-1072
66. Kim, S. J., and Skach, W. R. (2012) Mechanisms of CFTR folding at the endoplasmic reticulum *Frontiers in Pharmacology* **3**, ARTN 201 10.3389/fphar.2012.00201
67. Bannykh, S. I., Bannykh, G. I., Fish, K. N., Moyer, B. D., Riordan, J. R., and Balch, W. E. (2000) Traffic pattern of cystic fibrosis transmembrane regulator through the early exocytic pathway *Traffic* **1**, 852-870 DOI 10.1034/j.1600-0854.2000.011105.x
68. Farinha, C. M., and Canato, S. (2017) From the endoplasmic reticulum to the plasma membrane: mechanisms of CFTR folding and trafficking *Cellular and Molecular Life Sciences* **74**, 39-55 10.1007/s00018-016-2387-7
69. Gee, H. Y., Noh, S. H., Tang, B. L., Kim, K. H., and Lee, M. G. (2011) Rescue of ΔF508-CFTR Trafficking via a GRASP-Dependent Unconventional Secretion Pathway *Cell* **146**, 746-760 10.1016/j.cell.2011.07.021
70. Beenken, A., and Mohammadi, M. (2009) The FGF family: biology, pathophysiology and therapy *Nature Reviews Drug Discovery* **8**, 235-253 10.1038/nrd2792
71. Beenken, A., and Mohammadi, M. (2009) The FGF family: biology, pathophysiology and therapy *Nat Rev Drug Discov* **8**, 235-253 10.1038/nrd2792
72. Biadun, M., Sochacka, M., Karelus, R., Baran, K., Czyrek, A., Otlewski, J. *et al.* (2023) FGF homologous factors are secreted from cells to induce FGFR-mediated anti-apoptotic response *Faseb Journal* **37**, ARTN e23043 10.1096/fj.202300324R
73. Dahl, J. P., Binda, A., Canfield, V. A., and Levenson, R. (2000) Participation of Na,K-ATPase in FGF-2 secretion: rescue of ouabain-inhibitable FGF-2 secretion by ouabain-resistant Na,K-ATPase alpha subunits *Biochemistry* **39**, 14877-14883 10.1021/bi001073y
74. Zacherl, S., La Venuta, G., Muller, H. M., Wegehingel, S., Dimou, E., Sehr, P. *et al.* (2015) A direct role for ATP1A1 in unconventional secretion of fibroblast growth factor 2 *J Biol Chem* **290**, 3654-3665 10.1074/jbc.M114.590067
75. Biadun, M., Sochacka, M., Kalka, M., Chorazewska, A., Karelus, R., Krowarsch, D. *et al.* (2024) Uncovering key steps in FGF12 cellular release reveals a common mechanism

for unconventional FGF protein secretion *Cell Mol Life Sci* **81**, 356 10.1007/s00018-024-05396-9

76. Raman, R., Venkataraman, G., Ernst, S., Sasisekharan, V., and Sasisekharan, R. (2003) Structural specificity of heparin binding in the fibroblast growth factor family of proteins *Proc Natl Acad Sci U S A* **100**, 2357-2362 10.1073/pnas.0437842100
77. Miyakawa, K., Hatsuzawa, K., Kurokawa, T., Asada, M., Kuroiwa, T., and Imamura, T. (1999) A hydrophobic region locating at the center of fibroblast growth factor-9 is crucial for its secretion *Journal of Biological Chemistry* **274**, 29352-29357 DOI 10.1074/jbc.274.41.29352
78. Miyakawa, K., and Imamura, T. (2003) Secretion of FGF-16 requires an uncleaved bipartite signal sequence *Journal of Biological Chemistry* **278**, 35718-35724 10.1074/jbc.M300690200
79. Ohmachi, S., Watanabe, Y., Mikami, T., Kusu, N., Ibi, T., Akaike, A. *et al.* (2000) FGF-20, a novel neurotrophic factor, preferentially expressed in the substantia nigra pars compacta of rat brain *Biochem Bioph Res Co* **277**, 355-360 DOI 10.1006/bbrc.2000.3675
80. Chen, L. F., Fu, L. L., Sun, J. C., Huang, Z. Q., Fang, M. Z., Zinkle, A. *et al.* (2023) Structural basis for FGF hormone signaling *Nature* **618**, 862-+ 10.1038/s41586-023-06155-9
81. Fukumoto, S. (2008) Actions and mode of actions of FGF19 subfamily members *Endocr J* **55**, 23-31 DOI 10.1507/endocrj.KR07E-002
82. Fantl, W. J., Johnson, D. E., and Williams, L. T. (1993) Signaling by Receptor Tyrosine Kinases *Annu Rev Biochem* **62**, 453-481 DOI 10.1146/annurev.bi.62.070193.002321
83. Bateman, A., and Chothia, C. (1995) Outline Structures for the Extracellular Domains of the Fibroblast Growth-Factor Receptors *Nat Struct Biol* **2**, 1068-1074 DOI 10.1038/nsb1295-1068
84. Powers, C. J., McLeskey, S. W., and Wellstein, A. (2000) Fibroblast growth factors, their receptors and signaling *Endocr-Relat Cancer* **7**, 165-197 DOI 10.1677/erc.0.0070165
85. Yayon, A., Klagsbrun, M., Esko, J. D., Leder, P., and Ornitz, D. M. (1991) Cell-Surface, Heparin-Like Molecules Are Required for Binding of Basic Fibroblast Growth-Factor to Its High-Affinity Receptor *Cell* **64**, 841-848 Doi 10.1016/0092-8674(91)90512-W
86. Nugent, M. A., and Edelman, E. R. (1992) Kinetics of Basic Fibroblast Growth-Factor Binding to Its Receptor and Heparan-Sulfate Proteoglycan - a Mechanism for Cooperativity *Biochemistry* **31**, 8876-8883 DOI 10.1021/bi00152a026
87. Kan, M. K., Wang, F., Xu, J. M., Crabb, J. W., Hou, J. Z., and Mckeehan, W. L. (1993) An Essential Heparin-Binding Domain in the Fibroblast Growth-Factor Receptor Kinase *Science* **259**, 1918-1921 DOI 10.1126/science.8456318
88. Ornitz, D. M. (2000) FGFs, heparan sulfate and FGFRs: complex interactions essential for development *Bioessays* **22**, 108-112 Doi 10.1002/(Sici)1521-1878(200002)22:2<108::Aid-Bies2>3.0.Co;2-M
89. Furdui, C. M., Lew, E. D., Schlessinger, J., and Anderson, K. S. (2006) Autophosphorylation of FGFR1 kinase is mediated by a sequential and precisely ordered reaction *Molecular Cell* **21**, 711-717 10.1016/j.molcel.2006.01.022
90. Ornitz, D. M., and Itoh, N. (2015) The Fibroblast Growth Factor signaling pathway *Wires Dev Biol* **4**, 215-266 10.1002/wdev.176
91. Eswarakumar, V. P., Lax, I., and Schlessinger, J. (2005) Cellular signaling by fibroblast growth factor receptors *Cytokine & Growth Factor Reviews* **16**, 139-149 10.1016/j.cytogfr.2005.01.001

92. Helsten, T., Schwaederle, M., and Kurzrock, R. (2015) Fibroblast growth factor receptor signaling in hereditary and neoplastic disease: biologic and clinical implications *Cancer Metast Rev* **34**, 479-496 10.1007/s10555-015-9579-8
93. Ornitz, D. M., and Marie, P. J. (2015) Fibroblast growth factor signaling in skeletal development and disease *Gene Dev* **29**, 1463-1486 10.1101/gad.266551.115
94. Xie, Y. L., Su, N., Yang, J., Tan, Q. Y., Huang, S., Jin, M. *et al.* (2020) FGF/FGFR signaling in health and disease *Signal Transduct Tar* **5**, ARTN 181 10.1038/s41392-020-00222-7
95. Akl, M. R., Nagpal, P., Ayoub, N. M., Tai, B., Prabhu, S. A., Capac, C. M. *et al.* (2016) Molecular and clinical significance of fibroblast growth factor 2 (FGF2 /bFGF) in malignancies of solid and hematological cancers for personalized therapies *Oncotarget* **7**, 44735-44762 10.18632/oncotarget.8203
96. Liao, S., Bodmer, J., Pietras, D., Azhar, M., Doetschman, T., and Schultz, J. E. J. (2009) Biological Functions of the Low and High Molecular Weight Protein Isoforms of Fibroblast Growth Factor-2 in Cardiovascular Development and Disease *Dev Dynam* **238**, 249-264 10.1002/dvdy.21677
97. Sorensen, V., Nilsen, T., and Wiedlocha, A. (2006) Functional diversity of FGF-2 isoforms by intracellular sorting *Bioessays* **28**, 504-514 DOI 10.1002/bies.20405
98. Bugler, B., Amalric, F., and Prats, H. (1991) Alternative Initiation of Translation Determines Cytoplasmic or Nuclear-Localization of Basic Fibroblast Growth-Factor *Mol Cell Biol* **11**, 573-577 Doi 10.1128/Mcb.11.1.573
99. Cailliau, K., Browaeys-Poly, E., and Vilain, J. P. (2001) Fibroblast growth factors 1 and 2 differently activate MAP kinase in Xenopus oocytes expressing fibroblast growth factor receptors 1 and 4 *Biochim Biophys Acta* **1538**, 228-233 10.1016/s0167-4889(01)00074-x
100. Korc, M., and Friesel, R. E. (2009) The Role of Fibroblast Growth Factors in Tumor Growth *Curr Cancer Drug Tar* **9**, 639-651 Doi 10.2174/156800909789057006
101. Ornitz, D. M., Xu, J. S., Colvin, J. S., McEwen, D. G., MacArthur, C. A., Coulier, F. *et al.* (1996) Receptor specificity of the fibroblast growth factor family *Journal of Biological Chemistry* **271**, 15292-15297 DOI 10.1074/jbc.271.25.15292
102. Zhang, X. Q., Ibrahimi, O. A., Olsen, S. K., Umemori, H., Mohammadi, M., and Ornitz, D. M. (2006) Receptor specificity of the fibroblast growth factor family - The complete mammalian FGF family *Journal of Biological Chemistry* **281**, 15694-15700 10.1074/jbc.M601252200
103. Basilico, C., and Moscatelli, D. (1992) The Fgf Family of Growth-Factors and Oncogenes *Adv Cancer Res* **59**, 115-165 Doi 10.1016/S0065-230x(08)60305-X
104. Bikfalvi, A., Klein, S., Pintucci, G., and Rifkin, D. B. (1997) Biological roles of fibroblast growth factor-2 *Endocr Rev* **18**, 26-45 DOI 10.1210/er.18.1.26
105. Jeong, M., Bojkovic, K., Sagi, V., and Stankovic, K. M. (2021) Molecular and Clinical Significance of Fibroblast Growth Factor 2 in Development and Regeneration of the Auditory System *Front Mol Neurosci* **14**, 757441 10.3389/fnmol.2021.757441
106. Gospodarowicz, D. (1974) Localization of a Fibroblast Growth-Factor and Its Effect Alone and with Hydrocortisone on 3t3 Cell-Growth *Nature* **249**, 123-127 DOI 10.1038/249123a0
107. Abraham, J. A., Mergia, A., Whang, J. L., Tumolo, A., Friedman, J., Hjerrild, K. A. *et al.* (1986) Nucleotide-Sequence of a Bovine Clone Encoding the Angiogenic Protein, Basic Fibroblast Growth-Factor *Science* **233**, 545-548 DOI 10.1126/science.2425435

108. Zhang, J. D., Cousens, L. S., Barr, P. J., and Sprang, S. R. (1991) 3-Dimensional Structure of Human Basic Fibroblast Growth-Factor, a Structural Homolog of Interleukin-1-Beta *P Natl Acad Sci USA* **88**, 3446-3450 DOI 10.1073/pnas.88.8.3446
109. Ago, H., Kitagawa, Y., Fujishima, A., Matsuura, Y., and Katsube, Y. (1991) Crystal-Structure of Basic Fibroblast Growth-Factor at 1.6 a Resolution *J Biochem-Tokyo* **110**, 360-363 DOI 10.1093/oxfordjournals.jbchem.a123586
110. Zhu, X., Komiya, H., Chirino, A., Faham, S., Fox, G. M., Arakawa, T. *et al.* (1991) 3-Dimensional Structures of Acidic and Basic Fibroblast Growth-Factors *Science* **251**, 90-93 DOI 10.1126/science.1702556
111. Lolicato, F., Steringer, J. P., Saleppico, R., Beyer, D., Fernandez-Sobaberas, J., Unger, S. *et al.* (2024) Disulfide bridge-dependent dimerization triggers FGF2 membrane translocation into the extracellular space *Elife* **12**, 10.7554/eLife.88579
112. Temmerman, K., Ebert, A. D., Müller, H. M., Sinning, I., Tews, I., and Nickel, W. (2008) A Direct Role for Phosphatidylinositol-4,5-bisphosphate in Unconventional Secretion of Fibroblast Growth Factor 2 *Traffic* **9**, 1204-1217 10.1111/j.1600-0854.2008.00749.x
113. Steringer, J. P., Lange, S., Cujova, S., Sachl, R., Poojari, C., Lolicato, F. *et al.* (2017) Key steps in unconventional secretion of fibroblast growth factor 2 reconstituted with purified components *Elife* **6**, 10.7554/eLife.28985
114. Legrand, C., Saleppico, R., Sticht, J., Lolicato, F., Muller, H. M., Wegehingel, S. *et al.* (2020) The Na,K-ATPase acts upstream of phosphoinositide PI(4,5)P2 facilitating unconventional secretion of Fibroblast Growth Factor 2 *Commun Biol* **3**, 141 10.1038/s42003-020-0871-y
115. Legrand, C. (2020) *Unravelling the role of the Sodium Potassium ATPase in unconventional secretion of FGF2*,
116. Dahl, J. P., Binda, A., Canfield, V. A., and Levenson, R. (2000) Participation of Na,K-ATPase in FGF-2 secretion:: Rescue of ouabain-inhibitable FGF-2 secretion by ouabain-resistant Na,K-ATPase α subunits *Biochemistry* **39**, 14877-14883 DOI 10.1021/bi001073y
117. Ebert, A. D., Laussmann, M., Wegehingel, S., Kaderali, L., Erfle, H., Reichert, J. *et al.* (2010) Tec-kinase-mediated phosphorylation of fibroblast growth factor 2 is essential for unconventional secretion *Traffic* **11**, 813-826 10.1111/j.1600-0854.2010.01059.x
118. La Venuta, G., Wegehingel, S., Sehr, P., Muller, H. M., Dimou, E., Steringer, J. P. *et al.* (2016) Small Molecule Inhibitors Targeting Tec Kinase Block Unconventional Secretion of Fibroblast Growth Factor 2 *J Biol Chem* **291**, 17787-17803 10.1074/jbc.M116.729384
119. Muller, H. M., Steringer, J. P., Wegehingel, S., Bleicken, S., Munster, M., Dimou, E. *et al.* (2015) Formation of disulfide bridges drives oligomerization, membrane pore formation, and translocation of fibroblast growth factor 2 to cell surfaces *J Biol Chem* **290**, 8925-8937 10.1074/jbc.M114.622456
120. Guglier, S., Hricovini, M., Raman, R., Polito, L., Torri, G., Casu, B. *et al.* (2008) Minimum FGF2 binding structural requirements of heparin and heparan sulfate oligosaccharides as determined by NMR spectroscopy *Biochemistry* **47**, 13862-13869 10.1021/bi801007p
121. Engling, A., Backhaus, R., Stegmayer, C., Zehe, C., Seelenmeyer, C., Kehlenbach, A. *et al.* (2002) Biosynthetic FGF-2 is targeted to non-lipid raft microdomains following translocation to the extracellular surface of CHO cells *J Cell Sci* **115**, 3619-3631 10.1242/jcs.00036

122. Zehe, C., Engling, A., Wegehingel, S., Schafer, T., and Nickel, W. (2006) Cell-surface heparan sulfate proteoglycans are essential components of the unconventional export machinery of FGF-2 *Proc Natl Acad Sci U S A* **103**, 15479-15484 10.1073/pnas.0605997103
123. Backhaus, R., Zehe, C., Wegehingel, S., Kehlenbach, A., Schwappach, B., and Nickel, W. (2004) Unconventional protein secretion: membrane translocation of FGF-2 does not require protein unfolding *Journal of Cell Science* **117**, 1727-1736 10.1242/jcs.01027
124. Dimou, E., Cosentino, K., Platonova, E., Ros, U., Sadeghi, M., Kashyap, P. *et al.* (2019) Single event visualization of unconventional secretion of FGF2 *J Cell Biol* **218**, 683-699 10.1083/jcb.201802008
125. Balla, T. (2013) Phosphoinositides: tiny lipids with giant impact on cell regulation *Physiol Rev* **93**, 1019-1137 10.1152/physrev.00028.2012
126. Jiang, Z., Redfern, R. E., Isler, Y., Ross, A. H., and Gericke, A. (2014) Cholesterol stabilizes fluid phosphoinositide domains *Chem Phys Lipids* **182**, 52-61 10.1016/j.chemphyslip.2014.02.003
127. Laux, T., Fukami, K., Thelen, M., Golub, T., Frey, D., and Caroni, P. (2000) GAP43, MARCKS, and CAP23 modulate PI(4,5)P(2) at plasmalemmal rafts, and regulate cell cortex actin dynamics through a common mechanism *J Cell Biol* **149**, 1455-1472 10.1083/jcb.149.7.1455
128. Stahelin, R. V., Scott, J. L., and Frick, C. T. (2014) Cellular and molecular interactions of phosphoinositides and peripheral proteins *Chemistry and Physics of Lipids* **182**, 3-18 10.1016/j.chemphyslip.2014.02.002
129. Honigmann, A., van den Bogaart, G., Iraheta, E., Risselada, H. J., Milovanovic, D., Mueller, V. *et al.* (2013) Phosphatidylinositol 4,5-bisphosphate clusters act as molecular beacons for vesicle recruitment *Nat Struct Mol Biol* **20**, 679-686 10.1038/nsmb.2570
130. Levental, I., Christian, D. A., Wang, Y. H., Madara, J. J., Discher, D. E., and Janmey, P. A. (2009) Calcium-dependent lateral organization in phosphatidylinositol 4,5-bisphosphate (PIP2)- and cholesterol-containing monolayers *Biochemistry* **48**, 8241-8248 10.1021/bi9007879
131. Rusinova, R., Hobart, E. A., Koeppe, R. E., 2nd, and Andersen, O. S. (2013) Phosphoinositides alter lipid bilayer properties *J Gen Physiol* **141**, 673-690 10.1085/jgp.201310960
132. Fujita, A., Cheng, J., Tauchi-Sato, K., Takenawa, T., and Fujimoto, T. (2009) A distinct pool of phosphatidylinositol 4,5-bisphosphate in caveolae revealed by a nanoscale labeling technique *Proc Natl Acad Sci U S A* **106**, 9256-9261 10.1073/pnas.0900216106
133. Wen, Y., Vogt, V. M., and Feigenson, G. W. (2021) PI(4,5)P(2) Clustering and Its Impact on Biological Functions *Annu Rev Biochem* **90**, 681-707 10.1146/annurev-biochem-070920-094827
134. Jouhet, J. (2013) Importance of the hexagonal lipid phase in biological membrane organization *Front Plant Sci* **4**, 494 10.3389/fpls.2013.00494
135. Levental, I., Cebers, A., and Janmey, P. A. (2008) Combined electrostatics and hydrogen bonding determine intermolecular interactions between polyphosphoinositides *J Am Chem Soc* **130**, 9025-9030 10.1021/ja800948c
136. Lupyan, D., Mezei, M., Logothetis, D. E., and Osman, R. (2010) A molecular dynamics investigation of lipid bilayer perturbation by PIP2 *Biophys J* **98**, 240-247 10.1016/j.bpj.2009.09.063

137. Allolio, C., and Harries, D. (2021) Calcium Ions Promote Membrane Fusion by Forming Negative-Curvature Inducing Clusters on Specific Anionic Lipids *Acs Nano* **15**, 12880-12887 10.1021/acsnano.0c08614
138. Lin, X., Wang, H., Lou, Z., Cao, M., Zhang, Z., and Gu, N. (2018) Roles of PIP2 in the membrane binding of MIM I-BAR: insights from molecular dynamics simulations *FEBS Lett* **592**, 2533-2542 10.1002/1873-3468.13186
139. Wen, Y., Vogt, V. M., and Feigenson, G. W. (2018) Multivalent Cation-Bridged PI(4,5)P(2) Clusters Form at Very Low Concentrations *Biophys J* **114**, 2630-2639 10.1016/j.bpj.2018.04.048
140. Treibs, A., and Kreuzer, F. H. (1968) Di- and Tri-Pyrrylmethene Complexes with Di-Fluoro Boron *Liebigs Ann Chem* **718**, 208-+
141. Schmitt, A., Hinkeldey, B., Wild, M., and Jung, G. (2009) Synthesis of the core compound of the BODIPY dye class: 4,4'-difluoro-4-bora-(3a,4a)-diaza-s-indacene *J Fluoresc* **19**, 755-758 10.1007/s10895-008-0446-7
142. Chan, R., Uchil, P. D., Jin, J., Shui, G., Ott, D. E., Mothes, W. *et al.* (2008) Retroviruses human immunodeficiency virus and murine leukemia virus are enriched in phosphoinositides *J Virol* **82**, 11228-11238 10.1128/JVI.00981-08
143. Frankel, A. D., and Young, J. A. (1998) HIV-1: fifteen proteins and an RNA *Annu Rev Biochem* **67**, 1-25 10.1146/annurev.biochem.67.1.1
144. Wen, Y., Feigenson, G. W., Vogt, V. M., and Dick, R. A. (2020) Mechanisms of PI(4,5)P2 Enrichment in HIV-1 Viral Membranes *J Mol Biol* **432**, 5343-5364 10.1016/j.jmb.2020.07.018
145. Kerfeld, C. A., Sawaya, M. R., Tanaka, S., Nguyen, C. V., Phillips, M., Beeby, M. *et al.* (2005) Protein structures forming the shell of primitive bacterial organelles *Science* **309**, 936-938 10.1126/science.1113397
146. Bilkova, E., Pleskot, R., Rissanen, S., Sun, S., Czogalla, A., Cwiklik, L. *et al.* (2017) Calcium Directly Regulates Phosphatidylinositol 4,5-Bisphosphate Headgroup Conformation and Recognition *J Am Chem Soc* **139**, 4019-4024 10.1021/jacs.6b11760
147. Papahadjopoulos, D., Vail, W. J., Pangborn, W. A., and Poste, G. (1976) Studies on membrane fusion. II. Induction of fusion in pure phospholipid membranes by calcium ions and other divalent metals *Biochim Biophys Acta* **448**, 265-283 10.1016/0005-2736(76)90241-8
148. Kachar, B., Fuller, N., and Rand, R. P. (1986) Morphological responses to calcium-induced interaction of phosphatidylserine-containing vesicles *Biophys J* **50**, 779-788 10.1016/S0006-3495(86)83518-4
149. Churchward, M. A., Rogasevskaia, T., Brandman, D. M., Khosravani, H., Nava, P., Atkinson, J. K. *et al.* (2008) Specific lipids supply critical negative spontaneous curvature--an essential component of native Ca2+-triggered membrane fusion *Biophys J* **94**, 3976-3986 10.1529/biophysj.107.123984
150. Alder, B. J., and Wainwright, T. E. (1957) Phase Transition for a Hard Sphere System *J Chem Phys* **27**, 1208-1209 Doi 10.1063/1.1743957
151. McCammon, J. A., Gelin, B. R., and Karplus, M. (1977) Dynamics of folded proteins *Nature* **267**, 585-590 10.1038/267585a0
152. Hollingsworth, S. A., and Dror, R. O. (2018) Molecular Dynamics Simulation for All *Neuron* **99**, 1129-1143 10.1016/j.neuron.2018.08.011
153. Born, M., and Oppenheimer, R. (1927) Quantum theory of molecules *Ann Phys-Berlin* **84**, 0457-0484

154. Hockney, R. W., Goel, S. P., and Eastwood, J. W. (1974) Quiet High-Resolution Computer Models of a Plasma *J Comput Phys* **14**, 148-158 Doi 10.1016/0021-9991(74)90010-2
155. Hooke, M. D. (1678) *Lectures de potentia restitutiva, or of spring, explaining the power of springing bodies*, Lond
156. Jones, J. E. (1924) On the determination of molecular fields - II From the equation of state of a gas *P R Soc Lond a-Conta* **106**, 463-477 DOI 10.1098/rspa.1924.0082
157. Coulomb, C. A. (1785) *Premier Memoire sur l'slectricite et le magnetisme*, Paris
158. Darden, T., York, D., and Pedersen, L. (1993) Particle Mesh Ewald - an N.Log(N) Method for Ewald Sums in Large Systems *J Chem Phys* **98**, 10089-10092 Doi 10.1063/1.464397
159. Tironi, I. G., Sperb, R., Smith, P. E., and Vangunsteren, W. F. (1995) A Generalized Reaction Field Method for Molecular-Dynamics Simulations *J Chem Phys* **102**, 5451-5459 Doi 10.1063/1.469273
160. Fourier, J. B. J., and Freeman, A. (1878) *The analytical theory of heat*, The University press; etc., Cambridge Eng.
161. Klauda, J. B., Venable, R. M., Freites, J. A., O'Connor, J. W., Tobias, D. J., Mondragon-Ramirez, C. *et al.* (2010) Update of the CHARMM all-atom additive force field for lipids: validation on six lipid types *J Phys Chem B* **114**, 7830-7843 10.1021/jp101759q
162. Best, R. B., Zhu, X., Shim, J., Lopes, P. E., Mittal, J., Feig, M. *et al.* (2012) Optimization of the additive CHARMM all-atom protein force field targeting improved sampling of the backbone phi, psi and side-chain chi(1) and chi(2) dihedral angles *J Chem Theory Comput* **8**, 3257-3273 10.1021/ct300400x
163. Marrink, S. J., Risselada, H. J., Yefimov, S., Tieleman, D. P., and de Vries, A. H. (2007) The MARTINI force field: coarse grained model for biomolecular simulations *J Phys Chem B* **111**, 7812-7824 10.1021/jp071097f
164. Souza, P. C. T., Alessandri, R., Barnoud, J., Thallmair, S., Faustino, I., Grunewald, F. *et al.* (2021) Martini 3: a general purpose force field for coarse-grained molecular dynamics *Nat Methods* **18**, 382-388 10.1038/s41592-021-01098-3
165. Javanainen, M., Martinez-Seara, H., and Vattulainen, I. (2017) Excessive aggregation of membrane proteins in the Martini model *PLoS One* **12**, e0187936 10.1371/journal.pone.0187936
166. Bekker, H., Dijkstra, E. J., Renardus, M. K. R., and Berendsen, H. J. C. (1995) An Efficient, Box Shape Independent Nonbonded Force and Virial Algorithm for Molecular-Dynamics *Mol Simulat* **14**, 137-151 Doi 10.1080/08927029508022012
167. Camley, B. A., Lerner, M. G., Pastor, R. W., and Brown, F. L. (2015) Strong influence of periodic boundary conditions on lateral diffusion in lipid bilayer membranes *J Chem Phys* **143**, 243113 10.1063/1.4932980
168. Nose, S. (1984) A Unified Formulation of the Constant Temperature Molecular-Dynamics Methods *J Chem Phys* **81**, 511-519 Doi 10.1063/1.447334
169. Parrinello, M., and Rahman, A. (1981) Polymorphic Transitions in Single-Crystals - a New Molecular-Dynamics Method *J Appl Phys* **52**, 7182-7190 Doi 10.1063/1.328693
170. Berendsen, H. J. C., Postma, J. P. M., Vangunsteren, W. F., Dinola, A., and Haak, J. R. (1984) Molecular-Dynamics with Coupling to an External Bath *J Chem Phys* **81**, 3684-3690 Doi 10.1063/1.448118
171. Evans, D. J., and Holian, B. L. (1985) The Nose-Hoover Thermostat *J Chem Phys* **83**, 4069-4074 Doi 10.1063/1.449071
172. Maxwell, J. C., and Wiley Digital Archives British Association for the Advancement of, S. (1860) *Illustrations of the dynamical theory of gases*, John Wiley & Sons, Inc, S.l.

173. Boltzmann, L. (1866) *[Papers from the Sitzungsberichte der Kais. Akademie der Wissenschaften. Math.-Nat. Classe*, s.n, Wien
174. Lolicato, F., Saleppico, R., Griffo, A., Meyer, A., Scollo, F., Pokrandt, B. *et al.* (2022) Cholesterol promotes clustering of PI(4,5)P2 driving unconventional secretion of FGF2 *J Cell Biol* **221**, 10.1083/jcb.202106123
175. Kim, H., Fabian, B., and Hummer, G. (2023) Neighbor List Artifacts in Molecular Dynamics Simulations *J Chem Theory Comput* **19**, 8919-8929 10.1021/acs.jctc.3c00777
176. Boyd, K. J., and May, E. R. (2018) BUMPy: A Model-Independent Tool for Constructing Lipid Bilayers of Varying Curvature and Composition *J Chem Theory Comput* **14**, 6642-6652 10.1021/acs.jctc.8b00765
177. Majumder, A., and Straub, J. E. (2021) Addressing the Excessive Aggregation of Membrane Proteins in the MARTINI Model *J Chem Theory Comput* **17**, 2513-2521 10.1021/acs.jctc.0c01253
178. Jo, S., Kim, T., Iyer, V. G., and Im, W. (2008) CHARMM-GUI: a web-based graphical user interface for CHARMM *J Comput Chem* **29**, 1859-1865 10.1002/jcc.20945
179. Jo, S., Lim, J. B., Klauda, J. B., and Im, W. (2009) CHARMM-GUI Membrane Builder for mixed bilayers and its application to yeast membranes *Biophys J* **97**, 50-58 10.1016/j.bpj.2009.04.013
180. Brooks, B. R., Brooks, C. L., 3rd, Mackerell, A. D., Jr., Nilsson, L., Petrella, R. J., Roux, B. *et al.* (2009) CHARMM: the biomolecular simulation program *J Comput Chem* **30**, 1545-1614 10.1002/jcc.21287
181. Wu, E. L., Cheng, X., Jo, S., Rui, H., Song, K. C., Davila-Contreras, E. M. *et al.* (2014) CHARMM-GUI Membrane Builder toward realistic biological membrane simulations *J Comput Chem* **35**, 1997-2004 10.1002/jcc.23702
182. Jo, S., Cheng, X., Islam, S. M., Huang, L., Rui, H., Zhu, A. *et al.* (2014) CHARMM-GUI PDB manipulator for advanced modeling and simulations of proteins containing nonstandard residues *Adv Protein Chem Struct Biol* **96**, 235-265 10.1016/bs.apcsb.2014.06.002
183. Qi, Y., Ingolfsson, H. I., Cheng, X., Lee, J., Marrink, S. J., and Im, W. (2015) CHARMM-GUI Martini Maker for Coarse-Grained Simulations with the Martini Force Field *J Chem Theory Comput* **11**, 4486-4494 10.1021/acs.jctc.5b00513
184. Lee, J., Cheng, X., Swails, J. M., Yeom, M. S., Eastman, P. K., Lemkul, J. A. *et al.* (2016) CHARMM-GUI Input Generator for NAMD, GROMACS, AMBER, OpenMM, and CHARMM/OpenMM Simulations Using the CHARMM36 Additive Force Field *J Chem Theory Comput* **12**, 405-413 10.1021/acs.jctc.5b00935
185. Hsu, P. C., Bruininks, B. M. H., Jefferies, D., Cesar Telles de Souza, P., Lee, J., Patel, D. S. *et al.* (2017) CHARMM-GUI Martini Maker for modeling and simulation of complex bacterial membranes with lipopolysaccharides *J Comput Chem* **38**, 2354-2363 10.1002/jcc.24895
186. Lee, J., Patel, D. S., Stahle, J., Park, S. J., Kern, N. R., Kim, S. *et al.* (2019) CHARMM-GUI Membrane Builder for Complex Biological Membrane Simulations with Glycolipids and Lipoglycans *J Chem Theory Comput* **15**, 775-786 10.1021/acs.jctc.8b01066
187. Park, S., Choi, Y. K., Kim, S., Lee, J., and Im, W. (2021) CHARMM-GUI Membrane Builder for Lipid Nanoparticles with Ionizable Cationic Lipids and PEGylated Lipids *J Chem Inf Model* **61**, 5192-5202 10.1021/acs.jcim.1c00770

188. Feng, S., Park, S., Choi, Y. K., and Im, W. (2023) CHARMM-GUI Membrane Builder: Past, Current, and Future Developments and Applications *J Chem Theory Comput* **19**, 2161-2185 10.1021/acs.jctc.2c01246
189. Park, S. J., Kern, N., Brown, T., Lee, J., and Im, W. (2023) CHARMM-GUI PDB Manipulator: Various PDB Structural Modifications for Biomolecular Modeling and Simulation *J Mol Biol* **435**, 167995 10.1016/j.jmb.2023.167995
190. Brown, T. P., Santa, D. E., Berger, B. A., Kong, L., Wittenberg, N. J., and Im, W. (2024) CHARMM GUI Membrane Builder for oxidized phospholipid membrane modeling and simulation *Curr Opin Struct Biol* **86**, 102813 10.1016/j.sbi.2024.102813
191. Gee, S., Glover, K. J., Wittenberg, N. J., and Im, W. (2024) CHARMM-GUI Membrane Builder for Lipid Droplet Modeling and Simulation *Chempluschem* **89**, e202400013 10.1002/cplu.202400013
192. Kong, L., Park, S. J., and Im, W. (2024) CHARMM-GUI PDB Reader and Manipulator: Covalent Ligand Modeling and Simulation *J Mol Biol* **436**, 168554 10.1016/j.jmb.2024.168554
193. Kastrup, J. S., Eriksson, E. S., Dalboge, H., and Flodgaard, H. (1997) X-ray structure of the 154-amino-acid form of recombinant human basic fibroblast growth factor. comparison with the truncated 146-amino-acid form *Acta Crystallogr D Biol Crystallogr* **53**, 160-168 10.1107/S0907444996012711
194. Javanainen, M. (2014) Universal Method for Embedding Proteins into Complex Lipid Bilayers for Molecular Dynamics Simulations *J Chem Theory Comput* **10**, 2577-2582 10.1021/ct500046e
195. Michelucci, U. (2022) An Introduction to Autoencoders
196. Buchoux, S. (2017) FATSLiM: a fast and robust software to analyze MD simulations of membranes *Bioinformatics* **33**, 133-134 10.1093/bioinformatics/btw563
197. Michaud-Agrawal, N., Denning, E. J., Woolf, T. B., and Beckstein, O. (2011) MDAnalysis: a toolkit for the analysis of molecular dynamics simulations *J Comput Chem* **32**, 2319-2327 10.1002/jcc.21787
198. Sorre, B., Callan-Jones, A., Manneville, J. B., Nassoy, P., Joanny, J. F., Prost, J. *et al.* (2009) Curvature-driven lipid sorting needs proximity to a demixing point and is aided by proteins *Proc Natl Acad Sci U S A* **106**, 5622-5626 10.1073/pnas.0811243106
199. Mandal, K. (2020) Review of PIP2 in Cellular Signaling, Functions and Diseases *Int J Mol Sci* **21**, 10.3390/ijms21218342
200. Hink, M. A., Griep, R. A., Borst, J. W., van Hoek, A., Eppink, M. H., Schots, A. *et al.* (2000) Structural dynamics of green fluorescent protein alone and fused with a single chain Fv protein *J Biol Chem* **275**, 17556-17560 10.1074/jbc.M001348200
201. Borges-Araujo, L., and Fernandes, F. (2020) Structure and Lateral Organization of Phosphatidylinositol 4,5-bisphosphate *Molecules* **25**, 10.3390/molecules25173885
202. De Craene, J. O., Bertazzi, D. L., Bar, S., and Friant, S. (2017) Phosphoinositides, Major Actors in Membrane Trafficking and Lipid Signaling Pathways *Int J Mol Sci* **18**, 10.3390/ijms18030634
203. Marcus, A. J., Ullman, H. L., and Safier, L. B. (1969) Lipid composition of subcellular particles of human blood platelets *J Lipid Res* **10**, 108-114
204. Vamparys, L., Gautier, R., Vanni, S., Bennett, W. F., Tieleman, D. P., Antonny, B. *et al.* (2013) Conical lipids in flat bilayers induce packing defects similar to that induced by positive curvature *Biophys J* **104**, 585-593 10.1016/j.bpj.2012.11.3836

205. de Kruijff, B. (1987) Polymorphic regulation of membrane lipid composition *Nature* **329**, 587-588 10.1038/329587a0
206. Gilmore, R., Walter, P., and Blobel, G. (1982) Protein Translocation across the Endoplasmic-Reticulum .2. Isolation and Characterization of the Signal Recognition Particle Receptor *Journal of Cell Biology* **95**, 470-477 DOI 10.1083/jcb.95.2.470
207. Steringer, J. P., Muller, H. M., and Nickel, W. (2015) Unconventional secretion of fibroblast growth factor 2--a novel type of protein translocation across membranes? *J Mol Biol* **427**, 1202-1210 10.1016/j.jmb.2014.07.012
208. Wegehingel, S., Zehe, C., and Nickel, W. (2008) Rerouting of fibroblast growth factor 2 to the classical secretory pathway results in post-translational modifications that block binding to heparan sulfate proteoglycans *FEBS Lett* **582**, 2387-2392 10.1016/j.febslet.2008.05.042
209. Hirschberg, K., Miller, C. M., Ellenberg, J., Presley, J. F., Siggia, E. D., Phair, R. D. *et al.* (1998) Kinetic analysis of secretory protein traffic and characterization of golgi to plasma membrane transport intermediates in living cells *J Cell Biol* **143**, 1485-1503 10.1083/jcb.143.6.1485
210. Belghit, H., Spivak, M., Dauchez, M., Baaden, M., and Jonquet-Prevoteau, J. (2024) From complex data to clear insights: visualizing molecular dynamics trajectories *Front Bioinform* **4**, 1356659 10.3389/fbinf.2024.1356659
211. Kühlbrandt, W. (2014) The Resolution Revolution *Science* **343**, 1443-1444 10.1126/science.1251652
212. Jumper, J., Evans, R., Pritzel, A., Green, T., Figurnov, M., Ronneberger, O. *et al.* (2021) Highly accurate protein structure prediction with AlphaFold *Nature* **596**, 583-589 10.1038/s41586-021-03819-2
213. Abramson, J., Adler, J., Dunger, J., Evans, R., Green, T., Pritzel, A. *et al.* (2024) Accurate structure prediction of biomolecular interactions with AlphaFold 3 *Nature* **630**, 493-500 10.1038/s41586-024-07487-w
214. Varadi, M., Bertoni, D., Magana, P., Paramval, U., Pidruchna, I., Radhakrishnan, M. *et al.* (2024) AlphaFold Protein Structure Database in 2024: providing structure coverage for over 214 million protein sequences *Nucleic Acids Res* **52**, D368-D375 10.1093/nar/gkad1011
215. Martinez-Seara, H., Rog, T., Pasenkiewicz-Gierula, M., Vattulainen, I., Karttunen, M., and Reigada, R. (2008) Interplay of unsaturated phospholipids and cholesterol in membranes: effect of the double-bond position *Biophys J* **95**, 3295-3305 10.1529/biophysj.108.138123
216. Alessandri, R., Souza, P. C. T., Thallmair, S., Melo, M. N., de Vries, A. H., and Marrink, S. J. (2019) Pitfalls of the Martini Model *J Chem Theory Comput* **15**, 5448-5460 10.1021/acs.jctc.9b00473
217. Danielsson, A., Samsonov, S. A., Liwo, A., and Sieradzan, A. K. (2023) Extension of the SUGRES-1P Coarse-Grained Model of Polysaccharides to Heparin *J Chem Theory Comput* **19**, 6023-6036 10.1021/acs.jctc.3c00511
218. Fadda, E., and Woods, R. J. (2010) Molecular simulations of carbohydrates and protein-carbohydrate interactions: motivation, issues and prospects *Drug Discov Today* **15**, 596-609 10.1016/j.drudis.2010.06.001
219. Gupta, K., Donlan, J. A. C., Hopper, J. T. S., Uzdavinys, P., Landreh, M., Struwe, W. B. *et al.* (2017) The role of interfacial lipids in stabilizing membrane protein oligomers *Nature* **541**, 421-+ 10.1038/nature20820

220. Tarek, M. (2005) Membrane electroporation: a molecular dynamics simulation *Biophys J* **88**, 4045-4053 10.1529/biophysj.104.050617
221. Cunill-Semanat, E., and Salgado, J. (2019) Spontaneous and Stress-Induced Pore Formation in Membranes: Theory, Experiments and Simulations *J Membr Biol* **252**, 241-260 10.1007/s00232-019-00083-4
222. Neumann, E., Schaefer-Ridder, M., Wang, Y., and Hofschneider, P. H. (1982) Gene transfer into mouse lyoma cells by electroporation in high electric fields *EMBO J* **1**, 841-845 10.1002/j.1460-2075.1982.tb01257.x
223. Akimov, S. A., Volynsky, P. E., Galimzyanov, T. R., Kuzmin, P. I., Pavlov, K. V., and Batishchev, O. V. (2017) Pore formation in lipid membrane I: Continuous reversible trajectory from intact bilayer through hydrophobic defect to transversal pore *Sci Rep* **7**, 12152 10.1038/s41598-017-12127-7
224. Golani, G., and Schwarz, U. S. (2023) High curvature promotes fusion of lipid membranes: Predictions from continuum elastic theory *Biophys J* **122**, 1868-1882 10.1016/j.bpj.2023.04.018

# 7 Appendix

Exemplary gallery of starting points and observed structures for 30 simulations of 2 FGF2 monomers and 2 C95-bridged FGF2 dimers. Starting orientation of proteins was created randomly. In none of the simulations ring-like interactions between proteins was observed. Many interactions were not stable over time. A z-shaped assembly of the dimers and monomers was the only assembly stable for a longer time involving all proteins (**FigureS 1C**). However, I cannot assure that the simulation already reached full equilibrium. As experimental data suggested, FGF2-GFP assemblies on supported lipid bilayers showed a ring-like structure (111), I kept on working with the ring-shaped hexameric assembly of 3 dimers.

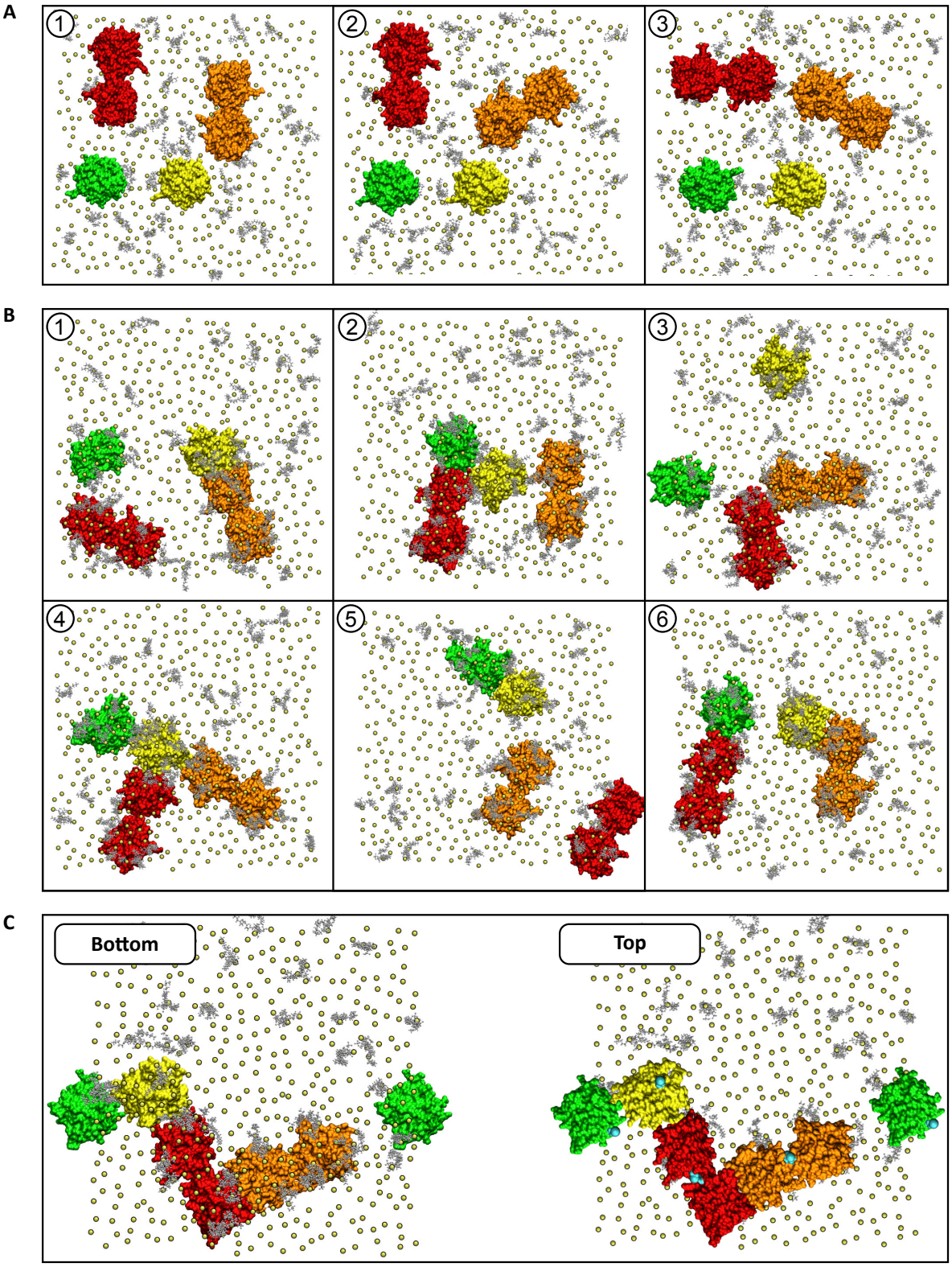


**FigureS 1: Gallery of the self-assembly of 2 FGF2 monomers and 2 C95-linked FGF2 dimers. A** 3 randomly generated starting positions. **B** 6 examples of interactions found in the simulations. **C** Only example of all proteins interacting. The green monomers is displayed twice due to periodic boundary conditions. Red: Dimer 1. Orange: Dimer 2. Yellow: Monomer 1. Green: Monomer 2. Orange beads: P atoms of phospholipids. Grey: 18:0-20:4 PI(4,5)$P_2$. Cyan beads in C: cysteine 95.

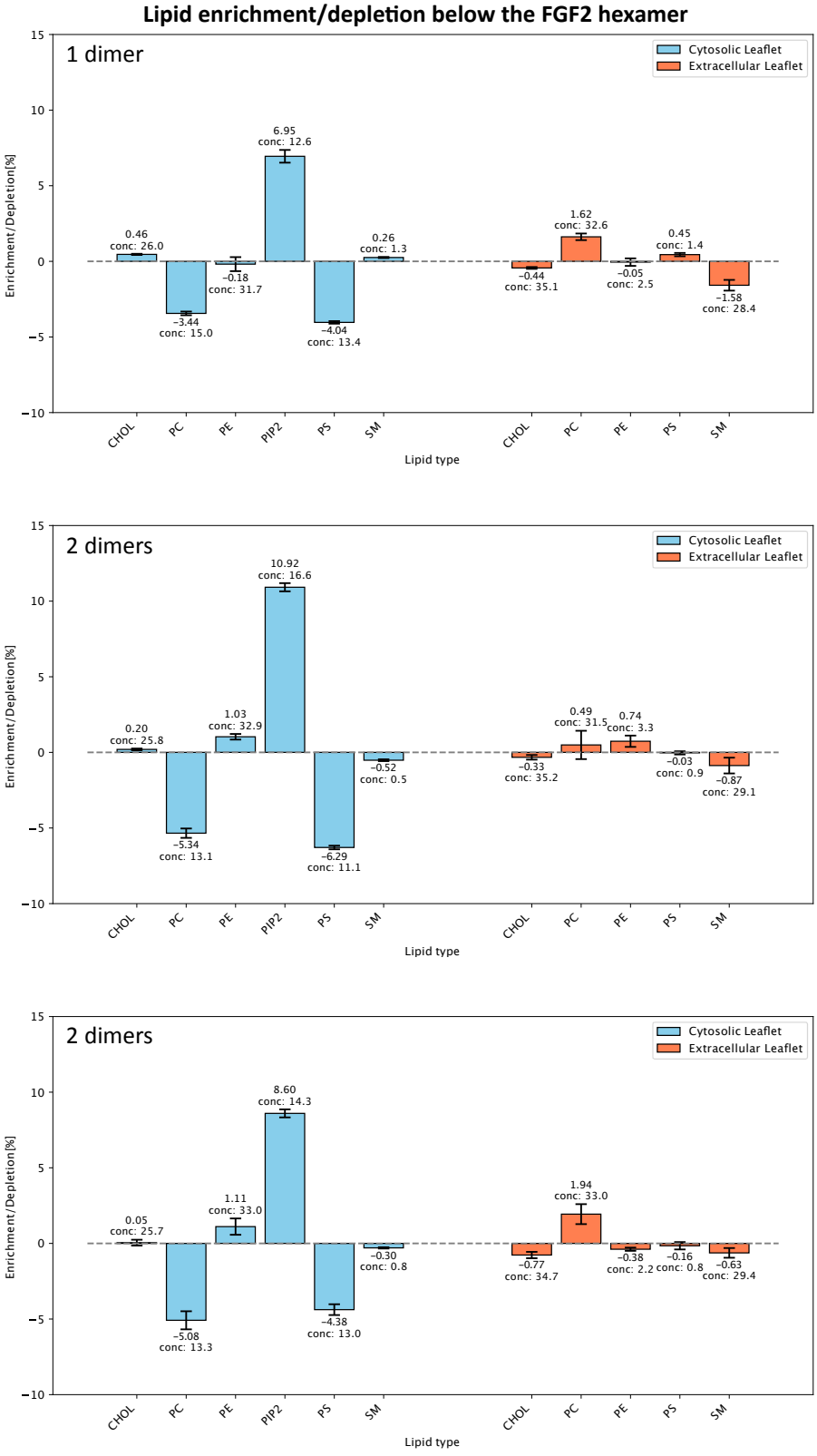


**FigureS 2: Lipid remodeling below 1 or 2 FGF2 dimers. Top**: Lipid enrichment/depletion below 1 FGF2 dimer. **Middle** and **bottom:** Lipid enrichment/depletion below 2 FGF2 dimers.

# 8 Abbreviations

| | |
|---|---|
| % | percent |
| Å | ångstroms |
| ABC | ATP-binding cassette |
| α1 | α1-domain of Na,K-ATPase |
| C77 | cysteine 77 |
| C95 | cysteine 95 |
| $Ca^{2+}$ | divalent calcium ions |
| COPI/II | coat protein complex I/coat protein complex II |
| ER | endoplasmic reticulum |
| ERAD | ER-associated protein degradation |
| ERGIC | ER-Golgi intermediate compartment |
| FGF | fibroblast growth factor |
| FGFR | fibroblast growth factor receptor |
| GFP | green fluorescent protein |
| GPC1 | glypican-1 |
| GPI | glycosylphosphatidylinositol anchor |
| GPU | graphics processing unit |
| GUV | giant unilamellar vesicles |
| HIV | human immunodeficiency virus |
| HMW | high-molecular weight |
| HSPG | heparan sulfate proteoglycans |
| I-BAR | inverse Bin/Amphiphysin/Rvs domain |
| Il-1β | Interleukin-1β |
| kDa | kilo Dalton |
| LMW | low-molecular weight |
| LUV | large unilamellar vesicles |
| MD simulations | Molecular Dynamics simulations |
| NLS | nuclear localization signal |

| | |
|---|---|
| NMR | nuclear magnetic resonance spectroscopy |
| ns | nanoseconds |
| P | All atoms name for the phosphate atom linking glycerol backbone and lipid headgroup |
| PBC | periodic boundary condition |
| PC | phosphatidyl choline |
| PE | phosphatidyl ethanolamine |
| PH domain | pleckstrin homology domain |
| PI(X)Px | phosphatidylinositol phosphate |
| PME | particle mesh ewald method |
| PO4 | Martini2.2 naming for phosphate group linking glycerol backbone and lipid headgroup |
| PS | phosphatidyl serine |
| RF | reaction field method |
| SM | sphingomyelin |
| U2OS | Human bone osteosarcoma epithelial cells |
| VdW | Van-der-Waals interactions |
| wt | wildtype |
| µs | microseconds |

# 9 Acknowledgments

First and foremost, I would like to express my gratitude to Walter Nickel for granting me the opportunity to pursue my PhD thesis in his lab. I am deeply thankful for his support, even during challenging times. Besides the mentoring and professional exchange, I always enjoyed our chats, especially about the doggies.

Then, I want to thank Fabio Lolicato for teaching me all about Molecular Dynamics simulations and being always open for questions and discussions in that time. Your guidance has been invaluable, and I would not be where I am today without your support.

Many thanks also go Thomas Söllner and Petr Chlanda, who always supported me as members of my thesis advisory committee. Their insights and guidance were valuable to me for the progress of my project.

A big thank you also goes to every member of the Nickel lab, past and present, whom I had the pleasure of meeting over the years. I truly enjoyed our conversations and exchanges, in the lab or privately. Cheers go out to you, Britta, Manpreet, Ana, Jaime, Ali, Annalena, Carola, Roberto, Julia, Sabine, and Michael. I also had the great pleasure to supervise and work with my two students in our private lab during the COVID times, I learned a lot from you Denise and Sarah.

Another thank you to all of you in the BZH, who I met over the years, or met again after long years. I met some of my best friends here, who became an important part of my life.

Though I was not around often, I enjoyed the Monday trips to Boulderhaus Mannheim with the Schookies. Thank you for inviting me.

I also want to thank Gonen Golani for the great work and insights from a membrane expert, helping me understand the results of my work.

I thank Dirk Flemming and Petr Chlanda for teaching me to work with the large cryo electron microscopes early on in my project.

Zum Schluss möchte ich noch meinen Eltern danken, die mich auf dem Weg hier her immer begleitet und unterstützt haben.